Title
Surface and Solution Mediated Studies of Small Molecule Enediyne Reactivity

Author
Gorman, Patrick

Publication Date
2016

Peer reviewed|Thesis/dissertation

Surface and Solution Mediated Studies of Small Molecule Enediyne Reactivity

By

Patrick Gorman

A dissertation submitted in partial satisfaction of the

requirements for the degree of

Doctor of Philosophy

in

Chemistry

in the

Graduate Division

of the

University of California, Berkeley

Committee in charge:

Professor Felix R. Fischer, Chair
Professor Omar M. Yaghi
Professor Tanja Cuk
Professor Michael F. Crommie

Fall 2016

Abstract

Surface and Solution Mediated Studies of Small Molecule Enediyne Reactivity

by

Patrick Gorman

Doctor of Philosophy in Chemistry

University of California, Berkeley

Professor Felix R. Fischer, Chair

Enediyne chemistry is a field with growing potential especially in the industries of material synthesis, catalysis, and therapeutic drug design. Enediynes offer a flexible synthetic handle with which to design these materials. However reactivity of enediynes is complex and in need of extensive and unambiguous characterization (Chapter 1). Imaging techniques like non-contact atomic force microscopy (nc-AFM) and scanning tunneling microscopy (STM) can be utilized for unambiguous determination of reaction products. Using, nc-AFM and STM, supported with *ab initio* density functional theory (DFT), we provide a glimpse into the reactive capabilities of enediynes and precisely characterize the complex product mixture from a reaction of 1,2-bis((2-ethynylphenyl)ethynyl)benzene (Chapter 2). Tailoring reaction conditions, including enediyne structure, can also result in tailoring the product of enediyne cyclization reactions. We characterize the chemical and electronic structure of individual chains of oligo-(E)-1,1'-bi(indenylidene), a poly-acetylene derivative that we have obtained through cooperative C^1–C^5 thermal enediyne cyclizations on Au(111) surfaces followed by a step-growth polymerization of the (E)-1,1'-bi(indenylidene) diradical intermediates (Chapter 3). These chemical transformations offer contrast to those from our initial investigation prompting a comprehensive study of the molecular energetics and conformational dynamics underlying these transformations. We report the detailed investigation of a surface-catalyzed cross-coupling and sequential cyclization cascade of 1,2-bis(2-ethynyl phenyl)ethyne on Ag(100) supported by theoretical simulations. These simulations indicate that the kinetic stabilization of experimentally observable intermediates is observably influenced by selective energy dissipation to the substrate and entropic changes associated with key transformations along the reaction pathway (Chapter 4). Finally, we begin to build on a motif by which to synthesize one-dimensional materials using the reactivity lessons learned from surface studies of enediynes. Synthesis of new small molecule enediynes is discussed, the thermodynamics of Bergman cyclization is considered and evaluated, and polymers are synthesized using Bergman Cyclization Polymerization (BCP) (Chapter 5).

To My Teachers

You Instilled In Me a Passion

For Knowledge and the Pursuit of Truth

You Taught Me the Importance

Never to Compromise My Values

You Stressed Attention to Detail

And

You Inspired Me

Never to Settle for Anything Less Than

Perfection

Table of contents

Acknowledgments

First and foremost I have to acknowledge the man who believed in me and enabled my completion of this work. Thank you Felix for taking me into your lab and giving me a shot.

As this work was highly collaborative, I have to give a great deal of thanks to Prof. Michael Crommie and his lab, especially Dr. Yen-Cia Chen, Dr. Dimas de Oteyza, Dr. Sebastian Wickenberg, and Dr. Alexander Riss. Without all the dedicated time and effort they provided, this work would not exist.

I want to thank the rest of my dissertation committee, Prof. Tanja Cuk and Prof. Omar Yaghi. Thank you for your support and input over the years.

Most importantly without the support of my friends and family, I would be nowhere and this degree and work would mean nothing. The people in my life bring meaning and value to all I do.

To mom, dad, and Kathryn, thank you for everything. You've always been by me from the start. To say that I earned this degree only over the span of the last five years would do no justice to the twenty-three years prior. This degree is the sum of all the love you've ever given me.

To Aunt Sheila, you're always there for me and you give without question. I couldn't ask for a better Godmother.

You don't get to choose your coworkers and labmates, but I would never trade the ones I ended up with for anyone else. Thanks Dona and Justin for always being the friends that I looked forward to seeing each day in lab – even on the tough days. It'll feel weird without your desks next to mine.

Lastly, I want to thank all of my Berkeley friends, especially all of the housemates with whom I've lived over the last five years. Not everyone is able to call the people with whom they live their friends, and I have been exceptionally fortunate to call all nineteen people with whom I've shared my home my great friends. You will all forever share a place in my heart.

And to the crew that started it all; the people I met serendipitously online that became my closest friends in person: To Brad, Tina, and Becca, I don't know where I'd be without your friendship throughout these last five years. I can only hope you understand the enormity of your influence on my life and on the completion of my degree. I consider you a special part of my family and I wish you all the best in the world.

Cheers!

Chapter 1
Introduction

A motivation for studying enediyne reactivity is presented. We will discuss first historical relevance of enediyne reactivity and its origins in synthetic chemistry. We will discuss how enediynes and their close relationship with metal centers can alter their reactivity as a basis for our understanding of how metal surfaces may influence enediyne reactivity. The importance of enediynes in material synthesis will be presented, as will the challenges associated with characterization of these materials. We will therefore discuss the importance of studying enediyne reactivity on surfaces, and the importance of using advanced microscopy, like non-contact atomic force microscopy and scanning tunneling microscopy, to characterize products of enediyne reactions.

1.1 Introduction

Enediynes are a special class of molecule characterized by an alternating set of two triple bonds on either side of a double bond. Owing to their unique structure, they have a variety of chemically relevant reaction mechanisms available to them. Evidence of their ability to perform thermal rearrangement was first noted in 1971 by Masamune *et al*.[1] Upon reaction of a butyne tethered

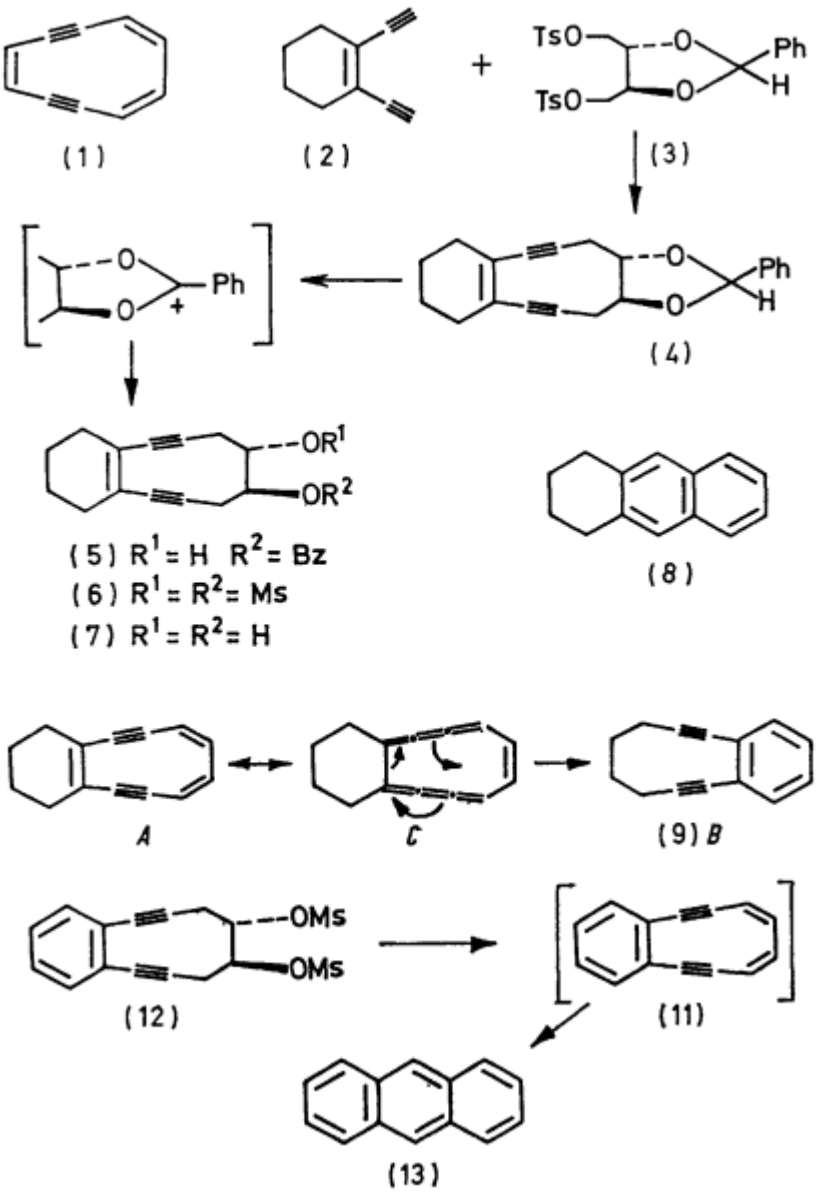

Figure 1.1 Evidence of enediyne cyclization observed by Masamune.[1] Upon reaction of the compounds "(5)-(7)" with sodium methoxide, "(8)" was formed. [Reproduced from ref. 1].

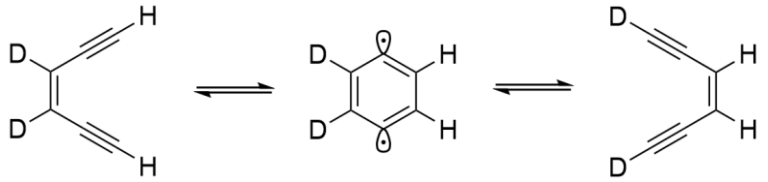

Scheme 1.1 Deuterium scrambling experiment performed by Bergman and Jones.[2]

enediyne (Figure 1.1, (5)-(7)) with sodium methoxide, it was noted that tetrahydroanthracene was recovered. Bergman and Jones investigated the nature of this reaction in 1972.[2] By performing simple deuterium scrambling experiments (Scheme 1.1), they were able to determine that enediynes are capable of undergoing thermal pericyclic rearrangements, passing from one enediyne to another through a reactive dehydrobenzene intermediate. The reaction fittingly became known as Bergman cyclization.

While discovery and investigation of this particular mechanism began in the '70s, it wasn't until discovery of natural enediynes that research on enediynes began to flourish.[3–6] The natural enediynes calicheamicin (1987),[4] esparamicin (1987),[5] and dynemicin (1990)[7] were soon after

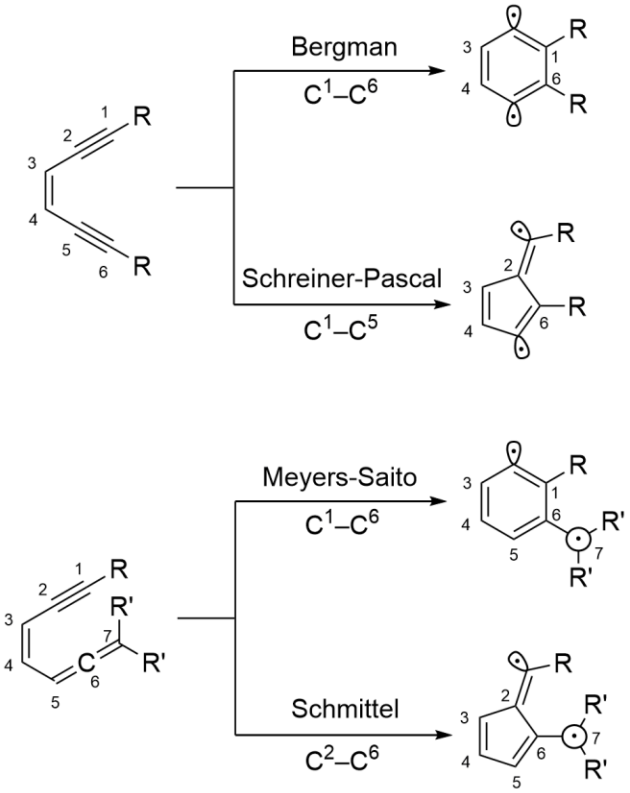

Scheme 1.2 Thermal rearrangements of enediyne (top) and enyne-allene (bottom) compounds. Bergman cyclization, a C^1–C^6 cyclization results in the generation of a 1,4-dehydrobenzene diradical species. Schreiner-Pascal cyclization, on the other hand, begins with the same enediyne compound yet undergoes C^1–C^5 cyclization resulting in a fulvene.

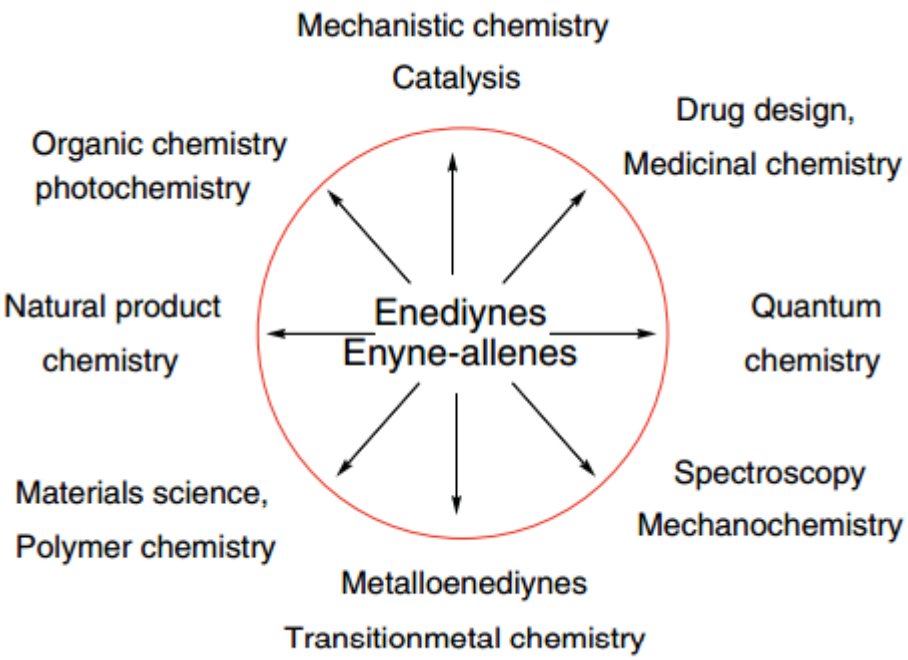

Figure 1.2 Enediynes are widely applicable in modern chemistry, ranging from drug design to polymer chemistry and even to catalysis. [Reproduced from ref. 6]

their discovery considered as possible leads for antitumor antibiotics. The ability for tumor suppression led to more reactive mechanisms of enediynes and enyne-allenes, a similar class of compounds, to be further explored. These mechanisms included Meyers-Saito[8–12] and Schmittel[13–16] cyclizations (Fig. 1.2). It wasn't until 2001 that another chemically relevant enediyne cyclization was proposed by Schreiner.[17] Drawing from analogous experiments which indicated that although the Meyers-Saito cyclization is energetically favored for enyne-allenes due to a gain of aromaticity in the product, it was possible to force Schmittel cyclization by increasing the steric bulk of the terminal substituents, Schreiner proposed a C^1–C^5 cyclization of enediynes which was later, in 2008, experimentally confirmed by Pascal.[18] If we can continue to study and learn about the intricate and delicate mechanisms involved in enediyne reactivity, there are many potential applications for their use.

1.2 Motivation

Enediyne research has found a niche in a multitude of scientific fields, most notably the biochemical field for its anti-cancer applications. However, if we look into the literature we will find a host of other important opportunities for enediyne reactivity (Fig. 1.2).

1.2.1 Enediynes and Metals

The use of metals for a modulation of the Bergman cyclization has become an emerging research field.[6,19–21] Understanding how metals may influence the reactivity of enediynes is important for

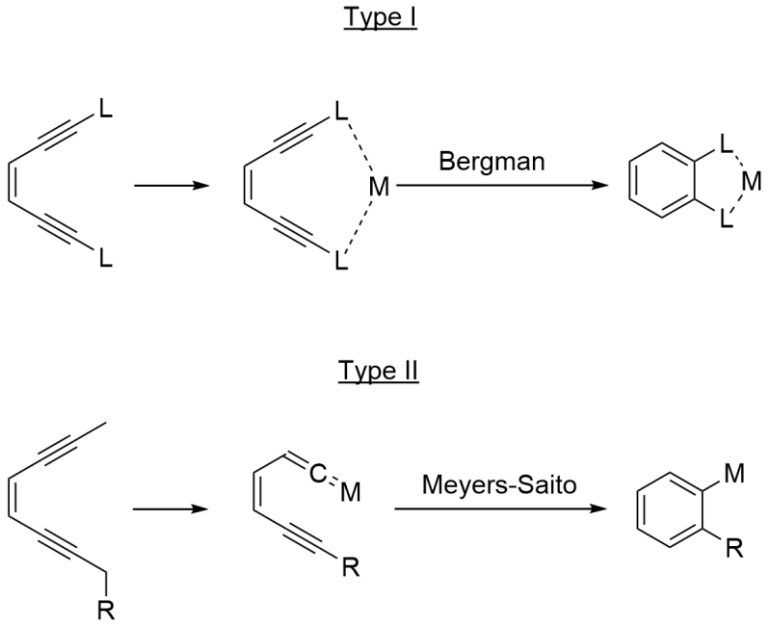

Scheme 1.3 Two mechanisms of Bergman cyclization mediated by metal atoms. In the first instance (Type I) a metal cation binds to terminal ligands on the enediyne facilitating cyclization. In the second example (Type II) an organometallic reagent promotes isomerization of the enediyne to form an enyne-allene, which formally undergoes Meyers-Saito cyclization to form the analogous product.[6]

applications in synthesis and may have potential for applications in surface chemistry. In general, metal sites offer additional structural flexibilities, which contributes to their intriguing Bergman cyclization reactivity. In fact, Buchwald[22] and König[23] were able to support that enediyne cyclization temperatures were modifiable depending on the choice of metal used to chelate the alkyne substituents (Scheme 1.3, top). Based on their finding, it appears that there are two basic modes of action. Type I: Enediynes bind via their ligands L to a metal ion M thus forming a metal-chelated ring, which undergoes the Bergman cyclization (Scheme 1.3, top). Type II: Organometallic reagents promote the isomerization of enediynes to enyne-allenes, followed by a Myers–Saito cyclization (Scheme 1.3, bottom). Some representative examples will be discussed in the following. 1,2-Bis(diphenyl-phosphino)ethynyl) undergoes the Bergman cyclization at 243 °C, as measured by differential scanning calorimetry.[22] Complexation with Pd(II) or Pt(II) lowers the barrier considerably so that cyclization takes place at 61 °C and 81 °C, respectively. Based on these findings, Zaleski and co-workers[21] designed redox-activated metalloenediyne prodrugs leading to a new strategy for potential dual-thread metalloenediyne therapeutics. A promising application of metallo-enediynes also exists in the field of photodynamic therapy. Zaleski and co-workers[24] also synthesized a vanadium (V) complex with strong ligand-metal charge transfer transitions in the near infrared region caused by the low redox potentials of the highly valent vanadium center and easily oxidizable metal bonds. The Bergman cyclization is

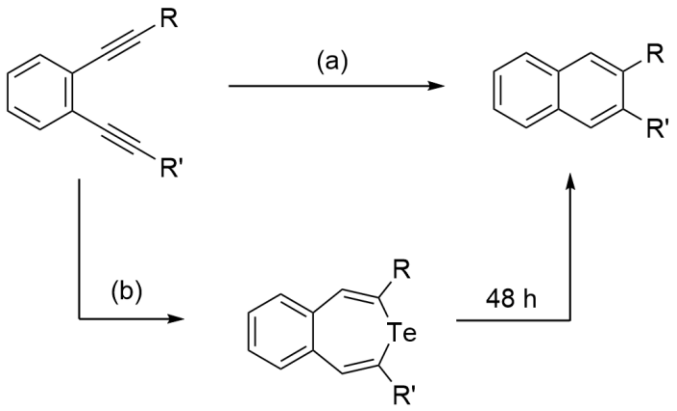

Scheme 1.4 Reaction conditions: (a) 180 °C benzene, 1,4-cyclohexadiene, sealed vessel. (b) Na_2 Te, hydrazine, benzene/water. [Reproduced from ref 25]

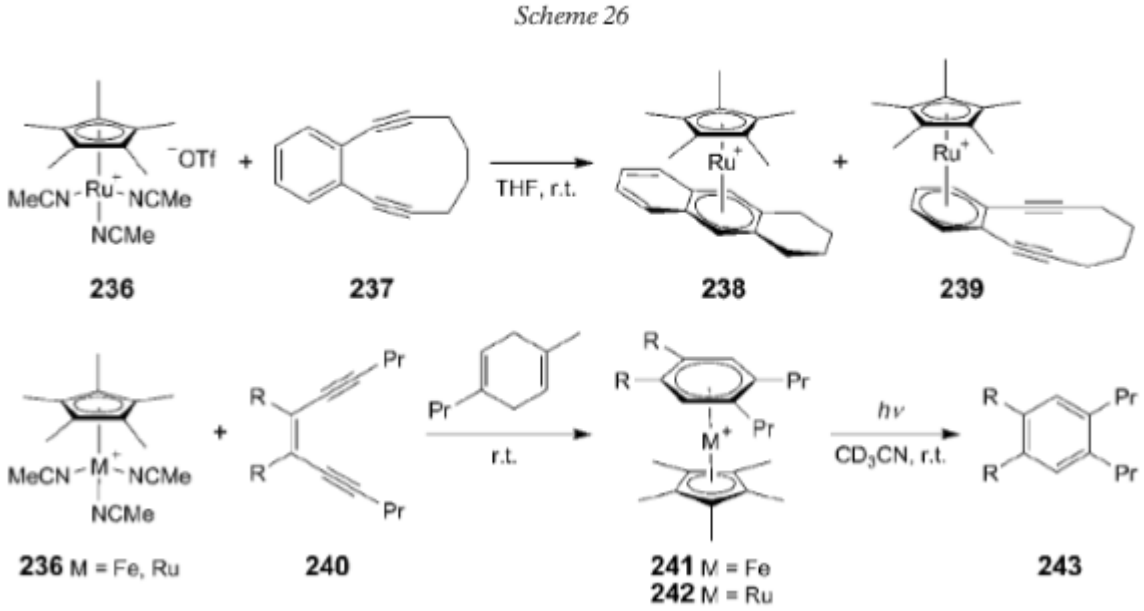

Scheme 1.5 Use of Ru-arene and Fe-arene complexes for room temperature cyclization of enediynes. [Reproduced from ref. 19]

activated photochemically using laser light of the wavelength 785 and 1064 nm, respectively, which correspond to wavelengths that ensure enhanced tissue penetration.[6]

Other enediyne cyclizations facilitated by metals have also been attempted.[19] For example, Anthony[25] and Tsuchiya[26] reported the use of tellurides to facilitate Bergman cyclization without modification of the alkyne termini. They even reported the ability to isolate the benzotellurepines in order to demonstrate that the reactive intermediate evolved by hydrotelluration (Scheme 1.4).

Additionally, O'Connor[27–29] reported the use other metal-arenes for room temperature Bergman cyclization (Scheme 1.5).

As we can see, metals can play an important part in enediyne reactivity, and it may be possible to intricately control the kinetics of enediyne cyclization. It appears as though there is much unlocked potential concerning our control over enediyne reactivity.

1.2.2 Enediynes for Material Synthesis

Further understanding of enediyne systems may give us intimate control of reactive structure. Given a particular enediyne, it may be possible to conditionally react it to obtain a specific product. As we've seen, given an enediyne, it may, depending on its reaction conditions and structure,

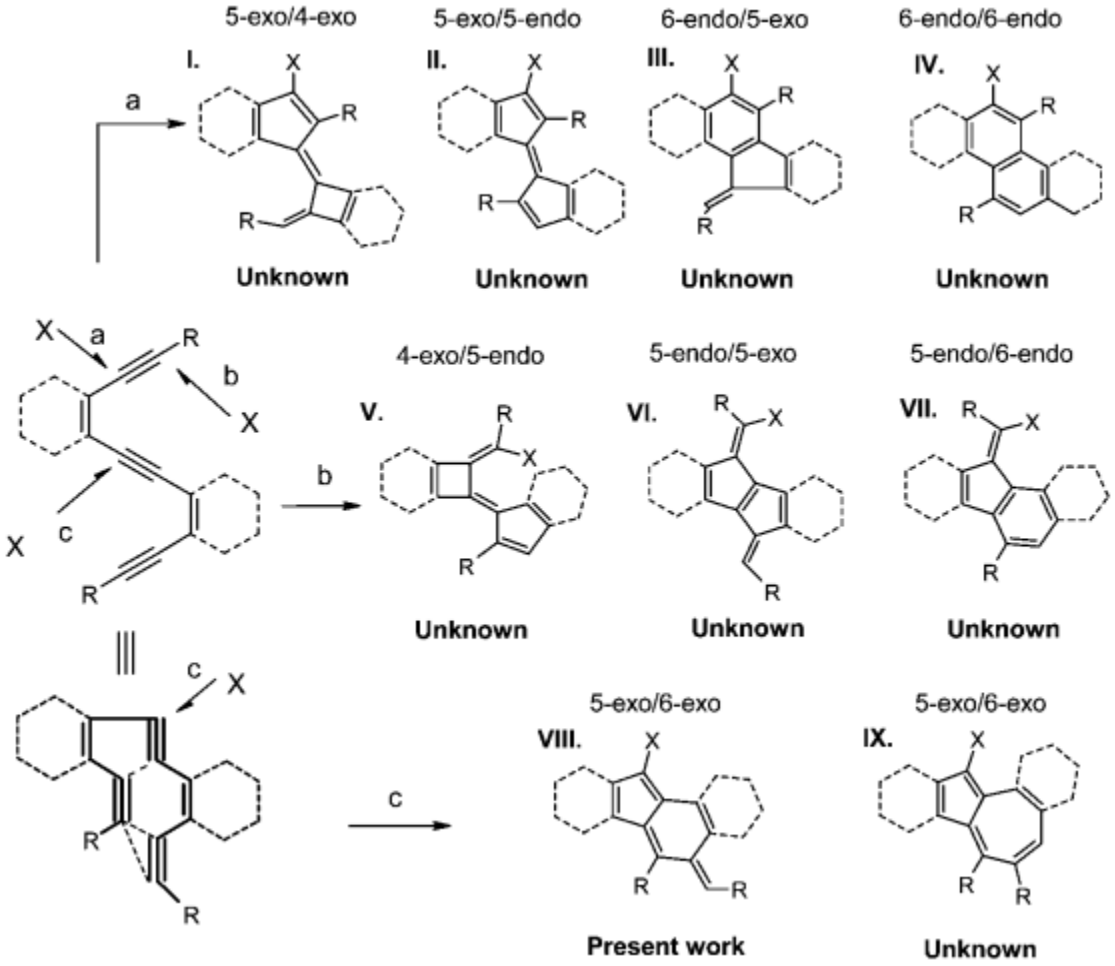

Scheme 1.6 A list of potential reaction for an *oligo*-phenylene ethynylene. Owing to the flexibility of the polymer and each pair of enediynes ability to undergo multiple different cyclization reactions, it is a reaction that generates many different products, many of which have yet to be isolated and characterized. [Reproduced from ref. 30]

undergo various reactive mechanisms including Bergman cyclization and Schreiner-Pascal cyclization. Control over reactivity and structure may give us a functional handle on precise material fabrication. The rich potential of alkyne functionality is manifested particularly well in cascade cyclizations.[30] Such transformations allow for the efficient and atom-economical preparation of polycyclic frameworks [31–38] found in carbon nanostructures, and other useful molecules.[39–44]

It is worth noting, however that despite these potential applications, these small molecule enediynes, and *oligo*-enediynes, have been relatively understudied.[45,46] Although, given chemists' access exclusively to bulk characterization methods, it makes sense that the intractable products formed in these reactions are difficult to characterize. Scheme 1.6 points to the complication of characterizing the reactive products of thermolysis of *oligo*-enediynes. Despite this complication,

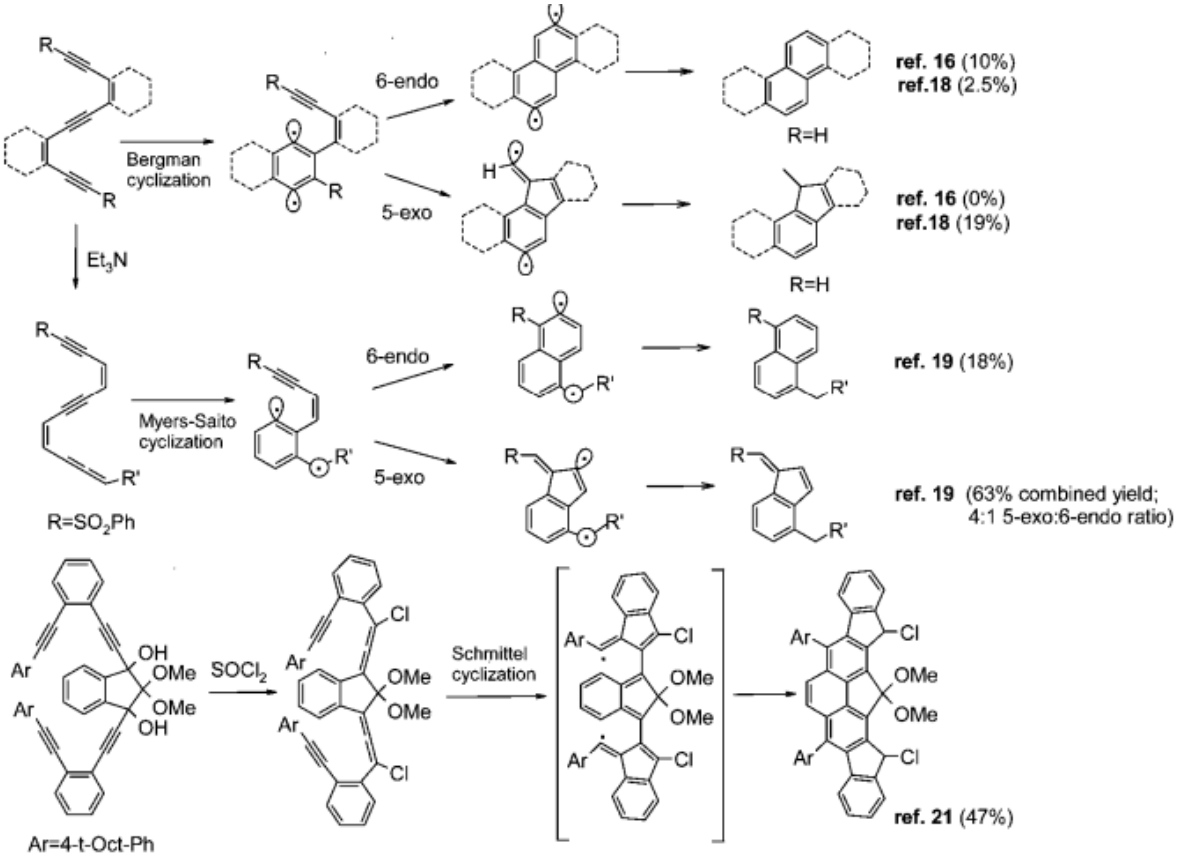

Scheme 1.7 Some examples of isolated cyclization products of enediynes. It is of note that while some products are isolated and characterized, that additional resulting side products remain unaccounted. To fully understand the reaction kinetics of such a complex reaction mechanism, it is important to find a way to solve the issue of "lost products", and to be able to fully characterize the reaction. [Reproduced from ref. 30] Note: The reference numbers provided in the figure do not correspond to the references in this work.

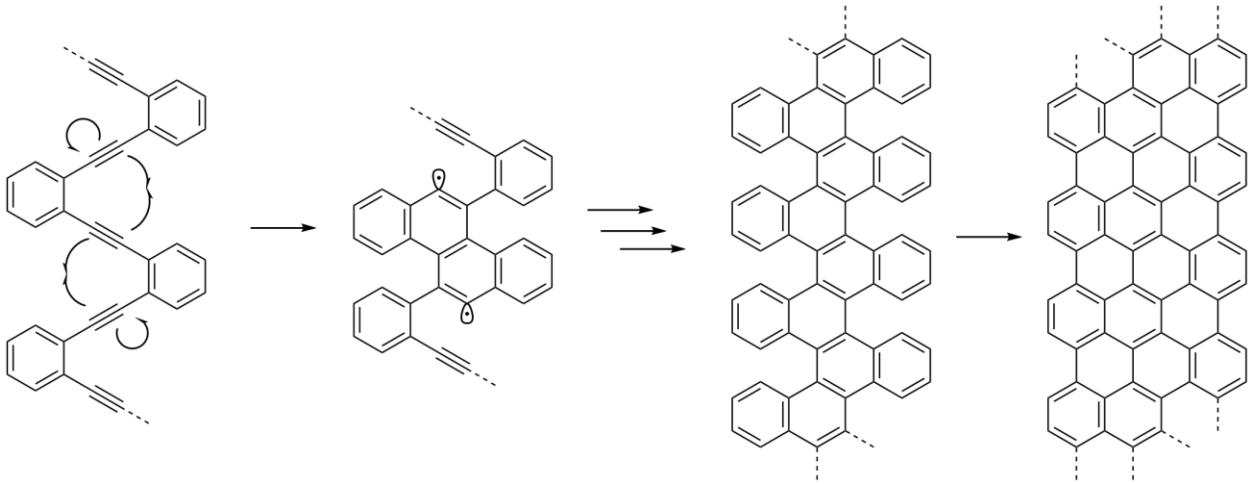

Scheme 1.8 Schematic representation of a series of possible cascade ring closing reactions leading to a GNR. Schematic representation of a 6-endo-dig cyclization cascade followed by dehydrogenation reactions leading to increased width of the GNR. The challenge associated with the conversion of polymer precursors into well-defined GNRs lies in the control of the cyclization cascade. This is a potent example of how enediyne cyclization, if controlled, can lead to a material with interesting electronic properties.

it is important to understand the reactivity of *ortho*-arylene ethynylenes, not only for the development of new polymers incorporating this structural unit, but also for the understanding of structure and properties of conjugated materials prepared through radical polymerization of enediynes.[47–52] However, surprisingly, all such cascades (Scheme 1.6, 1.7) starting with an addition of an external radical to one of the triple bonds are still undocumented.[30]

Being able to control enediyne cyclization may lead to the synthesis of interesting electronic materials and polymers. Conjugated polymers are attractive for their fundamental properties as well as their potential for industrial applications.[53–55] Their tunable electronic structure makes them a useful material for applications in the fields of molecular electronics and photonics.[56–58] Numerous chemical reactions yielding conjugated polymers have been adapted for the synthesis of well-defined molecular wires on surfaces.[59–69] Effective utilization of carbon-based nanostructures resulting from these reactions requires the development of synthetic tools to control the chemical and electronic structure of the polymer products. Of particular importance for advanced electronics applications[70] is the formation of polymeric structures featuring extended π-conjugation during the growth process from small-molecule building blocks. An example of a class of polymeric structures with electronically important properties are graphene nanoribbons (GNRs). GNRs, have been celebrated for their electronic properties boasting ballistic conductivity[71–73] and, due to quantum confinement and edge effects, semiconducting properties.[62,74,75] It has to be mentioned that enediynes have found a special role in materials science and polymer chemistry.[76]

1.3 Enediynes, Surface Chemistry, and Advanced Microscopy

1.3.1 Characterization

The complications of characterization of certain syntheses that arise from imperfect characterization techniques, especially ones that rely on ensemble averaging like nuclear magnetic resonance (NMR), prevent unambiguous structural determination of complicated synthetic mechanisms.[77] Without unambiguous structural information, it will further be impossible to characterize enediyne reactivity. Furthermore, it will be impossible to tailor enediyne cyclization to produce viable molecular materials.

Some of these challenges can be overcome by high-resolution scanning probe techniques which have been used to study chemical transformations at the single-molecule level.[69,78–87] Unambiguous identification of complex organic molecules by scanning tunneling microscopy (STM), however, generally still requires support from theoretical calculations.[79,88–91] Non-contact atomic force microscopy (nc-AFM) measurements with functionalized tips,[92,93] on the other hand, allow direct imaging of chemical structure and covalent bonding within organic molecules[94–96] nc-AFM can be a useful tool for unambiguously determining atomic structure. Then, once structure is assessed, electronic characterization can be achieved as most of these systems are capable of scanning tunneling microscopy (STM).

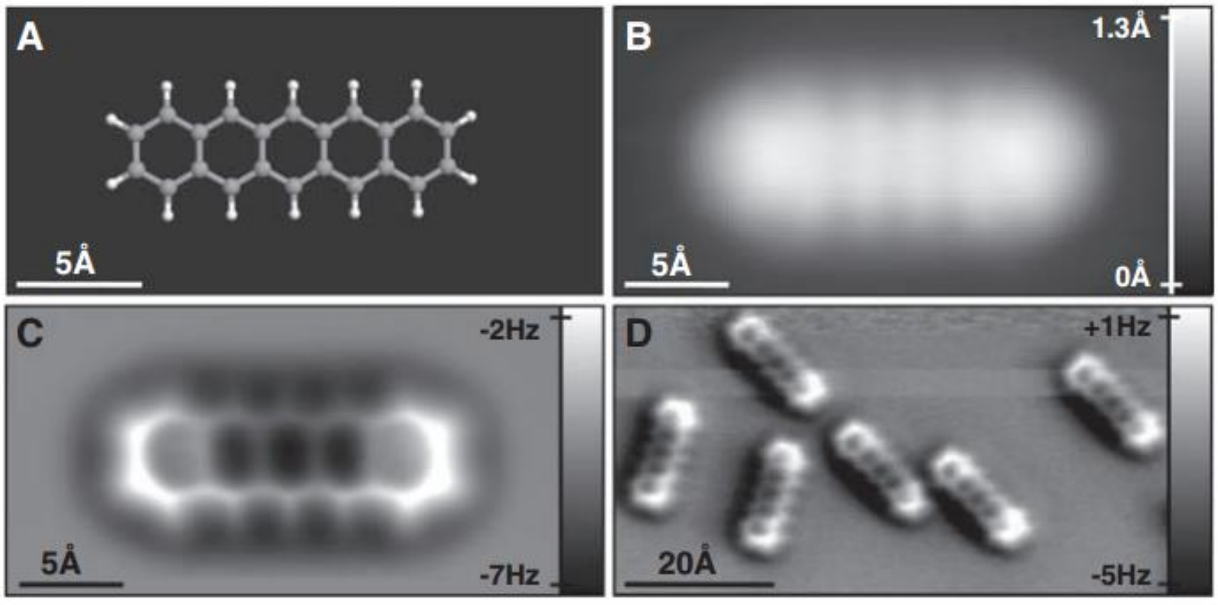

Figure 1.3 The first reported images of an organic molecule with atomic resolution. (A) A "ball-and-stick" model of pentacene. (B) Constant current STM of pentacene. (C) and (D) constant height nc-AFM images of pentacene obtained with a CO-modified tip. C-C bonds can be clearly resolved. C-H bonds can even be resolved. [Reproduced from ref. 94]

The application of nc-AFM to mechanistic problems in chemistry is a research area in its infancy. However, nc-AFM has been used to obtained "images" of single molecules. For example, atomic resolution was achieved on single-walled carbon nanotubes (SWNTs)[97,98] and most notably on pentacene.[99] Figure 1.3 illustrates how nc-AFM, combined with STM, can confirm with atomic precision the chemical structure of a molecule as well as the electronic structure of a molecule. By unambiguously resolving the atomic structure of a material, we will be able to unlock a new characterization technique that can allow organic chemists to resolve complex product mixtures. Single-molecule images obtained with this technique are reminiscent of wire-frame chemical

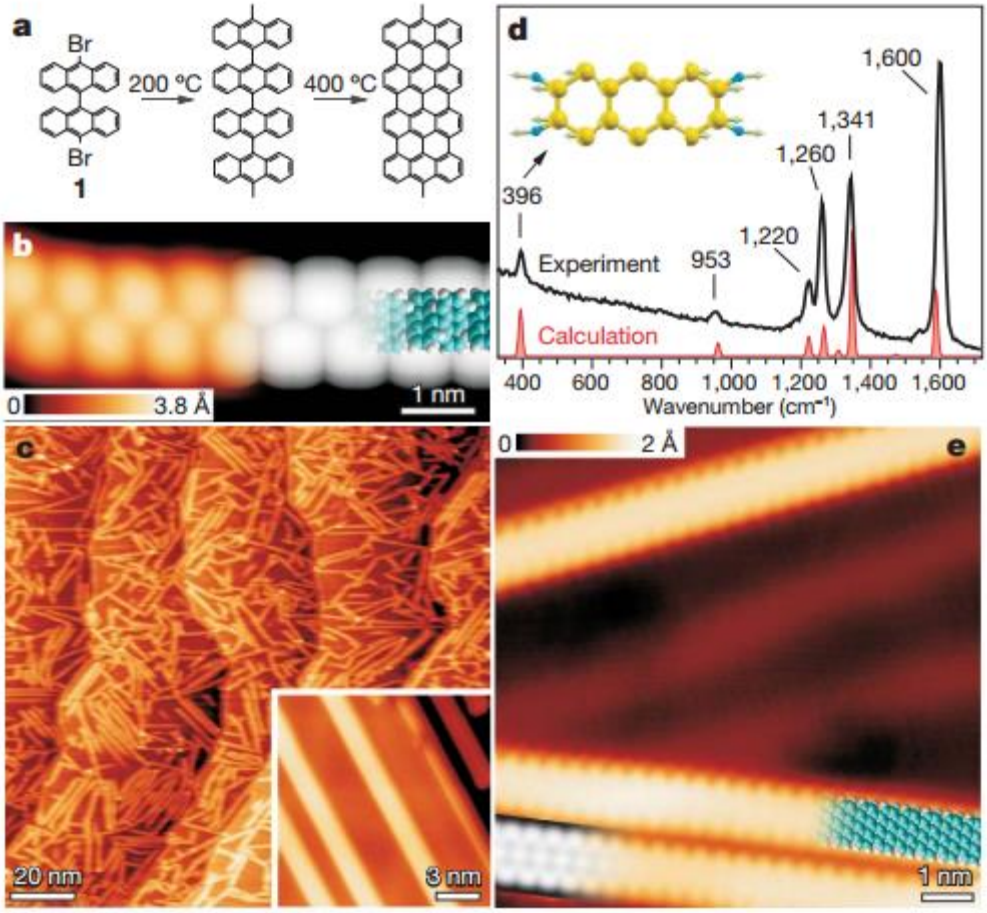

Figure 1.4 Surface assisted synthesis of *poly*-acenes using 10,10′-dibromo-9,9′-bianthryl monomers as precursors on Au(111). (a) Reaction scheme of dibromo precursor polymerizaing to form a *poly*-anthracene, and subsequently oxidizing to form a GNR. (b) STM image taken after polymerization at 200 °C. (c) Large-scale overview of ribbons after post-polymerization modification at 400 °C. (d) Raman spectrum of *n*=7 GNRs compared to theory. (e) High-resolution STM of final GNR with overlaid molecular model in blue. A DFT-based STM simulation of *n*=7 GNRs is overlaid in greyscale. [Reproduced from ref. 63]

structures and even allow differences in chemical bond order to be identified.[95] We believe it is possible to resolve with nc-AFM the intramolecular structural changes and bond rearrangements

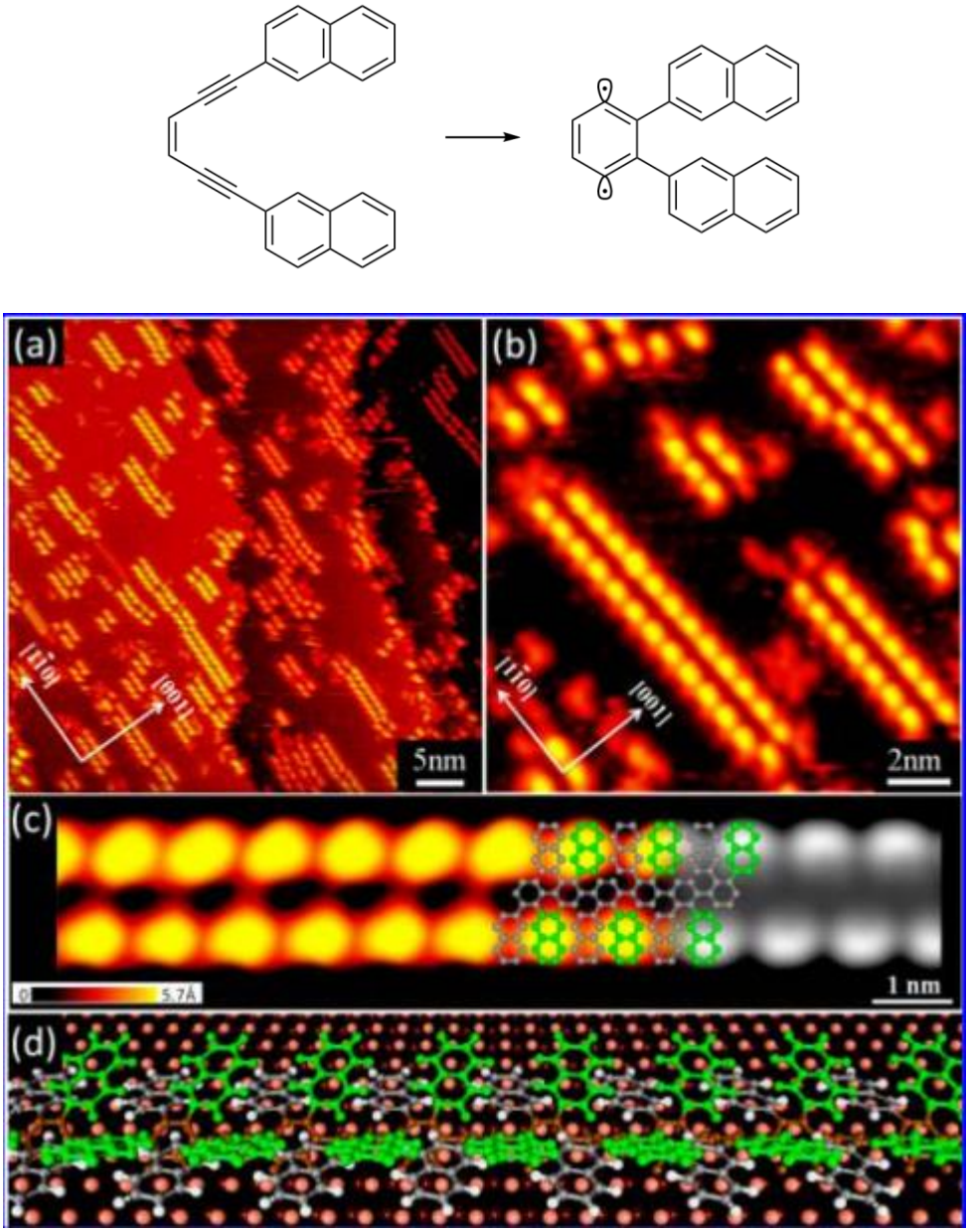

Figure 1.5 Surface templated cyclization of an enediyne (top). (a) Large-scale and (b) close-up STM images of post-Bergman-cyclized products on Cu(110). (c) After cyclization, they arrange into a one-dimensional secondary structure. However, covalent bonding between monomer segments is not unambiguously determined. (d) Structural model illustrating that the naphthyl segments are alternatingly tilted out of plane with the surface. [Reproduced from ref. 88]

associated with complex surface-supported cyclization cascades, thereby revealing the microscopic processes involved in chemical reaction pathways.

1.3.2 Surface Chemistry and Templating

Fabrication of on-surface molecular electronic devices remains one of the most fascinating goals within nanotechnology. Key challenges lie in controllable construction of nanostructures with molecular precision. Recently, the synthesis of covalently interlinked nanostructures from individual molecular building blocks through various kinds of well-known chemical reactions on single-crystal metal surfaces under ultrahigh vacuum (UHV) conditions has been achieved.[62,63,68,69,100–104] This strategy has stimulated intense attention in surface chemistry since it allows the formation of nanostructures with high thermal and chemical stability in comparison with non-covalent self-assembled nanostructures, prohibits the risk of solvents and other contaminants, and facilitates *in situ* characterization by STM.

Figure 1.4 illustrates one specific use of surfaces for material synthesis. In this example, a dibromobisanthracene precursor is deposited on an atomically clean Au(111) surface. Upon annealing, the precursor undergoes homolytic cleavage of the aryl-halide bonds and polymerizes. It is worth noting that while this process is apparently catalyzed by the surface, as the surface aids in the aryl-halide bond cleavage, the most important aspect is that the surface provides a template upon which the reaction, as well as structural and electronic characterization, may occur.[62]

Surfaces may also template the Bergman cyclization. If possible, The Bergman reaction should be especially interesting for on-surface fabrication of molecular nanostructures because it is a byproduct-free synthetic route involving one component with no strict requirement of a catalyst. Figure 1.5 illustrates the potential use of surfaces in templating Bergman cyclization reactions.[90] It was seen that Cu(110) was capable of templating Bergman cyclization on surfaces. In addition, after the initial annealing, the monomers arranged into a secondary structure which could possibly imply that ribbon formation from enediyne precursors is in fact possible.

Surface chemistry may allow for the perfect environment within which to study enediyne reactivity.

1.4 This Work

This work will focus lessons learned from enediyne reactivity. The goal of this work is to learn from surface studies to help inform solution studies. Chapter 2 will outline unambiguous product determination from a complex reaction of an *oligo*-enediyne, thus solving our issue of "imperfect" characterization. Chapter 3 will build on Chapter 2 illustrating the manipulation of a different *oligo*-enediyne for conjugated polymer synthesis. Chapter 4 will delve into the thermodynamics of individual reaction dynamics of the *oligo*-enediyne presented in Chapter 3. Finally Chapter 5 will outline attempts at synthesis and characterization of materials generated from enediyne cyclizations of small molecule enediynes.

Introduction

Chapter 2

Direct Imaging of Covalent Bond Structure in Single Molecule Chemical Reactions

Observing the intricate chemical transformation of an individual molecule as it undergoes a complex reaction is a long-standing challenge in molecular imaging. Advances in scanning probe microscopy now provide the tools to visualize not only the frontier orbitals of chemical reaction partners and products, but their internal covalent bond configurations as well. We used noncontact atomic force microscopy to investigate reaction-induced changes in the detailed internal bond structure of individual oligo-(phenylene-1,2-ethynylenes) on a (100) oriented silver surface as they undergo a series of cyclization processes. Our images reveal the complex surface reaction mechanisms underlying thermally induced cyclization cascades of enediynes. Calculations using ab-initio density functional theory provide additional support for the proposed reaction pathways.

Parts of this chapter have been published in De Oteyza, D. G.; Gorman, P.; Chen, Y.-C.; Wickenburg, S.; Riss, A.; Mowbray, D. J.; Etkin, G.; Pedramrazi, Z.; Tsai, H.-Z.; Rubio, A.; Crommie, M. F.; Fischer, F. R. *Science* **2013**, *340*, 1434–1437.

2.1 Introduction

Understanding the microscopic rearrangements of matter that occur during chemical reactions is of great importance for catalytic mechanisms and might lead to dramatic optimization of industrially relevant processes.[105,106] However, traditional chemical structure characterization methods are typically limited to ensemble techniques where different molecular structures, if present, are convolved in each measurement.[77] This limitation complicates the determination of final chemical products, and often renders such identification impossible for products present only in small amounts. Single-molecule characterization techniques, such as scanning tunneling microscopy (STM),[64,107] potentially provide a means for surpassing these limitations. Structural identification using STM, however, is limited by the microscopic contrast arising from the electronic local density of states (LDOS), which is not always easily related to chemical structure. Another important sub-nanometer-resolved technique is transmission electron microscopy (TEM). Here, however, the high-energy electron beam is often too destructive for organic molecule imaging. Recent advances in tuning-fork-based noncontact atomic force microscopy (nc-AFM) provide a method capable of nondestructive sub-nanometer spatial resolution.[94–96,108,109] Single-molecule images obtained with this technique are reminiscent of wire-frame chemical structures and even allow differences in chemical bond order to be identified.[95] Here we show that it is possible to resolve with nc-AFM the intramolecular structural changes and bond rearrangements associated with complex surface-supported cyclization cascades, thereby revealing the microscopic processes involved in chemical reaction pathways.

2.2 Experimental Design

A suitable system by which to observe the complexities of chemical rearrangements precisely by nc-AFM are the class of molecules which are capable of undergoing thermal pericyclic rearrangements. Enediynes, a class of molecules characterized by alternating triple and double bonds, exhibit a variety of radical cyclization processes known to compete with traditional Bergman cyclizations,[18,110] thus often render numerous products with complex structures that are difficult to characterize using ensemble techniques.[51] Bergman cyclization, a well-studied organic reaction, typically relies on well-controlled reaction conditions to ensure that the desired reaction product is achieved, such as flooding the reaction mixture with quenching agent so as to trap the product before it polymerizes. As seen in Scheme 2.1, enediynes have multiple reaction pathways available to them. Depending upon their substitution pattern, one can force a system to favor one

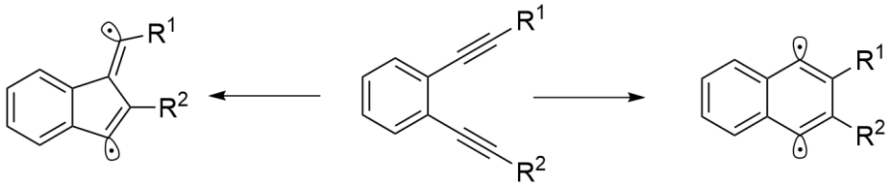

Scheme 2.1 An enediyne molecule is capable of undergoing multiple competing pericyclic reactions. Shown above are C^1–C^5 cyclization (left) and C^1–C^6, or Bergman, cyclization (right). Depending upon substitution patterns, which affect the kinetics of cyclization, the cyclization of the enediyne system can be directed towards the preferred product.

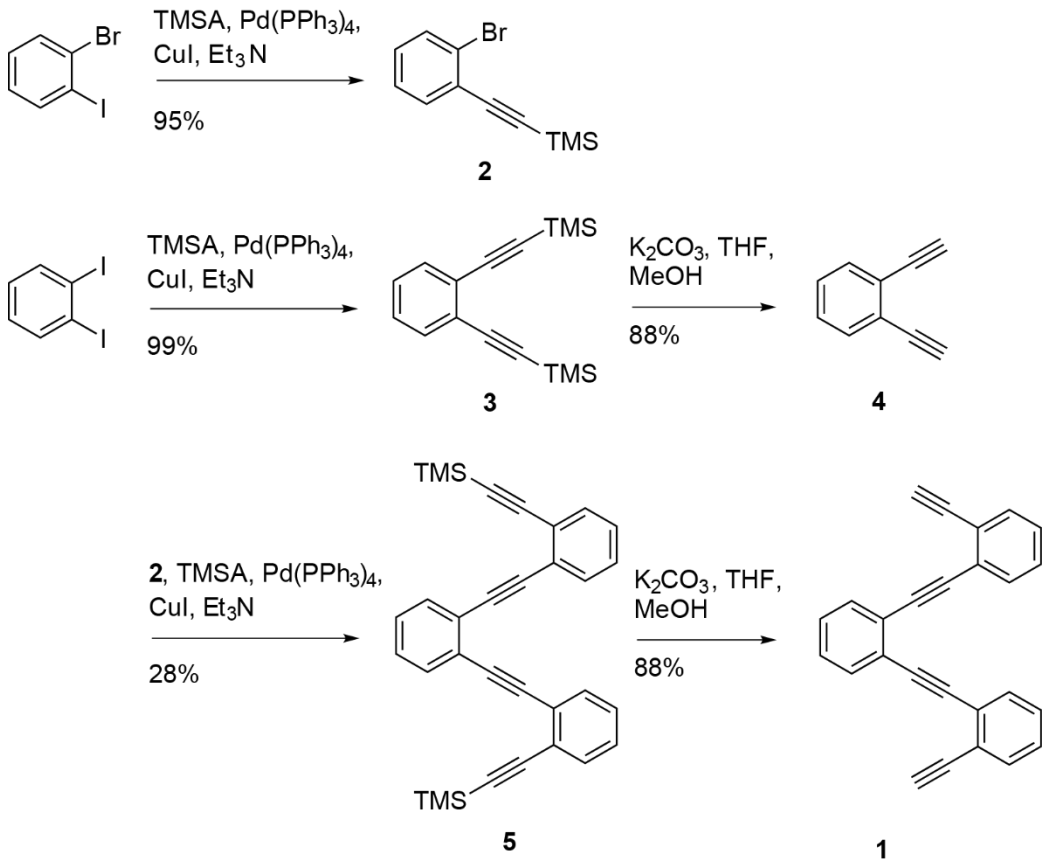

Scheme 2.2 Synthetic route toward 1,2-bis((2-ethynylphenyl)ethynyl)benzene (**1**).

cyclization pathway over another by influencing that cyclizations activation barrier (E_a).[18,111] For example, by simply changing the R group on the acetylene from H to Ph, the E_a of C^1–C^6 rises from 24.6 kcal/mol to 32.9 kcal/mol, whereas the E_a of C^1–C^5 lowers from 37.2 kcal/mol to 35.1 kcal /mol.[17,18,112]

To probe deeper into the complexities of enediyne reactivity, illustrated in Scheme 2.3, we synthesized 1,2-bis((2-ethynylphenyl)ethynyl)benzene (**1**) through convergent iterative Sonogashira cross-coupling reactions (Scheme 2.2). Precursor **2** was synthesized via Sonogashira cross-coupling with one equivalent of trimethysilylacetylene (TMSA). **3** was prepared in a similar fashion via Sonogashira cross-coupling with two equivalents of TMSA. **3** was deprotected with potassium carbonate in a mixture of THF and methanol to yield terminal di-acetylene **4**. Protected bromophenyl acetylene **2** was used in 2 equivalents as coupling partner with **4** to yield trimethylsilyl protected *oligo*-1,2-diethynylbenzene **5** which was subjected to deprotection conditions to yield the target phenylene ethynylene **1**.

As one can see clearly from Scheme 2.3, the chosen molecule **1** will afford ample insight into the preferred rearrangements of a complex enediyne system.

To directly image these products with sub-nanometer spatial resolution, we deposited **1** from a Knudsen cell onto an atomically clean Ag(100) surface held at room temperature under ultrahigh

vacuum (UHV). Molecule-decorated samples were transferred to a cryogenic imaging stage ($T \leq$ 7K) before and after undergoing a thermal annealing step. Cryogenic imaging was performed both in a home-built T = 7 K scanning tunneling microscope and in a qPlus-equipped,[113,114] commercial Omicron LT-STM/AFM at T = 5 K. We used STM and nc-AFM to probe both the reactant and final products at the single molecule level. nc-AFM images were recorded by measuring the frequency shift of the qPlus resonator while scanning over the sample surface in constant-height mode. For nc-AFM measurements, the apex of the tip was first functionalized with a single CO molecule.[94] Our images reveal how the thermally induced complex bond rearrangement of **1** resulted in a variety of unexpected products, from which we have obtained a detailed mechanistic picture. To assess the reaction pathway energetics, we performed *ab initio* DFT calculations within

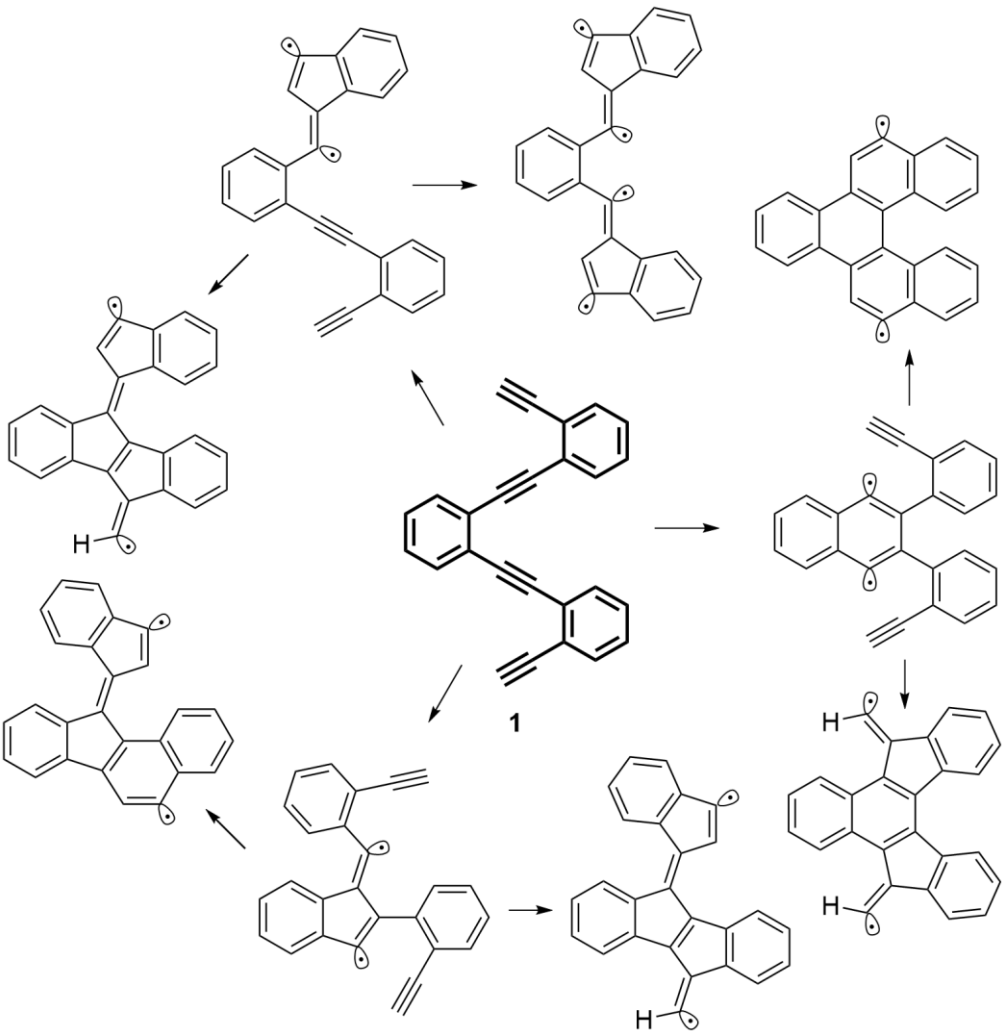

Scheme 2.3 The complex rearrangement of *oligo*-phenylene ethynylene **1**. Shown here, via various conceivable reaction pathways, are six of the many potential products.

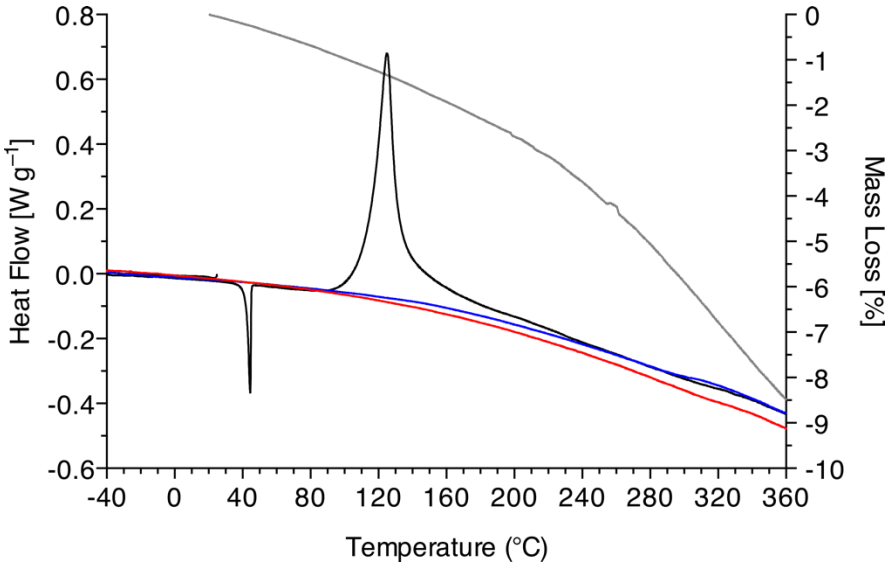

Figure 2.1 DSC and TGA of **1**. Color code: –40 to 360 °C, black, DSC; 360 to –40 °C, blue, DSC; –40 to 360 °C; gray, TGA.

the local density approximation using the Grid-based Projector Augmented Wavefunction (GPAW) method code.[115–117]

2.2.1 Differential Scanning Calorimetry and Thermogravimetric Analysis

In an effort to evaluate the reactivity of the 1,2-diethynylbenzenes upon heating, the thermal properties of **1** were investigated using differential scanning calorimetry (DSC). The trace in Fig. 2.1 shows a sharp endothermal peak at 44 °C associated with the melting point of the sample, and a broad exothermal feature centered around 120 °C characteristic for a thermally induced cyclization process.[45] Repeated cycles of heating and cooling indicate that the latter peak is coupled to an irreversible transformation of **1**. Thermogravimetric analysis (TGA) of the same

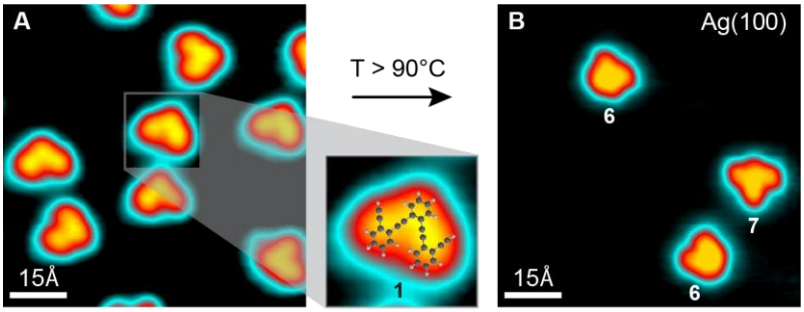

Figure 2.2 (A) Constant current STM image of **1** as deposited on Ag(100) (I = 25 pA, V = 0.1 V, T = 7 K). A model of the molecular structure is overlaid on a close-up STM image. (B) STM image of products **6** and **7** on the surface shown in (A) after annealing at T = 145 °C for 1 minute (I = 45 pA, V = 0.1 V, T = 7 K).

sample indicates only a < 1% mass loss in the temperature range between 100 and 150 °C. We thus conclude that the exothermal peak is not associated with the thermal decomposition of **1**.

2.3 STM and nc-AFM Imaging

Fig. 2.2A shows a representative STM image of **1** on Ag(100) before undergoing thermal annealing. The adsorbed molecules each exhibited three maxima in their LDOS at positions suggestive of the phenyl rings in **1** (Fig. 2.2A). Annealing the molecule-decorated Ag surface up to 80 °C left the structure of the molecules unchanged. Annealing the sample at $T \geq 90$ °C, however, induced a chemical transformation of **1** into distinctly different molecular products (some molecular desorption was observed). Fig. 2.2B shows an STM image of the surface after annealing at 145 °C for 1 min. Two of the reaction products can be seen in this image, labeled as **6** and **7**. The structures of the products are unambiguously distinguishable from one another and from the starting material **1**, as shown in the close-up STM images of the most common products **6**, **7**, and **8** in Figs. 2.3B–D. The observed product ratios are **6** : **7** : **8** = (51 ± 7)% : (28 ± 5)% : (7 ± 3)%

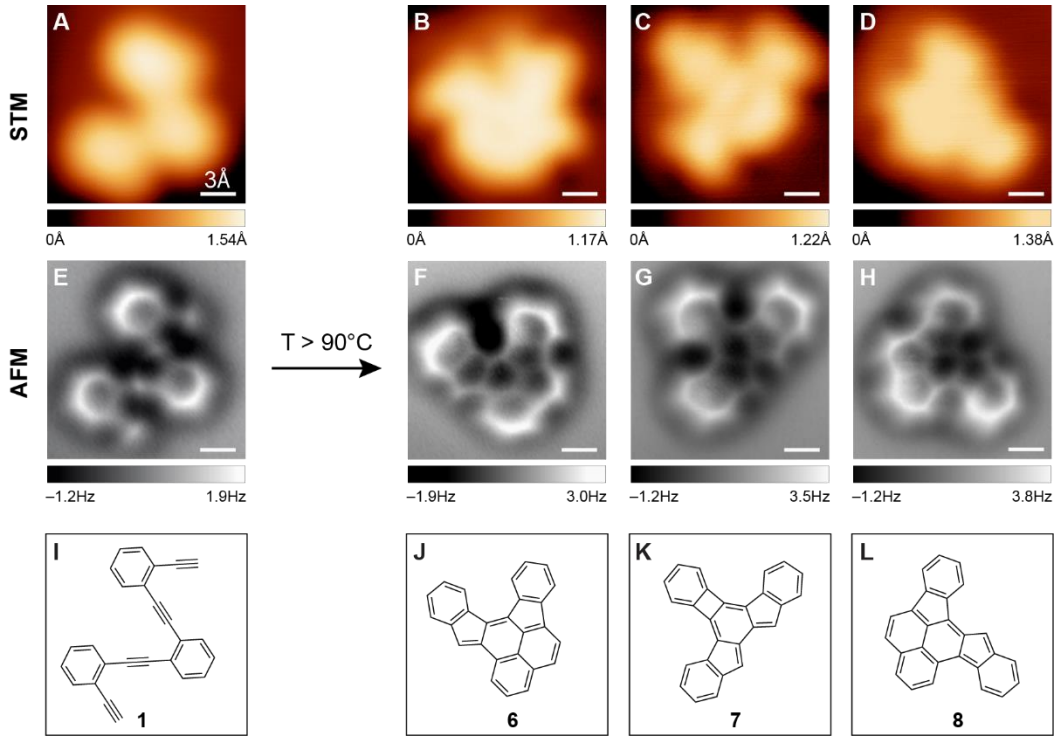

Figure 2.3 Comparison of STM images, nc-AFM images, and structures for molecular reactant and products. (A) STM image of **1** on Ag(100) prior to annealing. (B–D) STM images of individual products **6**–**8** on Ag(100) after annealing at $T > 90$ °C ($I = 10$ pA, $V = -0.2$ V, $T = 5$ K). (E) nc-AFM image of the same molecule (reactant **1**) depicted in (A). (F–H) nc-AFM images of the same molecules (products **6**–**8**) depicted in (B–D). nc-AFM images were obtained at sample bias $V = -0.2$ V (qPlus sensor resonance frequency = 29.73 kHz, nominal spring constant = 1800 N/m, Q-value = 90000, oscillation amplitude = 60 pm). (I–L) Schematic representation of the molecular structure of reactant **1** and products **6**–**8**. All images were acquired with a CO modified tip.

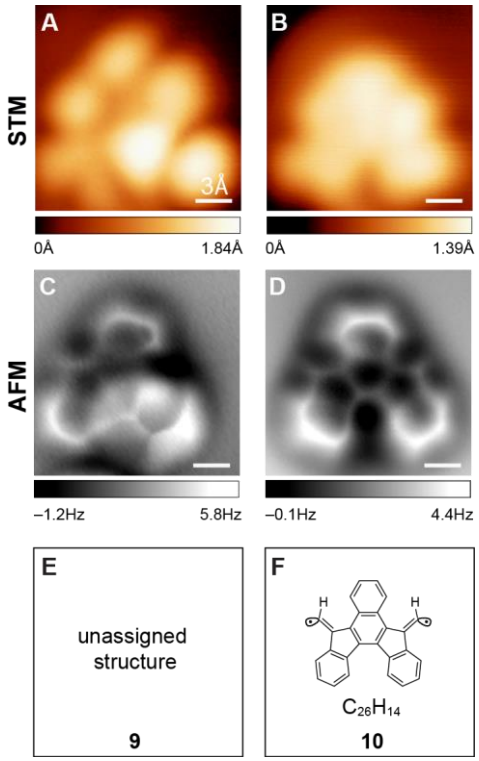

Figure 2.4 STM (A–B) and nc-AFM images (C–D) of the products **9** and **10**. A schematic representation of the proposed molecular structure of **10** is depicted in (F). Imaging parameters were (I = 5 pA, V = –0.066 V), (I = 10 pA, V = –0.2 V), (V = –0.25 V, amplitude = 60 pm) and (V = –0.2 V, amplitude = 70 pm) for A, B, C and D, respectively. For the nc-AFM measurements, the sensor parameters were the following: qPlus sensor resonance frequency = 29.73 kHz, nominal spring constant = 1800 N/m, Q-value = 90000.

with the remaining products comprised of other minority monomers as well as fused oligomers (Figure 2.4).

Detailed sub-nanometer-resolved structure and bond conformations of the molecular reactant **1** and products (**6** to **8**) were obtained by performing nc-AFM measurements of the molecule-decorated sample both before and after annealing at $T \geq 90$ °C. Fig. 2.3E shows a nc-AFM image of **1** prior to annealing. In contrast to the STM image (Fig. 2.3A) of **1**, which reflects the diffuse electronic LDOS of the molecule, the AFM image reveals the highly spatially resolved internal bond structure. A dark halo observed along the periphery of the molecule is associated with long-range electrostatic and van der Waals interactions.[94,118] The detailed intramolecular contrast arises from short-ranged Pauli repulsion, which is maximized in the regions of highest electron density.[118] These regions include the atomic positions and the covalent bonds. Even subtle differences in the electron density attributed to specific bond orders can be distinguished,[95] as evidenced by the enhanced contrast at the positions of the triple bonds within **1**. This effect is to be distinguished from the enhanced contrast observed along the periphery of the molecule, where

spurious effects (e.g. because of a smaller van der Waals background, enhanced electron density at the boundaries of the delocalized π-electron system, and molecular deviations from planarity) generally influence the contrast.[95,118]

Figs. 2.3F–H show sub-nanometer-resolved nc-AFM images of reaction products **6** to **8** that were observed after annealing the sample at $T > 90$ °C. The structure of these products remained unaltered even after further annealing to temperatures within the probed range from 90 °C to 150 °C (150 °C was the maximum annealing temperature explored in this study). The nc-AFM images reveal structural patterns of annulated six-, five-, and four-membered rings. The inferred molecular structures are represented in Figs. 2.3J–L. Internal bond lengths measured by nc-AFM have previously been shown to correlate with Pauling bond order,[95] but with deviations occurring near a molecule's periphery, as described above. As a result, we could extract clear bonding geometries for the products (Figs. 2.3J–L), but not their detailed bond order. The subtle radial streaking extending from the peripheral carbon atoms suggests that the valences of the carbon atoms are terminated by hydrogen.[118] This is in agreement with molecular mass conservation for all proposed product structures and indicates that the chemical reactions leading to products **6** to **8** are exclusively isomerization processes. (Fig. 2.3G suggests a 4-membered ring between two 6-membered rings, but does not resolve it perfectly. DFT calculations indicate that other structural isomers, such as an 8-membered ring next to a 6-membered ring, are energetically very unfavorable compared to the structure of **7**). Images of other minority products (**9** and **10**) are included in Fig. 2.4. The bonding structure of **9** is non-planar and thus leads to a complex contrast in the nc-AFM images that hampers direct structure determination. Product **10** is the result of two C^1–C^5 cyclizations on the sterically less hindered outer enediynes in combination with a C^1–C^6 cyclization on the inner enediyne. The AFM contrast of the terminal carbon atom in the C=C bonds of **10** is lower than expected. We attribute this to a molecular distortion resulting from the stabilizing interaction between the Ag surface and the terminal sp^2 carbon centered radicals.[119] DFT calculations indicate that the carbon atom on the exocyclic double bond comes to lie closer to the Ag surface.

2.4 Reactivity and Reactive Pathways from 1 to Products

Our ability to directly visualize the bond geometry of the reaction products (Figs. 2.3F–H) provides insight into the detailed thermal reaction mechanisms that convert **1** into the products. We now limit our discussion to the reaction pathways leading from **1** to the two most abundant products, **6** and **7**. The reactivity of *oligo*-1,2-diethynylbenzene **1** can be rationalized by treating the 1,2-diethynylbenzene subunits as independent but overlapping enediyne systems that are either substituted by two phenyl rings for the central enediyne, or by one phenyl ring and one hydrogen atom in the terminal segments. This treatment suggests three potential cyclizations along the reaction pathway (resulting in 6-membered, 5-membered, or 4-membered rings),[17] in addition to other possible isomerization processes such as [1,2]-radical shifts or bond rotations that have been observed in related systems.[112] Combinations of these processes leading to the products in a minimal number of steps were explored and analyzed using DFT calculations. (Fig. 2.6)

2.4.1 Description of DFT calculations

All DFT calculations were performed using the real-space projector augmented wavefunction (PAW) method as implemented in the GPAW software package.[116,117] We employ the local density approximation (LDA) [115] to the exchange and correlation (xc)-functional. Note that differences between the energetics obtained within the local density approximation (LDA),

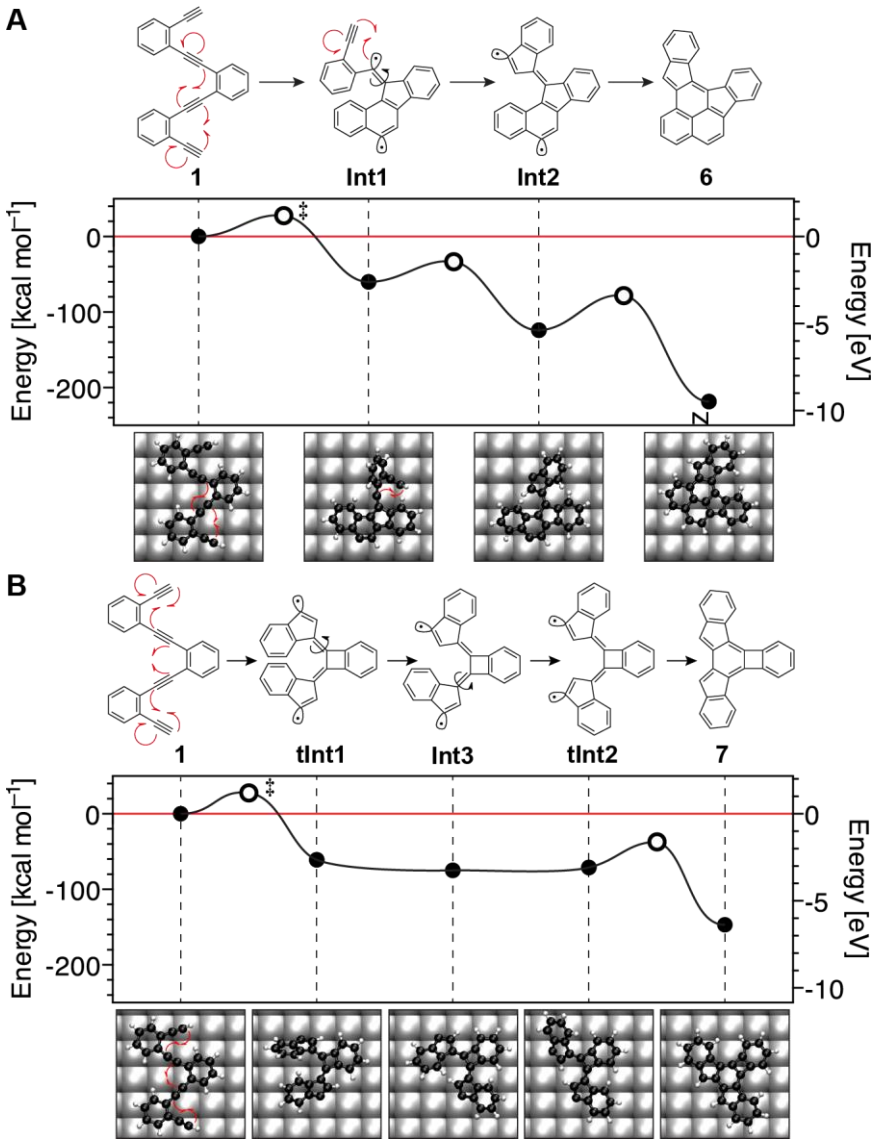

Figure 2.5 Proposed pathways for the cyclization of reactant **1** into (A) product **6** and (B) product **7** on Ag(100). Energies for **1**, **6**, and **7** (filled circles), intermediates **Int1**–**Int3**, **tInt1**, and **tInt2** (filled circles), and reaction barriers (open circles) as calculated using ab initio DFT theory. 3D-models show the non-planar structure of intermediates. (‡) rate-determining transition state; red line, reference energy of **1** on Ag(100).

generalized gradient approximation (GGA), or range-separated hybrid xc-functionals are expected to be an order of magnitude smaller than the energy of the most weakly bound transition state relative to the reactant following the initial cyclization for each reaction pathway. Further, the LDA often provides superior bond length and geometry predictions compared to more computationally expensive methods, such as GGAs and hybrids. This suggests that LDA results are sufficiently accurate for describing the chemical processes under consideration.[120]

We perform Γ point calculations using a grid spacing of h = 0.2 Å, an electronic temperature of k_BT = 0.1 eV with all energies extrapolated to T = 0 K, and relax all molecular structures until a maximum force below 0.05 eV/Å is obtained. Adsorption on the Ag(100) surface is modeled using a 6×6×3 slab fixed to the experimental coordinates obtained from a lattice parameter for Ag of 4.09 Å, and including more than 12 Å of vacuum between the molecular layer and the repeated image of the Ag(100) slab. The 6×6×3 slab provides at least 4 Å of separation between repeated molecular images in the surface plane. We find these values are sufficient to converge both energy differences and the electron density for the systems under consideration.

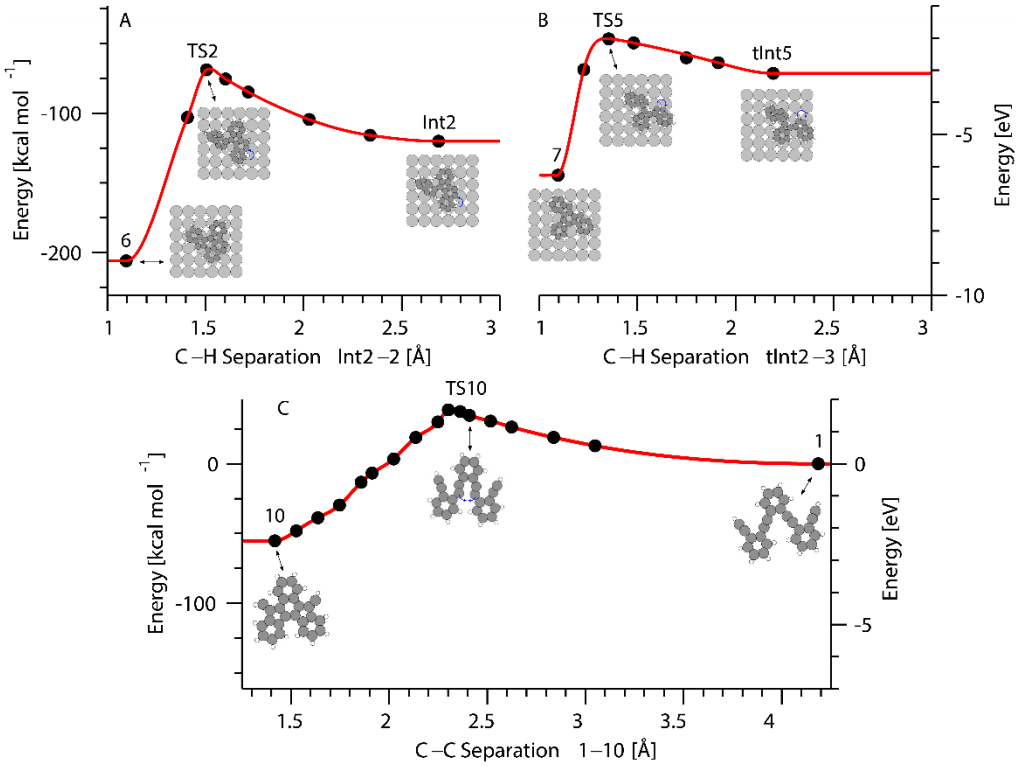

Figure 2.6. Schematics and energies versus C–H separation in Å for (A) [1,3]-hydrogen shift from **Int2** to product **6**, (B) [1,2]-hydrogen shift from **tInt2** to product **7** and versus C–C separation in Å for (C) the initial cyclization from **1** to product **10**. Hydrogen shifts and cyclizations are marked in blue.

2.4.2 Results of DFT Modeling

We started by calculating the total energy of a single adsorbed molecule of the reactant **1** on a Ag(100) surface. Activation barriers and the energy of metastable intermediates were calculated (including molecule-surface interactions) for a variety of isomeric structures along the reaction pathway leading toward the products **6** and **7**. Our observations that the structure of reactants on Ag(100) remains unchanged for $T < 90$ °C and that no reaction intermediates can be detected among the products indicates that the initial enediyne cyclization is associated with a notable activation barrier that represents the rate-determining step in the reaction. In agreement with experiments, DFT calculations predict an initial high barrier for the first cyclization reactions, followed by a series of lower barriers associated with subsequent bond rotations and hydrogen shifts.

Fig. 2.5A shows the reaction pathway determined for the transformation of **1** into product **6**. The rate-determining activation barrier is associated with a C^1–C^6 Bergman cyclization of a terminal enediyne coupled with a C^1–C^5 cyclization of the internal enediyne segment to give the intermediate diradical **Int1** in an overall exothermic process (–60.8 kcal mol^{-1}). Rotation of the third enediyne subunit around a double bond, followed by the C^1–C^5 cyclization of the fulvene radical with the remaining triple bond leads to **Int2**. The rotation around the exocyclic double bond is hindered by the Ag surface and requires the breaking of the bond between the unsaturated valence on the sp^2 carbon atom and the Ag. Yet, the activation barrier associated with this process does not exceed the energy of the starting material used as a reference. The formation of three new carbon-carbon bonds and the extended aromatic conjugation stabilize **Int2** by –123.9 kcal mol^{-1} relative to **1**. Lastly, a sequence of radical [1,2]- and [1,3]-hydrogen shifts followed by a C^1–C^6 cyclization leads from **Int2** directly to the dibenzofulvalene **6**. Our calculations indicate that the substantial activation barriers generally associated with radical hydrogen shifts in the gas phase (50–60 kcal mol^{-1})[85,121] are lowered through the stabilizing effect of the Ag atoms on the surface, and thus, do not represent a rate-limiting process (Fig. 2.5A).

The reaction sequence toward **7** is illustrated in Fig. 2.5B. The rate-determining first step involves two C^1–C^5 cyclizations of the sterically less hindered terminal enediynes to yield benzofulvene diradicals. The radicals localized on the exocyclic double bonds subsequently recombine in a formal C^1–C^4 cyclization to yield the four-membered ring in the transient intermediate **tInt1**. This process involves the formation of three new carbon-carbon bonds, yet it lacks the aromatic stabilization associated with the formation of the naphthyl fragment in **Int2** and is consequently less exothermic (–60.7 kcal mol^{-1}). A sequence of bond rotations transforms **tInt1** via **Int3** into **tInt2**. Alignment of the unsaturated carbon valences in diradical **tInt1** with underlying Ag atoms maximizes the interaction with the substrate and induces a highly non-planar arrangement, thereby making subsequent rotations essentially barrierless. [1,2]-hydrogen shifts and a formal C^1–C^6 cyclization yield the biphenylene **7**.

Transition states have been obtained by fixing the length of the bond to be broken or formed and relaxing the geometry. We stretch the bond in steps of 0.1 Å until a maximum in energy, i.e. the bond length for the transition state, is found. For hydrogen shifts these calculations must include

Structure	Energy [eV]	Energy [kcal mol^{-1}]	Charge [*e*]
1	0	0	–0.48
Int1	–2.64	–60.8	–0.70
Int2	–5.37	–123.9	–0.79
TS2	–3.39	–78.2	–0.87
6	–9.47	–218.4	–0.62
tInt1	–2.63	–60.7	–0.68
Int3	–3.25	–74.9	–0.77
tInt2	–3.08	–71.0	–0.66
TS3	–1.63	–37.5	–0.85
7	–6.36	–146.7	–0.58
TS10	1.13	25.9	–0.75
10	–5.04	–116.1	–0.68

Table 2.1. Energy in eV and kcal mol^{-1} and charge in *e* of each molecular structure considered.

the Ag(100) surface explicitly, as the transition may be surface mediated, e.g. the [1,3]-hydrogen shift on **Int2**. As we are first searching for the fixed bond length which describes the transition state, rather than its energy, we may employ a simplified 6×6×1 slab model for the Ag(100) surface. On the other hand, when forming C bonds, the surface plays less of a role in determining the bond length which describes the transition state. To model the first cyclization barrier, we have used gas phase calculations for the reaction pathway from reactant **1** to product **10**. These methods allow us to quickly obtain the required bond length for the transition state, which we then employ within a 6×6×3 slab model to obtain accurate transition state energies. The transition state energies as a function of bond length are shown in Fig. 2.6 for the (A) [1,3]-hydrogen shift, (B) [1,2]-hydrogen shift, and (C) first cyclization step along with schematics of the initial, transition, and final states. The initial cyclizations along the pathways towards products **6** or **7** are expected to be energetically similar, as concluded from the comparable product distribution after annealing to different temperatures. The calculated transition state energy for the initial cyclization is furthermore in good agreement with estimations from the 90 °C threshold temperature observed

experimentally, in combination with an Arrhenius function and typical attempt frequencies on the order of 10^{13} Hz.

Estimations of the barriers associated with the bond rotations along the transformation pathways from **1** to **6** and **7** are obtained as follows. In step **Int1**–**Int2** the Ag surface hinders the rotation. We therefore estimate an upper limit for the barrier from the energy required to break the bond between the unsaturated C-atom and the Ag while tilting the molecule far enough to allow an unhindered bond rotation. A different scenario appears for the sequence of bond rotations transforming **tInt2** via **Int3** into **tInt2**. In this case, **tInt1** maximizes the interaction with the substrate having its unsaturated C radicals pointing towards the Ag surface in a highly non-planar arrangement and thereby makes the subsequent rotations essentially barrierless.

The charge transfer between the Ag(100) surface and the adsorbed molecules is estimated by applying the Bader partitioning scheme [122] to the all-electron density obtained from DFT. This level of theory has recently been shown to describe charge transfer for large molecules on Ag quite accurately.[123] The energy in eV and kcal mol^{-1} and the charge in *e* for reactant **1**, **Int1**–**Int3**, **tInt1**, **tInt2**, and products **6**–**7** is provided in Table 2.1.

Both reaction pathways toward **6** and **7** involve C^1–C^5 enediyne cyclizations. These are generally energetically less favorable compared to the preferred C^1–C^6 Bergman cyclizations,[17] but factors such as the steric congestion induced by substituents on the alkynes,[17,18] the presence of metal catalysts,[124] or single-electron reductions of enediynes [125,126] have been shown to sway the balance toward C^1–C^5 cyclizations yielding benzofulvene diradicals. All three of these factors apply to the present case of the thermally induced cyclization of **1** on Ag(100) [e.g., bulky phenyl substituent on C^1 and C^6, a metallic substrate, and a charge transfer of 0.5 electrons from the substrate to **1**] thus facilitating the C^1–C^5 cyclizations. The precise order of the low-energy processes (such as the **Int3**/**tInt2** rotation and the **tInt2**/**7** [1,2]-hydrogen shifts) following the rate-limiting initial cyclizations cannot be strictly determined experimentally. However, the sequence does not change the overall reaction kinetics and thermodynamics discussed above. Our bond-resolved single-molecule imaging thus allows us to extract an exhaustive picture and unparalleled insight into the chemistry involved in complex enediyne cyclization cascades on Ag(100) surfaces. This detailed mechanistic understanding in turn guides the design of precursors for the rational synthesis of functional surface-supported molecular architectures.

Direct Imaging of Covalent Bond Structure in Single Molecule Chemical Reactions

Chapter 3

Local Electronic Structure of Oligo-Acetylene Derivatives Formed Through Radical Cyclizations at a Surface

Semiconducting π-conjugated polymers have attracted significant interest for applications in light-emitting diodes, field-effect transistors, photovoltaics, and nonlinear optoelectronic devices. In this work we characterize the chemical and electronic structure of individual chains of oligo-(E)-1,1'-bi(indenylidene), a poly-acetylene derivative that we have obtained through cooperative C^1–C^5 thermal enediyne cyclizations on Au(111) surfaces followed by a step-growth polymerization of the (E)-1,1'-bi(indenylidene) diradical intermediates. We have determined the combined structural and electronic properties of this class of oligomers by characterizing the atomically precise chemical structure of individual monomer building blocks and oligomer chains (via non-contact atomic force microscopy (nc-AFM)), as well as by imaging their localized and extended molecular orbitals (via scanning tunneling microscopy and spectroscopy (STM/STS)). Our combined structural and electronic measurements reveal that the energy associated with extended π-conjugated states in these oligomers is significantly lower than the energy of the corresponding localized monomer orbitals, consistent with theoretical predictions.

Parts of this chapter have been published in Riss, A.; Wickenburg, S.; Gorman, P.; Tan, L. Z.; Tsai, H.-Z.; de Oteyza, D. G.; Chen, Y.-C.; Bradley, A. J.; Ugeda, M. M.; Etkin, G.; Louie, S. G.; Fischer, F. R.; Crommie, M. F. *Nano Lett.* **2014**, *14*, 2251–2255.

Local Electronic Structure of Oligo Acetylene Derivatives Formed Through Radical Cyclizations at a Surface

3.1 Introduction

Conjugated polymers have attracted considerable interest into their fundamental properties as well as their potential for industrial applications.[53–55] Their tunable electronic structure makes them a useful material for applications in the fields of molecular electronics and photonics.[56–58] Numerous chemical reactions yielding conjugated polymers have been adapted for the synthesis of well-defined molecular wires on surfaces.[59–69] These reactions include Ullmann-type cross-coupling,[62–64] diyne polymerization,[65,66] and alkyne homocoupling,[69] most of which require catalytically active metal substrates to facilitate polymerization. Thermally-induced enediyne cyclization on surfaces,[83,90] a newer polymerization technique, has received increased attention due to its greater flexibility regarding non-catalytic growth substrates. Effective utilization of carbon-based nanostructures resulting from these reactions requires the development of synthetic tools to control the chemical and electronic structure of the polymer products. Of particular importance for advanced electronics applications[70] is the formation of polymeric structures featuring extended π-conjugation during the growth process from small-molecule building blocks.

Here we report the synthesis and characterization of individual chains of *oligo*-(*E*)-1,1'-bi(indenylidene)[127] obtained through a thermally induced cooperative C^1–C^5 radical cyclizations of enediyne precursors followed by step-growth polymerization on Au(111). We have gained substantial insight into the relationship between chemical structure and electronic properties in these oligomers by utilizing nc-AFM to determine the precise atomic-scale structure of enediyne starting material, cyclized monomers, and covalently linked oligomeric chains, while simultaneously utilizing STM/STS measurements to probe the localized and extended electronic states of these species (including orbital energies). These measurements help us to understand the oligomer formation reaction mechanism and show that the development of oligomer extended electronic states can be rationalized as the result of an efficient π-orbital overlap between monomer building blocks. Increased spatial delocalization is associated with a decrease in oligomer electronic energy, as confirmed by our theoretical simulations.

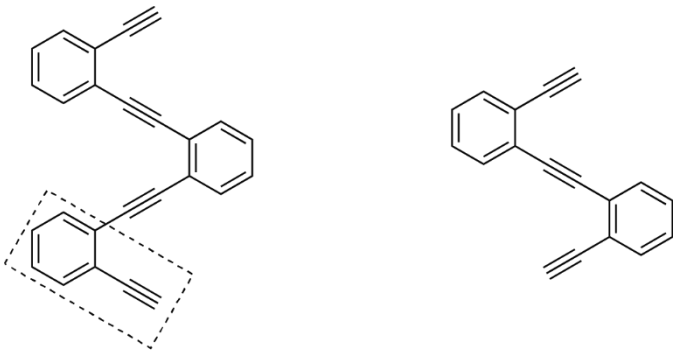

1 **11**

Scheme 3.1 By limiting the number of ethynylbenzene units (dashed box) within the structure of the target product, we can inherently decrease the degrees of freedom our product may access while undergoing cyclization reactions during the thermal annealing process.

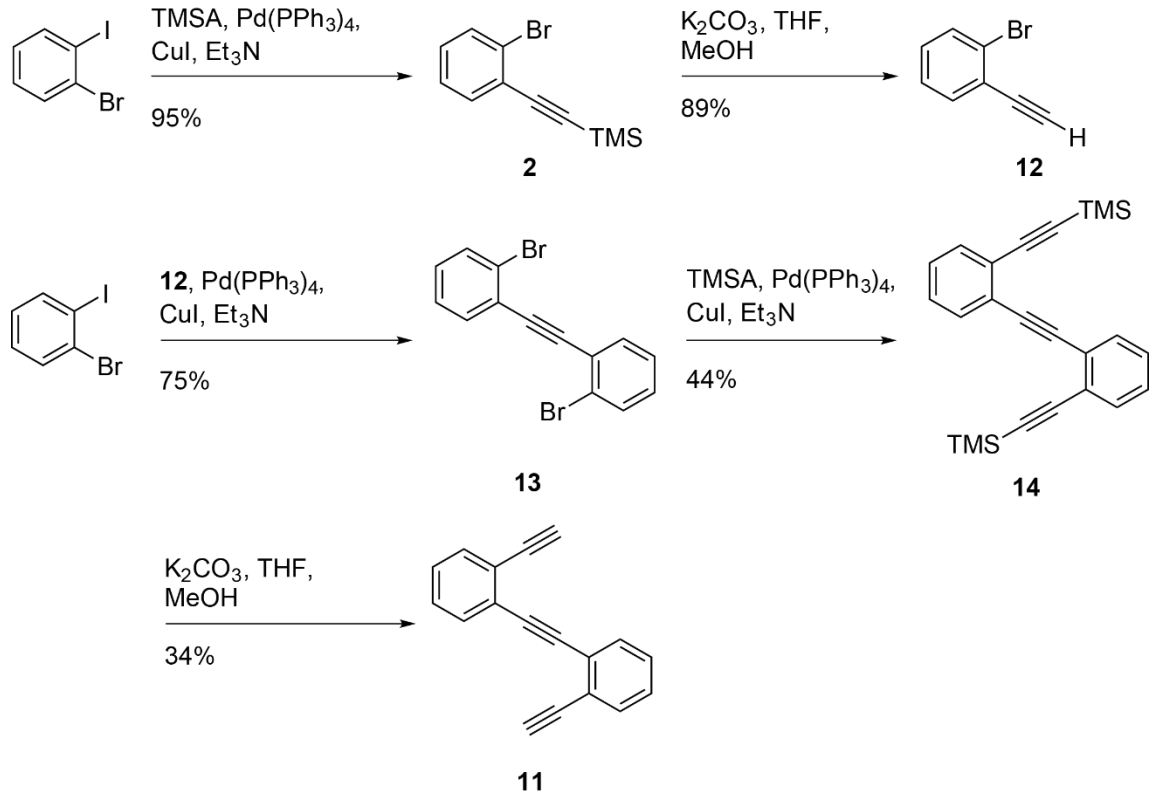

Scheme 3.2 Synthetic route toward 1,2-bis(2-ethynylphenyl)ethyne (**11**).

3.2 Experimental Design

Drawing from insights outlined in Chapter 2, a suitable small molecule precursor was designed to examine thermally induced cyclization and subsequent polymerization of short chain phenylene ethynylene molecules. This molecule, by design would have to have fewer ethynylbenzene units (Scheme 3.1, dashed box) than product **1** so as to have fewer degrees of reactional freedom available (Scheme 3.1). With that in mind, the enediyne precursor 1,2-bis(2-ethynylphenyl)ethyne (**11**) (Scheme 3.2) was designed and synthesized through iterative Sonogashira cross-coupling reactions. Precursor **2** was synthesized via Sonogashira cross-coupling with one equivalent of trimethysilylacetylene (TMSA) which was then deprotected to yield precursor **12**. Sonogashira coupling between **12** and 2-bromo-1-iodobenene yielded diphenylacetylene **13**. Sonogashira coupling between **13** and two equivalents of TMSA yielded precursor **14** which was subsequently deprotected to yield product phenylene ethynylene **11**.

11 was deposited in ultra-high vacuum onto a Au(111) surface held at room temperature (T = 293 K). Cryogenic nc-AFM measurements (T = 4 K) (Fig. 1a) reveal that **11** adopts two conformational isomers on the surface: a C_{2h} symmetric *trans*-conformation (Fig. 3.1b) and a C_{2v} symmetric *cis*-conformation (Fig. 3.1c). The atomic structure of the phenyl rings and the positions of the single and triple bonds are clearly resolved in the nc-AFM image. Contrast in nc-AFM measurements at

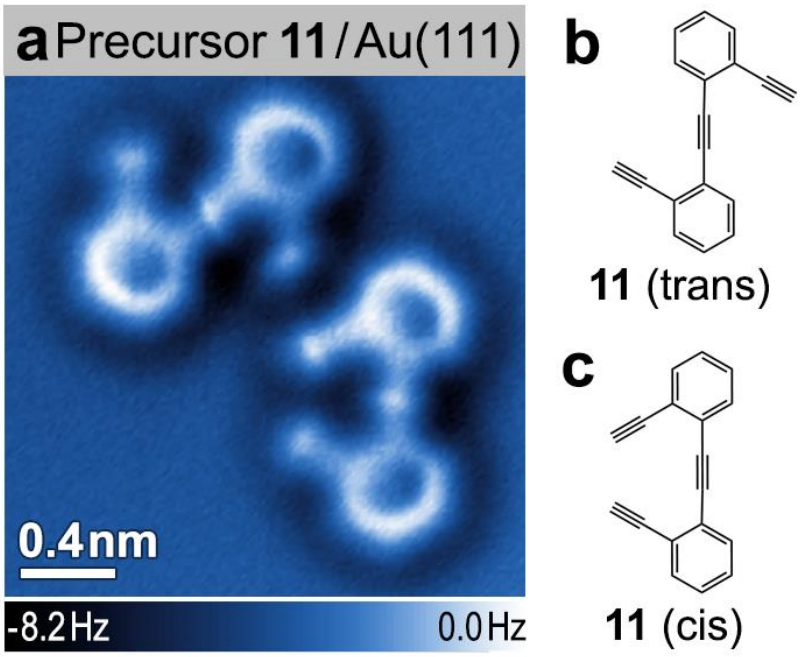

Figure 3.1 Precursor molecule **11**. (a) nc-AFM image of the two conformational isomers of **11** on Au(111) (T = 4 K; tip height corresponds to tunnel current set point Vs = 50 mV and I = 10 pA); Schematic representation of (b) *trans* conformation and (c) *cis* conformation.

the small oscillation amplitudes used here (60 pm) is dominated by short-range chemical forces that arise from repulsive interactions between the CO functionalized AFM tip and molecular adsorbates on the surface.[113] This imaging technique allows precise spatial resolution of surface-bound atoms and bonds at a level that is not attainable by other surface probes,[83,94,95] as indicated by comparison of the nc-AFM image in Fig. 3.1a to the wire-frame structures in Figs. 3.1b,c.

3.3 Inducing Polymer Growth via Thermal Annealing

Thermal annealing of a Au(111) surface decorated with a sub-monolayer coverage of **11** at 160 °C induces two intramolecular C^1–C^5 radical cyclization reactions as well as intermolecular carbon-carbon coupling reactions between monomer units. Following this annealing step more than 70% of the material on the surface becomes part of covalently linked molecular assemblies with lengths $n \geq 3$ (where "n" denotes the number of monomer subunits). As depicted in the nc-AFM image of Fig. 3.4a, the most common structures observed are covalently linked *oligo*-(*E*)-1,1'-bi(indenylidene) chains (an *oligo*-acetylene derivative) containing the common monomer subunit **11′** (Fig. 3.4b, dashed box). Most chains are composed of 5 to 10 monomer units, but sometimes exceed 20. Defect-free translational symmetry along the oligomer backbones is typically retained over segments of three to five monomers. While **11′** (Fig. 3.4b, dashed box) is representative of the dominant monomer incorporated into extended oligomer chains, other monomer subunits were also observed within the chains (See Figs. 3.2 and 3.3).

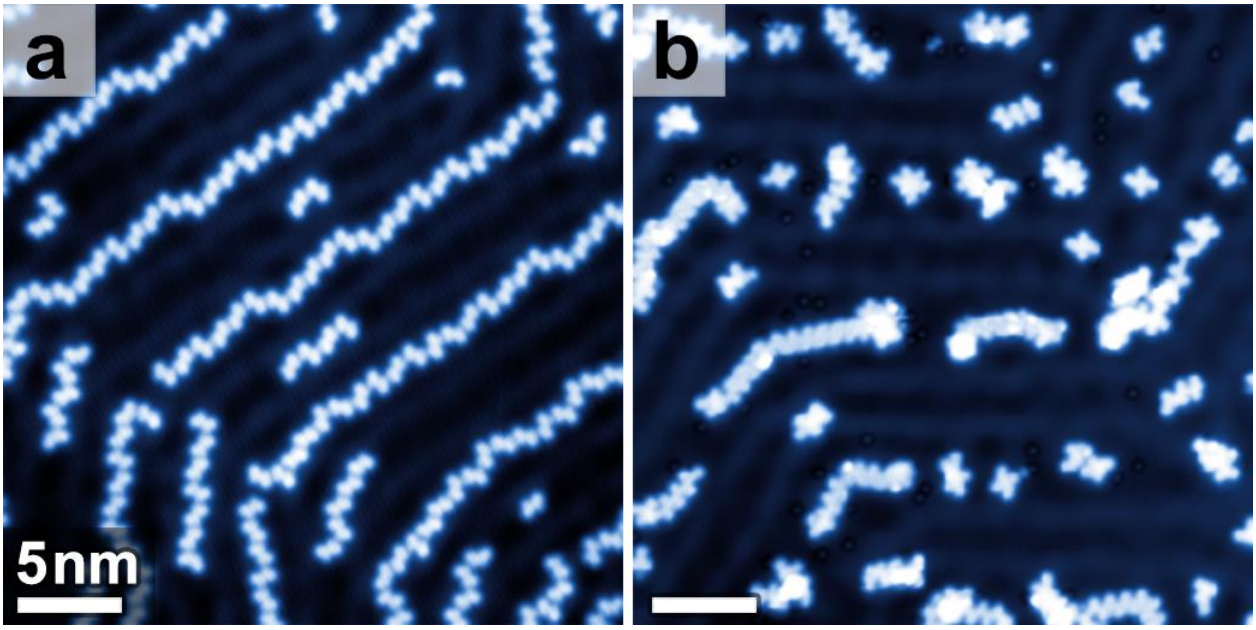

Figure 3.2 (a) STM image of precursor molecules (**11**) adsorbed onto Au(111) before annealing. The herringbone reconstruction of Au(111) leads to a one-dimensional arrangement of the molecules (V_s = 50 mV, I = 50 pA). (b) STM image of the surface after annealing precursor molecules on Au(111) to 160 °C for 5 minutes shows the formation of oligomer chains and shorter molecular adducts (V_s = 50 mV, I = 10 pA).

nc-AFM imaging of the atomic structure of the oligomer chains (Fig. 3.4a) reveals that the π-conjugated carbon-carbon double bonds along the backbone exhibit alternating lengths. Bonds between five-membered rings alternate in length and are marked by red arrows (short bonds) and green arrows (long bonds) in the image. A schematic representation of the alternating pattern of short (C=C) and long (C–C) carbon-carbon bonds along the conjugated backbone is depicted in Fig. 3.4b. The shorter (double) bonds between indenyl groups appear to be roughly 50% of the length of the longer (single) bonds (for the tip-sample distance used to obtain the image in Fig. 3.4a). It is important to note that while our nc-AFM measurement correctly identifies alternating trends in bond lengths, the magnitude of this effect is greatly exaggerated by this imaging technique.[95] Bonds within the five-membered rings are also seen to exhibit a bond length modulation. In particular, the double bonds in indenyl end-groups show a distinctive deviation compared to indenyl groups along the extended oligomer chain (Fig. 3.4a).

Our STM spectroscopy of *oligo*-(*E*)-1,1'-bi(indenylidene) reveals that the electronic structure of the covalently-linked oligomer chains exhibits extended-state behavior (Fig. 3.5). An AFM image of a representative oligomer chain on the Au(111) surface is depicted in Fig. 3.5a along with the STM dI/dV spectrum (Fig. 3.5d) measured at one point along the backbone of the oligomer chain (dI/dV measurement reflects the electronic local density of states (LDOS) at the energy selected

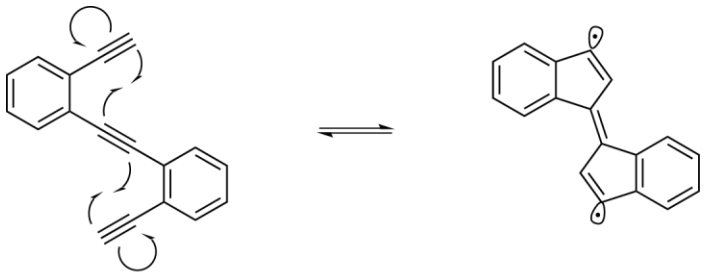

11 **11′**

Scheme 3.2 Two C^1–C^5 thermal enediyne cyclizations convert precursor **11** to monomer **11′**.

by the tip-sample bias). A well-defined electronic resonance is observed at an energy approximately 0.125 V above E_F (blue arrow) compared to the d*I*/d*V* spectrum on bare Au(111). A d*I*/d*V* spatial map of the oligomer chain at a tip bias of 0.125 V (Fig. 3.5b) reveals that the intensity of this state is localized along the oligomer backbone and extends continuously along the full length of the π-conjugated chain (excluding the ends, which are often composed of different types of monomer subunits). This extended-state spatial distribution was observed for all imaged oligomer chains composed of monomer units **11′**.

Isolated monomer building blocks **11′** not incorporated into oligomeric structures were observed to coexist with the chains on the Au(111) surface. These monomers account for a few percent of the material on the surface (other monomer structures have also been observed). Figure 3.6a depicts a nc-AFM image of an isolated (*E*)-1,1'-bi(indenylidene) monomer. Isolated monomer building blocks **11′** exhibit a geometry that resembles the indenyl end-groups in oligomer chains (Fig. 3.4a, bottom), including the presence of highly distorted five-membered rings (such distortion might arise due to the interaction of a radical with the surface[128]). The electronic structure of bi(indenylidene) monomers **11′** was characterized by STM spectroscopy. The d*I*/d*V* spectrum measured on an isolated (*E*)-1,1'-bi(indenylidene) monomer and the corresponding spectrum of the bare Au(111) surface are depicted in Fig. 3.6d. A prominent resonance at V_s = 1.2 V (blue arrow) marks the lowest unoccupied molecular orbital (LUMO) of the molecule adsorbed on the Au(111) surface. The spatial distribution of this molecular electronic state was imaged using d*I*/d*V* mapping (Fig. 3.6b).

The combination of nc-AFM and STM spectroscopy measurements on individual oligomer chains and small molecule precursors reveals both the underlying reaction mechanism that leads to the formation of *oligo*-(*E*)-1,1'-bi(indenylidene), as well as the origin of the oligomer electronic structure. Two thermally induced intramolecular C^1–C^5 enediyne cyclizations of **11** yield the monomer building-block **11′** that has been observed on the surface (Fig. 3.6). This highly reactive 3,3'-diradical intermediate diffuses along the Au(111) surface and recombines with other monomers in a step-growth process. While theoretical models in the gas phase have reported an

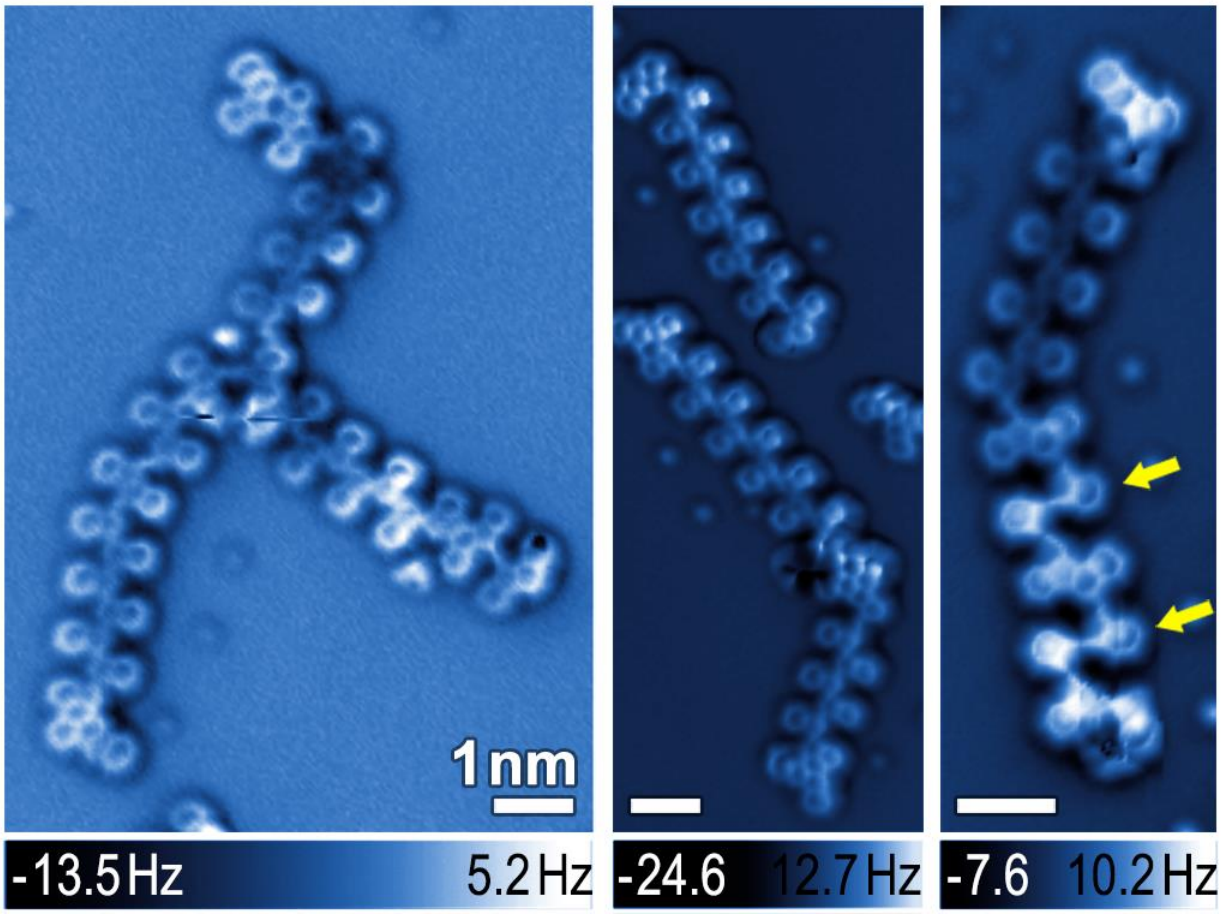

Figure 3.3 nc-AFM images of oligomer chains on Au(111) (T = 4K) formed after thermally-induced reactions starting from molecular precursor **11**. Oligomers of different length are found, as well as other short species. Yellow arrows mark uncyclized molecules (**11**) observed within an oligomer chain.

activation barrier of ~40 kcal mol^{-1} for the C^1–C^5 cyclization of benzannulated enedyines,[17] we have previously shown that metal surface-supported C^1–C^5 cyclizations can proceed at temperatures below 100 °C.[83] In some oligomer chains we have observed uncyclized precursor molecules **11** that are covalently linked via their terminal alkyne carbon atoms (Fig. 3.3). We attribute this structural defect to the reaction of a radical at the end of the growing *oligo*-(*E*)-1,1'-bi(indenylidene) chain with a terminal alkyne carbon atom of an uncyclized building block **11**.

The electronic structure of the *oligo*-acetylene derivative *oligo*-(*E*)-1,1'-bi(indenylidene) can be understood as a consequence of spatial delocalization caused by extended conjugation of π-

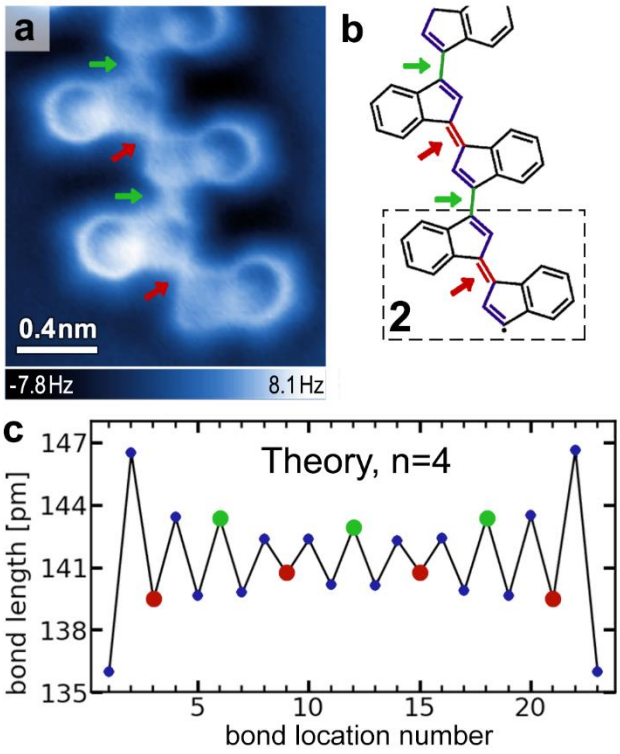

Figure 3.4 Oligomer containing monomer **11′** subunits. (a) nc-AFM image of an oligomer chain on Au(111) (T = 4 K; tip height corresponds to tunnel current set point Vs = 50 mV and I = 30 pA). (b) Schematic representation of chemical structure of the oligomer in (a). Arrows indicate short (red) and long (green) bonds between indenyl groups. Dashed box shows monomer structure **11′**. (c) DFT calculated bond lengths for a 4-unit oligomer chain (composed of units of **11′** as seen in (b)) as a function of the location of the bond along the chain. Red and green dots indicate short and long bonds between indenyl groups, while blue dots indicate bonds within the five-membered rings (calculation shown for an oligomer chain having unsaturated radical valences at the chain ends; results are similar for hydrogen-terminated chains).

systems between monomer building blocks. While an individual monomer exhibits localized electronic states separated by a large energy gap, the efficient π-overlap between monomer orbitals in the oligomer chains results in the formation of lower energy extended states. This behavior is evident in the spectroscopic data in Figs. 3.5 and 3.6, where the LUMO of an isolated monomer lies ~1.1 eV higher in energy than the extended state (relative to E_F).

These conclusions were confirmed by GW calculations[129,130] performed to model both an isolated monomer **11′** and an n = 4 oligomer chain having the same structure indicated by the partial wireframe image (orange overlay) in Figs. 3.5a-c. The calculated LDOS of the isolated monomer LUMO is depicted in Fig. 3.6c. It closely resembles the experimental dI/dV map (Fig. 3.6b), with

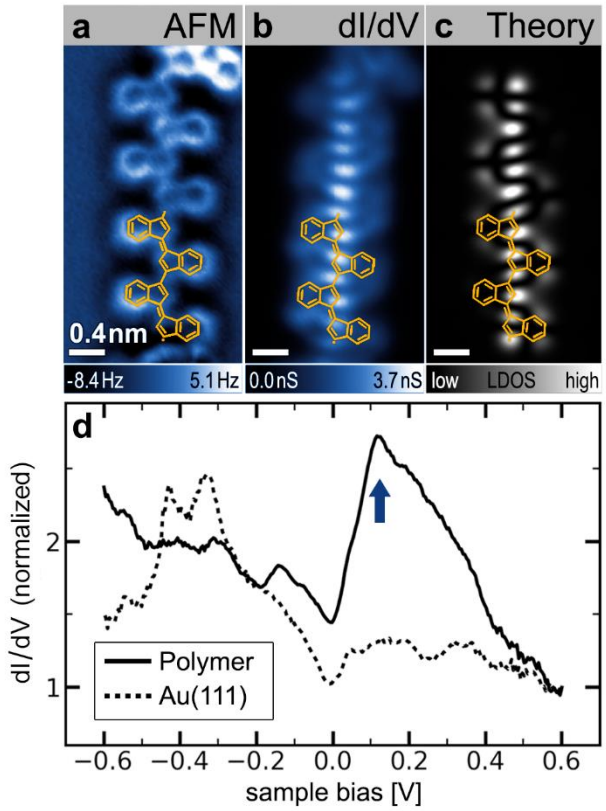

Figure 3.5 Electronic structure of an individual oligomer. (a) nc-AFM image of oligomer chain (tip height corresponds to tunnel current set point *V*s = 50 mV and *I* = 20 pA). (b) Experimental STM d*I*/d*V* map (constant height) at *V*s = 0.125 V reveals an extended electronic state along the conjugated backbone of oligomer shown in (a). (c) GW calculation of electronic local density of states of the LUMO for a free-standing oligomer chain containing four monomer **11′** subunits (n = 4). Orange overlays in (a)–(c) show the chemical structure of two units of the n = 4 oligomer chain used in the calculation. (d) STM d*I*/d*V* point spectroscopy of oligomer chain shown in (a) reveals an electronic resonance at *V*s ≈ 0.13 V (blue arrow) compared to a reference spectrum on bare Au(111) (spectra are normalized by their respective values at *V*s = 0.6 V, open feedback spectroscopy starting parameters *V*s = 0.6 V, *I* = 0.8 nA, *T* = 4 K).

strong intensity arising from the 3 and 3' positions in the (*E*)-1,1'-bi(indenylidene). When monomer subunits are joined in the n = 4 oligomer chain, GW calculations indicate the formation of an extended electronic state that is lower in energy by 1.0 ± 0.1 eV compared to the monomer LUMO, assuming typical physisorption distances of 0.33 ± 0.03 nm[131] (these values were obtained using an image-charge model of the surface combined with the GW calculation[132]). This state extends continuously along the oligomer backbone as depicted in the theoretical LDOS of Fig. 3.5c. The energetic lowering and spatial extent of the calculated oligomer LDOS closely resembles the experimental data.

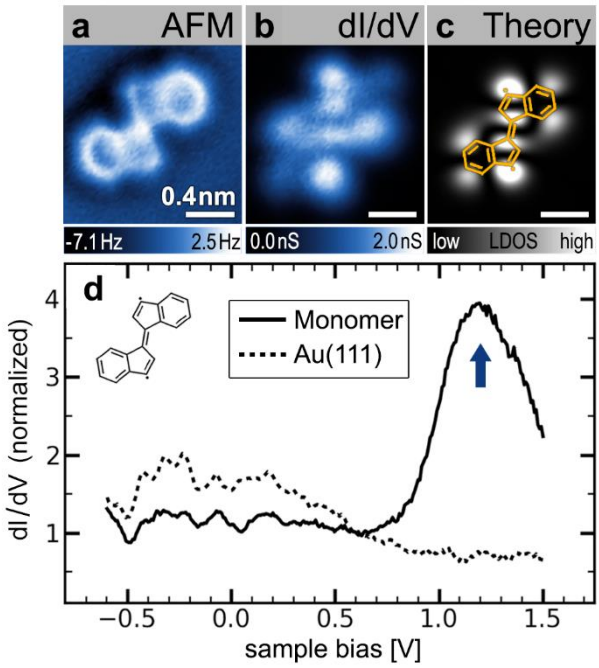

Figure 3.6 Isolated monomer building block **11′**: (a) nc-AFM image of an isolated monomer **11′** on Au(111) (T = 4 K, tip height corresponds to tunnel current set point *V*s = 50 mV and *I* = 35 pA). (b) Experimental constant-height d*I*/d*V* map of monomer **11′** shown in (a) at *V*s = 1.2 V depicts the spatial distribution of the monomer LUMO. (c) GW calculation of the local density of states of the LUMO for a free-standing monomer **11′**. (d) STM d*I*/d*V* point spectroscopy performed on the monomer in shown in (a) reveals the monomer LUMO at *V*s ≈ 1.2 V (blue arrow) compared to a reference spectrum on bare Au(111) (spectra are normalized by their respective values at *V*s = 0.6 V, open feedback spectroscopy starting parameters *V*s = 1.5 V, *I* = 0.5 nA, *T* = 4 K).

The agreement between theory and experiment extends to the appearance of alternating bond lengths in the oligomer. Fig. 3.4c shows that the calculated bond lengths along the conjugated backbone of an n = 4 oligomer chain alternate in the same pattern as observed experimentally for the C–C/C=C bond lengths between indenyl groups (green circles represent long bonds between indenyl groups, red circles represent short bonds between indenyl groups). In the calculation this behavior arises from a combination of Peierls distortion and boundary effects (since the boundary fixes the bond phase). As expected, there is a discrepancy between the nc-AFM experimental results and the theoretical calculations regarding the absolute magnitude of the bond-alternation effect. Whereas the AFM images (Fig. 3.4a) largely exaggerate bond length variations (~50%), the calculation predicts bond-to-bond variations of only ~3%. This discrepancy does not arise from oligomer interaction with the substrate lattice, since similar bond variations are experimentally observed for oligomers lying along different substrate crystallographic directions. The

anomalously large bond alternation observed experimentally is likely an artifact (i.e., an image distortion) caused by tilting of the CO molecule adsorbed to the AFM tip.[95]

In conclusion, we have grown 1D chains of the *oligo*-acetylene derivative *oligo*-(*E*)-1,1'-bi(indenylidene) on a surface through a thermally-induced radical cyclization/step-growth polymerization process. Individual oligomer chains exhibit extended 1D electronic states and alternating bond lengths. This radical polymerization process on surfaces provides a new route toward fully conjugated low-bandgap derivatives of all-*trans poly*-acetylene.

Local Electronic Structure of Oligo Acetylene Derivatives Formed Through Radical Cyclizations at a Surface

Chapter 4

Imaging Single-Molecule Reaction Intermediates Stabilized by Surface Dissipation and Entropy

Chemical transformations at the interface between solid/liquid or solid/gaseous phases of matter lie at the heart of key industrial-scale manufacturing processes. A comprehensive study of the molecular energetics and conformational dynamics underlying these transformations is often limited to ensemble-averaging analytical techniques. Here we report the detailed investigation of a surface-catalyzed cross-coupling and sequential cyclization cascade of 1,2-bis(2-ethynyl phenyl)ethyne on Ag(100). Using non-contact atomic force microscopy (nc-AFM) we imaged the single-bond-resolved chemical structure of transient metastable intermediates. Theoretical simulations indicate that the kinetic stabilization of experimentally observable intermediates is determined not only by the potential energy landscape, but also by selective energy dissipation to the substrate and entropic changes associated with key transformations along the reaction pathway. The microscopic insights gained here pave the way for rational design and control of complex organic reactions at the surface of heterogeneous catalysts.

Parts of this chapter have been published in Riss, A.; Paz, A.P.; Wickenburg, S.; Tsai, H.-Z.; de Oteyza D.G.; Bradley, A.J.; Ugeda, M.M.; Gorman, P**.**; Jung, H.S.; Crommie, M.F.; Rubio, A.; Fischer, F.R. *Nature Chem.*, **2016**, *8*, 678.

4.1 Introduction

Understanding the microscopic mechanisms of surface-catalyzed organic reactions at solid/liquid and solid/gas interfaces is a grand challenge for modern heterogeneous catalysis and its application to industrial-scale chemical processes. Investigation of the underlying reaction mechanisms that transform crude feedstock into complex value-added chemicals at the surface of a heterogeneous catalyst bed is often hampered by competing pathways that lead to numerous intermediates and undesired side-products. Advanced tools such as time-resolved spectroscopy and mass spectrometry provide valuable insight into the product distribution under a variety of reaction conditions. Precise structural identification of transient reaction intermediates and products, however, is limited by their respective concentration in the sample stream, as well as the ability to separate and isolate potentially highly reactive intermediates using chromatographic tools. Crucial transient intermediates that remain adsorbed to the active catalyst during the reaction often escape identification via traditional ensemble-averaging spectroscopic techniques.

Some of these challenges can be overcome by high-resolution scanning probe techniques which have been used to study chemical transformations at the single-molecule level.[69,78–87] Unambiguous identification of complex organic molecules by scanning tunneling microscopy (STM), however, generally still requires support from theoretical calculations.[79,88–91] nc-AFM measurements with functionalized tips,[92,93] on the other hand, allow direct imaging of chemical structure and covalent bonding within organic molecules[94–96] and have even been suggested as a tool to image non-covalent intermolecular contacts.[78,133–136] In recent work,[83] nc-AFM-based chemical identification of reaction products has helped to uncover reaction pathways which were subsequently confirmed by *ab initio* calculations. The temporal resolution for these single-molecule imaging techniques, however, remains more than ten orders of magnitude lower than the typical timescale of a chemical reaction. Real-time observations of chemical reaction steps and their associated microscopic behavior are thus beyond the scope of current nc-AFM measurements.

Here we show that it is possible to directly determine complex surface-reaction mechanisms through real-space imaging of reaction intermediates at the single-molecule/single-bond level. We have successfully stabilized a select series of transient intermediates along a multistep reaction pathway by surface-assisted thermal quenching and entropic effects, and imaged the molecular structures using nc-AFM. This has allowed us to resolve the chemical structure of individual intermediates observed along a reaction pathway involving the bimolecular coupling and intramolecular cyclization cascade of enediyne molecules on a Ag(100) surface. Statistical analysis of large-area scans recorded at sequential time points during the reaction reveals a distinct correlation of the distribution of reactants, intermediates, and products with a postulated reaction mechanism. Theoretical calculations show that the underlying reaction kinetics (and thus the stabilization of particular intermediate species along the reaction coordinate) are strongly influenced by thermal energy dissipation to the underlying metal substrate, as well as by changes in entropy. These new mechanistic insights into complex reaction cascades involving cross-coupling and cyclization reactions should help in future design/optimization of heterogeneous catalytic systems used in industrial manufacturing processes, as well as the development of novel synthetic tools for carbon-based nanotechnology.[80,137–140]

4.2 Experimental Design

The enediyne precursor 1,2-bis(2-ethynyl phenyl)ethyne (**11**) (Fig. 4.1a) was sublimed in ultrahigh vacuum (UHV) onto a Ag(100) surface held at 290 K. Thermal annealing of the adsorbed molecules on Ag(100) induces a series of chemical reactions leading to monomeric, dimeric and oligomeric structures resulting from a sequence of intermolecular cross-coupling and cyclization cascades (see Fig. 4.1).[83,140] To obtain a better understanding of the different reaction pathways observed on the substrate surface, we determined the precise chemical structures of the adsorbates through high-resolution nc-AFM imaging. All cryogenic nc-AFM measurements were performed at 4 K with CO-functionalized tips[92,93] to resolve the structure of the adsorbates before and after subjecting the sample to a series of annealing steps (Fig. 4.1f) over a range of temperatures between 290 K and 460 K.

Herein we will focus on the major reaction pathway resulting from the dimerization of **11** on the surface. Strikingly, the observed dimers (Figs. 4.1b-d) exhibit varying degrees of cyclization (i.e. the number of annulated rings). Uncyclized dimers (i.e. dimers consisting of two uncyclized subunits, e.g. **11-2b**), half-cyclized dimers (i.e. dimers consisting of one cyclized and one uncyclized monomer subunit, e.g. **11-3c**), and fully cyclized dimers (i.e. dimers consisting of two cyclized monomer subunits, e.g. **11-4c**) were found to coexist on the surface. The relative ratio of **11-2b**/**11-3c**/**11-4c** gradually shifts towards molecules featuring higher degrees of cyclization, i.e.

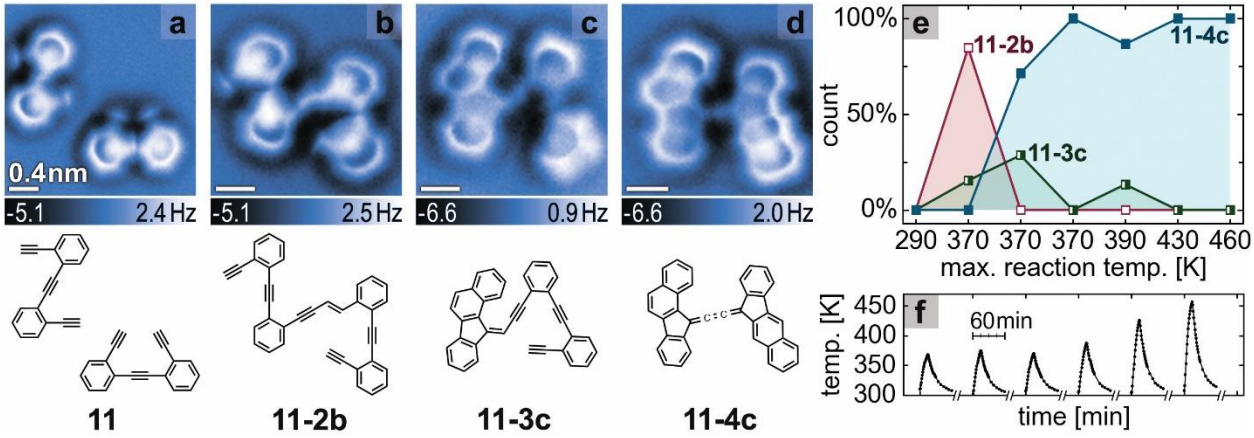

Figure 4.1 Experimental observation of transient intermediates in a stepwise bimolecular enediyne coupling and cyclization cascade. (a–d): Constant-height nc-AFM images show intermediates along the reaction pathway from **11** to **11-4c** (frequency shift ranges are represented by color gradient bars below the images, bright colors correspond to high frequency shift values). The corresponding chemical structures are depicted below the nc-AFM images. (e), Relative abundance of the experimentally observed intermediates (**11-2b**, **11-3c**, **11-4c**) along the reaction pathway after each successive annealing step (data based on 105 counted molecules; the abundance of **11** is excluded since **11** can also undergo other reaction pathways). (f) Measured sample temperature for each successive annealing step.

from uncyclized towards half-cyclized and then to fully cyclized dimers, as temperature is increased with each annealing step (Figs. 4.1e,f). This observation suggests that partially cyclized structures are transient intermediates along a multistep reaction sequence that eventually leads to fully cyclized dimers (such as **11-4c**). The total number of molecules within the reaction pathway does not significantly decrease suggesting that desorption, trapping of intermediates at step edges, or side reactions (such as reaction with hydrogen from the residual gas) do not play an important role.

The single-bond-resolved images of Figs. 4.1a-d provide insight into the mechanistic steps that lead from **11** to the cumulene **11-4c**. During the first annealing step an intermolecular C–C bond is formed between the terminal alkynes of two 1,2-bis(2-ethynyl phenyl)ethynes (**11**) yielding the eneyne intermediate **11-2b** (the building block on the left adopts a C_{2h} symmetry while the right half adopts a C_{2v} symmetry (Fig 4.1b)). A sequence of thermally induced C^1–C^6, and C^1–C^5 cyclizations of the 1,2-bis(2-ethynyl phenyl)ethyne fragment on the left (C_{2h}), followed by a stepwise hydrogen transfer, leads to the benzo[*a*]fluorene **11-3c**. A second thermally activated cyclization/hydrogen transfer sequence converts the remaining 1,2-bis(2-ethynyl phenyl)ethyne fragment on the right into a benzo[*b*]fluorene to yield the fully cyclized product **11-4c**, which features a buta-1,2,3-triene linker.

Intramolecular bonding in the structure of both the partially and fully cyclized intermediates/products can be unambiguously determined despite some distortion of the bond lengths in the nc-AFM images arising from the imaging technique[78,95,140–145] (our structure assignments are consistent with simulated AFM images using the scheme by Hapala et al.[78]). The experimental images provide additional insight into the three-dimensional conformation adopted by the molecules on the surface. For example, the nc-AFM image of **11-3c** shows that one of the phenyl rings (Fig 4.1c, lower right) in the 1,2-bis(2-ethynyl phenyl)ethyne fragment is twisted out of the plane of the surface. Rotation of this ring around the triple bond linking two phenyl-rings points the terminal alkyne group towards the surface (the terminal alkyne is not resolved in the image) while the opposite edge of the phenyl ring is protruding above the plane of the molecule as shown by the brighter contrast in the nc-AFM image.

4.3 Thermodynamic Modeling

Further insight into this reaction sequence is obtained from *ab initio* calculations. We first calculated the reaction energy landscape, i.e. the energies for all transient intermediates along the reaction pathway as well as for the corresponding transition states using density functional-based tight binding (DFTB) theory (Fig. 4.2). The initial activation barrier (i.e. the energy of the first transition state) for the intermolecular coupling of two **11** is 1.38 eV (31.82 kcal mol^{-1})[146] and represents the rate determining step. The energies of all subsequent intermediates (i.e., the local minima along the potential energy landscape, marked by filled circles), as well as all transition states (i.e., the local maxima, marked by empty circles), are lower than the energy of the first transition state. Our calculations suggest the existence of seven intermediate states, whereas only two (**11-2b**, **11-3c**) were experimentally observed. In order to understand why only two of the seven possible intermediates are observed experimentally, we have solved the temperature-

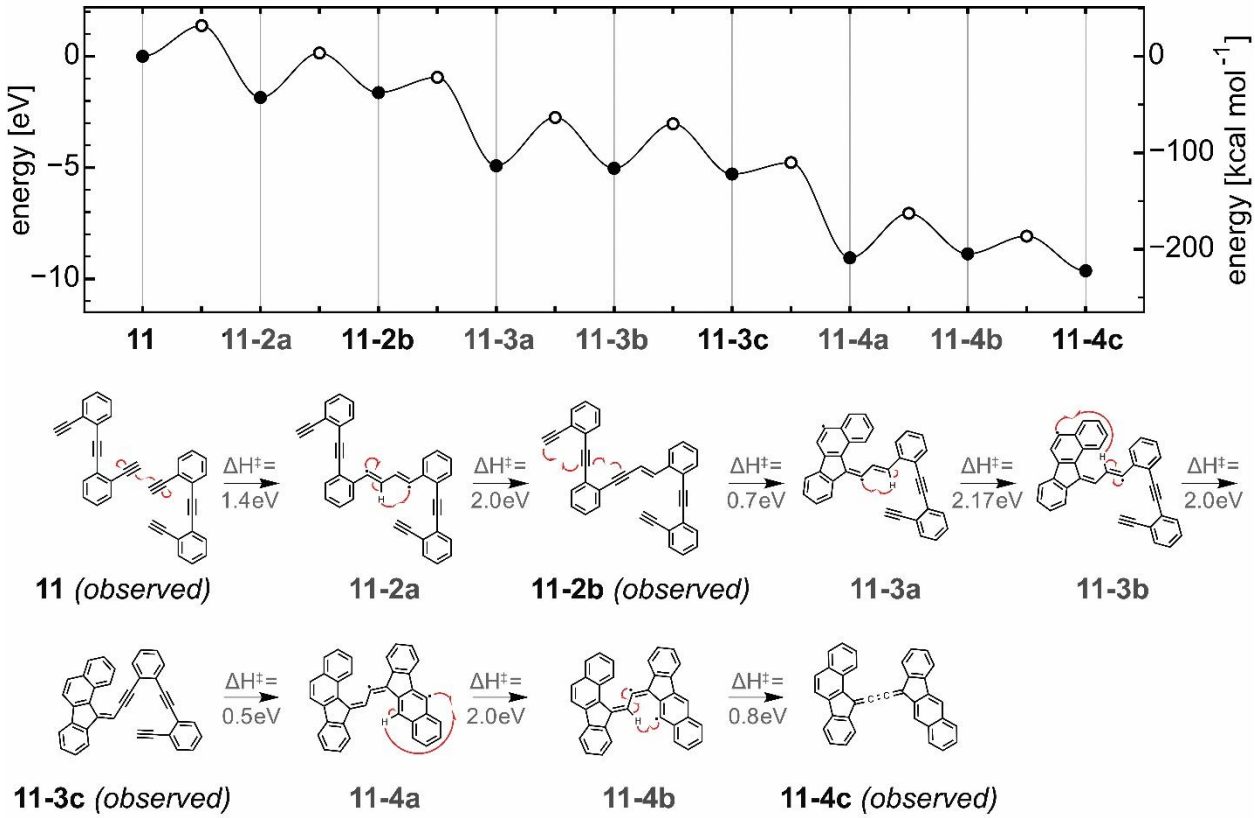

Figure 4.2 Calculated energy diagram for the stepwise enediyne coupling and cyclization cascade. The graph shows the ab initio energy landscape for intermediates and transition state energies along reaction pathway from **11** to **11-4c**. Chemical structures show metastable intermediates along the reaction coordinate (transition state structures not shown). Calculated activation enthalpies are shown below the reaction arrows. Out of seven theoretically predicted intermediates two are experimentally observed – both structures are followed by comparably low activation enthalpy barriers ($\Delta H^{\ddagger}$ = 0.7 eV for **11-2b** and $\Delta H^{\ddagger}$ = 0.5 eV for **11-3c**).

dependent kinetic rate equations for the reaction energy landscape depicted in Fig. 4.2.[147] We find that our data can only be explained by going beyond simple adiabatic and instant thermalization models and by including both selective surface dissipation as well as changes in molecular entropy, as described below.

An adiabatic model of the reaction sequence implies that once the first rate-determining transition state is reached the molecule has sufficient energy to overcome all subsequent reaction barriers Along the path to the final product **11-4c**. The solution of the kinetic rate equations under these conditions (Fig. 4.3a) is determined by only the first reaction barrier. This simple model, however, is incompatible with the experimental observation of metastable intermediates **11-2b** and **11-3c** which are not among the predicted chemical species shown in Fig. 4.3a. A model involving instant thermalization (an approximation commonly used in heterogeneous catalysis[148–151]) also cannot account for the selectivity of our experimental observations. Instant thermalization implies that energy transfer from the molecule to the surface (which acts as a thermal reservoir) is faster than

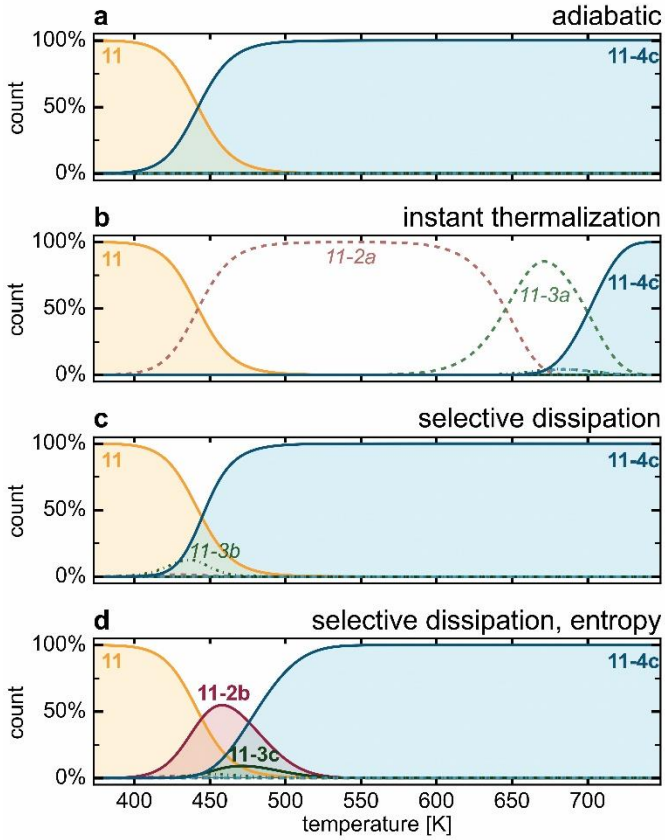

Figure 4.3 Calculated temperature-dependent relative concentrations of reactant, intermediates and product determined by solving kinetic rate equations for the reaction pathway from **11** to **11-4c**. (a) Adiabatic model: only reactant **11** and product **11-4c** are stabilized. (b) Instant thermalization model: only intermediates that are followed by the highest activation barriers are stabilized (**11-2a**, **11-3a**). The product **11-4c** is predicted to be formed only at high temperature. (c) Selective dissipation effects: addition of selective dissipation causes **11-4c** to form at lower temperature and leads to stabilization of **11-3b**. (d) Entropic effects: addition of entropic effects results in predominant stabilization of intermediates **11-2b** and **11-3c**, in agreement with experimental observations.

the subsequent reaction step, thus preferably stabilizing intermediates that are flanked by high activation barriers. However, our *ab initio* calculations (Fig. 4.2) show that the reaction steps following the experimentally observed intermediates feature comparatively low activation barriers ($\Delta H^{\ddagger}$ = 0.7 eV for **11-2b** and $\Delta H^{\ddagger}$ = 0.5 eV for **11-3c**) and so these intermediates are less likely to be stabilized by an instant thermalization model than the intermediates **11-2a** and **11-3a**, which have much higher barriers (but which could not be observed experimentally). This is reflected in the solution of our kinetic rate equations under the assumption of instant thermalization (Fig. 4.3b) which incorrectly predicts stabilization of intermediates **11-2a** and **11-3a**, and which also suggests an unreasonably high formation temperature for product **11-4c**.

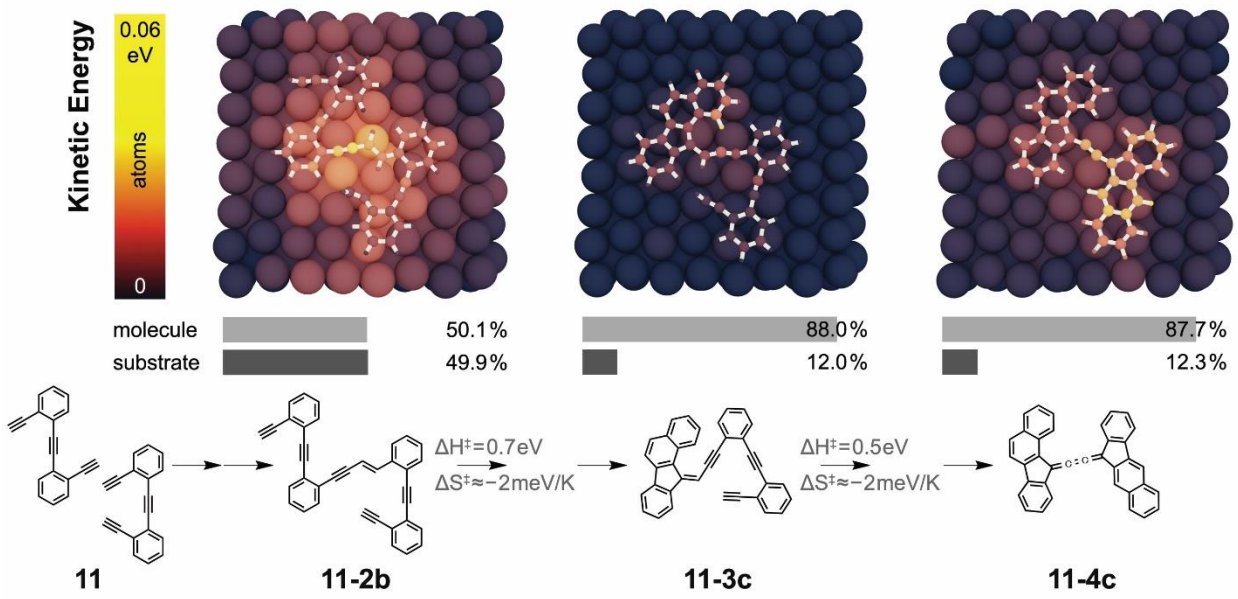

Figure 4.4 Calculated dissipation of the chemical energy at different intermediate reaction steps calculated by DFTB molecular dynamics simulations. The images show spatial maps of the kinetic energy distribution (averaged over 1 ps after the energy plateaus post-reaction) for each atom of the metastable species **11-2b**, **11-3c**, and **11-4c**, as well as the substrate. Relative atom sizes have been adjusted for clarity. Horizontal bars show spatially integrated relative kinetic energy for molecule versus substrate averaged over 1 ps after the energy plateaus post-reaction.

Since neither an adiabatic nor an instant thermalization model can explain the experimentally observed reaction kinetics, we are led to consider the dissipation of chemical energy that is released during each reaction step. We have calculated this dissipative energy transfer by using molecular dynamics (MD) simulations within the DFTB framework that allow us to follow the flow of energy from the reactants to the substrate. Fig. 4.4 shows the resulting atomic kinetic energies (averaged over 1 ps) for the experimentally observed intermediates as well as for the Ag(100) substrate atoms as a function of position (color map). The spatially integrated average kinetic energy for the entire molecule (not including the substrate kinetic energy) and for the entire substrate slab (not including the molecule kinetic energy) are plotted separately beneath each image for a 1 ps period after an energy plateau has been reached (the kinetic energy of the substrate is zero before the reaction). The integrated kinetic energy of the substrate provides a measure for the efficiency of heat transfer from the molecule to the surface, and arises primarily from phonon coupling between the vibrational modes of the molecule and the substrate.

Energy dissipation to the Ag(100) substrate is an efficient process and proceeds at a rate comparable to the chemical transformations along the reaction. The redistribution of energy from the molecule to the substrate effectively reduces the energy available to overcome subsequent activation barriers. Our calculations show that the efficiency of dissipative processes varies greatly for each reaction step (e.g., it is high for the intermediate **11-2b** but relatively low for the intermediate **11-3c**). The effects of selective dissipation are added to our kinetic rate equations

through an effective temperature that depends on how much of the released chemical energy remains in the molecule as kinetic energy after dissipative energy transfer to the substrate (as determined by the MD/DFTB calculations). The conversion factor between the remaining molecular internal (kinetic and potential) energy and the molecular effective temperature increase is the molecular heat capacity:

$$T_{\text{eff}} = T_0 + \Delta E_{\text{molecule}}/C_{\text{V,molecule}} \qquad \text{(Eq. 4.1)}$$

Here T_0 is the substrate temperature before the reaction step, $\Delta E_{\text{molecule}}$ is the internal energy remaining in the molecule after dissipation, and $C_{\text{V,molecule}}$ is the molecular heat capacity. In order to solve our kinetic rate equations in the presence of selective dissipation, we utilize an average value of $C_{\text{V,molecule}} = 80\ k_B$ obtained by considering the different vibrational degrees of freedom of molecules along the reaction pathway. The addition of selective dissipation to our rate equations in this way significantly lowers the expected onset temperature for the formation of the fully cyclized product **11-4c** as seen in Fig. 4.3c, but also suggests a prevalence of the intermediate **11-3b**, which is not observed experimentally. Since the experimentally observed intermediates **11-2b** and **11-3c** are both associated with relatively small activation barriers ($\Delta H^{\ddagger} = 0.7$ eV for **11-2b** and $\Delta H^{\ddagger} = 0.5$ eV for **11-3c**), even the inclusion of selective dissipation is insufficient to explain why they are the only experimentally observed intermediates along the reaction pathway.

To solve this puzzle, we must go one step further and include the effect of changes in entropy on the reaction kinetics.[152–155] Classical transition state theory provides a framework for including such free energy considerations through the Eyring equation:[154]

$$k = \frac{k_B T}{h}\, e^{\frac{\Delta S^{\ddagger}}{k_B}}\, e^{-\frac{\Delta H^{\ddagger}}{k_B T}} \qquad \text{(Eq. 4.2)}$$

where k is the chemical reaction rate constant, k_B is the Boltzmann constant, h is Planck's constant, T is temperature, $\Delta S^{\ddagger}$ is the activation entropy, and $\Delta H^{\ddagger}$ is the activation enthalpy for the reaction step. We implemented this by estimating the activation entropies for the adsorbate intermediates on the Ag(100) substrate within a DFTB framework. This was performed by including vibrational as well as rotational and translational contributions associated with motion of the adsorbates on the surface. The intermediate species **11-2b** and **11-3c** are free to undergo rotational and translational motion, but all other intermediates feature carbon-centered radicals that strongly interact with the surface and thus suppress their roto-translational degrees of freedom.

Using a modified Sackur-Tetrode equation[156–158] and taking into account the degrees of freedom associated with the respective transition states leads to a significant reduction in the activation entropies for the intermediates **11-2b** and **11-3c** up to $\Delta S^{\ddagger} = -2$ meV/K at 573 K (ΔS is not strongly temperature dependent). This large negative activation entropy, which is not present for the other intermediate species, substantially reduces the reaction rates for **11-2b** and **11-3c**. As shown in Fig. 4.3d, inclusion of both selective dissipation and entropic effects in our rate equations explains the experimentally observed selective stabilization of transient intermediates **11-2b** and **11-3c**. The predicted transformation temperatures depicted in Fig. 4.3d, however, are higher than the experimentally observed temperatures (Fig. 4.1e) by about 100 K. This discrepancy is likely caused by a combination of experimental uncertainty in accurately determining the sample surface

temperature (± 25 K at the highest measured temperatures) and theoretical uncertainty in determining the transition state reaction barriers and molecular entropy (typical errors in the estimation of the barriers on the order of 0.1 eV will translate to a change in transformation temperatures of ± 70 K).

4.4 Discussion and Conclusion

A key insight gained in this study is the significance of the fact that the experimentally observed structures **11-2b** and **11-3c** are the only intermediates that do not exhibit carbon-centered radicals (the reactivity of radicals at surfaces can greatly differ from radicals in solution[83,140,159]). Importantly, the transition states for intermediates **11-2b** and **11-3c** exhibit partial radical character and so have restricted roto-translational degrees of freedom, thus contributing further to the large negative activation entropies for these two particular intermediates. These entropic considerations, along with the effects of selective dissipation, are enough to outweigh the considerably larger activation enthalpies of the other intermediates in order to stabilize species **11-2b** and **11-3c** along the pathway from **11** to **11-4c**. In conclusion, we have used single-bond-resolved nc-AFM imaging to characterize the thermally induced dimerization/cyclization reaction cascade of 1,2-bis(2-ethynyl phenyl)ethyne on a Ag(100) surface. By imaging the molecules after sequential annealing steps we have identified the structure and relative abundance of transient intermediates and products along the reaction pathway. *Ab initio* calculations indicate that the observation of particular intermediates along the static energy landscape of the reaction can be explained only by considering both the selective efficiency of energy dissipation to the surface and changes in entropy associated with subsequent reaction steps.

Imaging Single-Molecule Reaction Intermediates Stabilized by Surface Dissipation and Entropy

Chapter 5

Reactivity of Small Molecule Enediynes in Solvated Systems

We have discussed reactivity of enediynes on the single-molecule level, and this chapter seeks to begin building on a motif by which to synthesize one-dimensional materials using the reactivity lessons learned from the previous chapters. In this chapter, synthesis of new small molecule enediynes is discussed. The thermodynamics of Bergman cyclization is considered and evaluated, and polymers are synthesized using Bergman Cyclization Polymerization.

5.1 Introduction

Understanding the microscopic rearrangements of matter on the atomic scale can help us to predict reactivity on the bulk scale. We have discussed reactivity of enediynes on the single-molecule level, yet have neglected the conversation of enediyne reactivity on macroscopic scale. While it is of importance to understand the delicate equilibria that dictate small molecule reactivity on the unimolecular and bimolecular scale, it is of equal importance to understand it on the bulk scale, especially for in the case of industrial production of materials. As we have seen chemical reactivity has important consequences for heterogeneous catalysis,[105,106] and polymer and materials synthesis.[59–69]

Bergman cyclization is a reaction mechanism which lends itself to a great number of advantages over other types of reaction mechanisms typically used for material synthesis. It is relatively mild, requiring no catalyst, it is synthetically flexible allowing for a great degree of functionality within the reaction scheme, and can occur at relatively low temperatures (<35 °C).[160,161] Furthermore, Bergman cyclization is a well-known mechanism, and has received great attention from the biochemical community for its potential role as an anti-cancer agent.[162,163]

The Bergman cyclization is a well-studied system.[164] We have shown via our surface supported studies that enediyne systems have access to a variety of complex reaction mechanisms, and one wonders about the potential for Bergman Cyclization Polymerization (BCP) for use as a polymer generating mechanism using enediynes. Generating homogeneous polymers by BCP have been

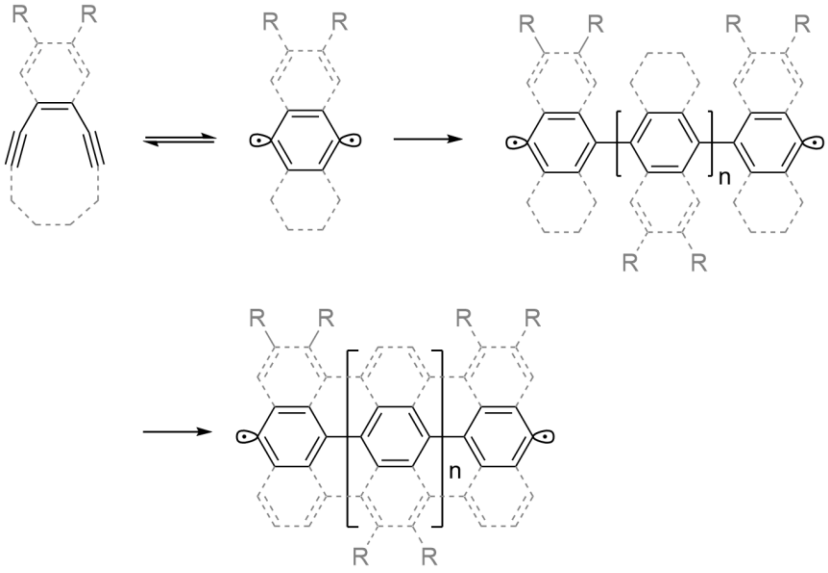

Scheme 5.1 Enediynes, aside from their interesting reaction mechanism, also have potential for use as molecular building blocks for 1-D materials with extended π electron systems. A general reaction scheme is presented above. The essential enediyne core component is highlighted in black. These materials also allow for a great degree of functionality and can be readily adapted (shown in gray dotted outline).

attempted and yet due to the difficulty in characterizing extended arene polymers owing to their relative intractability and insolubility discussion of BCP was effectively tabled.[47,51] However, recent research lend us some clues on how to control to the polymerization process. Kinetic studies may lend us an idea of how to tailor this system.[160,165]

The previous chapters have delved into the reaction mechanism and thermodynamics of enediyne cyclization on surfaces. If we want to understand the mechanism of reaction of these materials in solution, further studies must be done with the hope of expanding our understanding of the reaction mechanism at hand.

5.2 Experimental Design

A series of enediyne molecular precursors with interesting potential as polymer precursors were chosen and synthesized in order to study their reactivity. The selected precursors ultimately could be thought to generate ribbons with interesting electronic potential, as described in Chapter 3. In order to determine the kinetics of cyclization of these precursors so as to better understand the potential for BCP, these molecules were subjected to a variety of kinetic experiments.

Enediynes **15** and **19** were synthesized to evaluate their potential for use in the synthesis of one-dimensional graphitic materials (Scheme 5.2, 5.3). **15** was accessed via 9,10-phenenthrenedione. Double 1,2-addition of TMSA to the phenanthrene dione followed by deprotection yielded diol **16**. Reduction of the diol by anhydrous tin(II) chloride yielded the target enediyne **15**. The synthesis of **19** remained more challenging. The preparation began with ozonolysis of phenenthrene to yield dicarbaldehyde **20**. Corey-Fuchs homologation of the aldehydes yields diyne **21** in

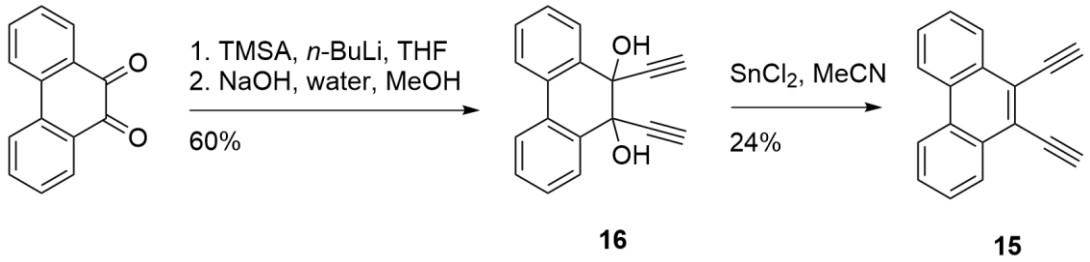

Scheme 5.2 Synthesis of enediyne **15**. Synthesis of this compound was chosen for its synthetic accessibility and its potential for use as a precursor for a graphene nanoribbon with 9-carbon width.

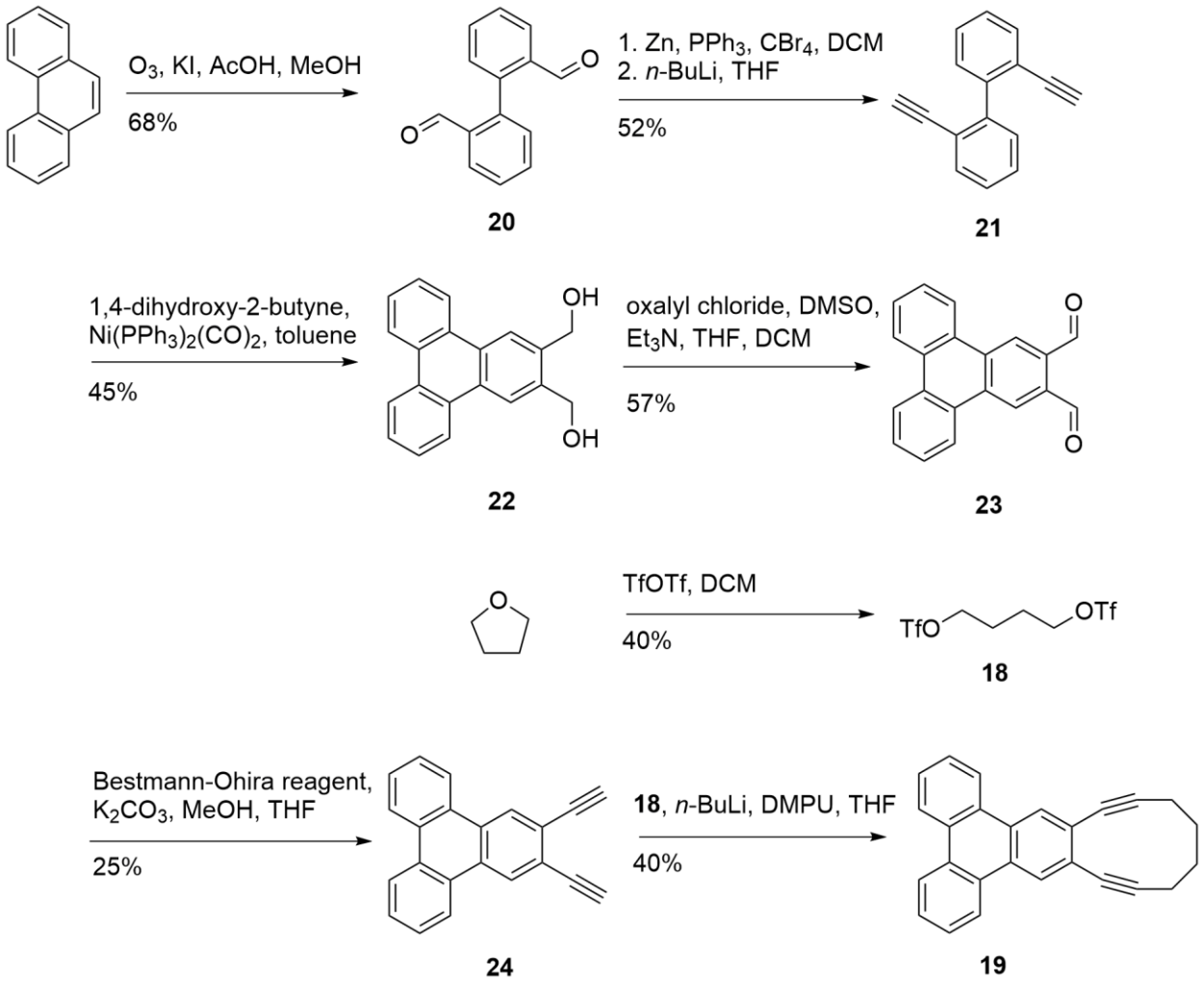

Scheme 5.3 Synthesis of tethered enediyne **19**. Synthesis of this compound was chosen for its potential for use as a precursor for a graphene nanoribbon with 13-carbon width. Additionally, the tether to the terminal alkynes would conceivably lower the activation barrier to C^1–C^6 cyclization while raising the activation barrier to C^1–C^5 cyclization.

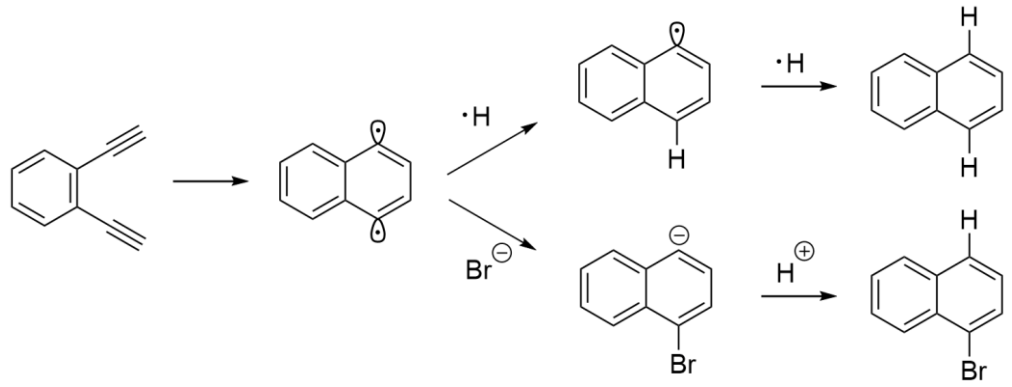

Scheme 5.4 Generic mechanism for C^1–C^6 cyclization of an enediyne and reaction with either HBr or radical hydrogen. While in each case, the starting enediyne forms a di-radical intermediate species, depending on which reagents are present in the reaction mixture, the intermediate may undergo radical addition (top) or nucleophilic addiction (bottom).

moderate, yield. Generation of the triphenylene core remained the greatest challenge of this synthesis. In this instance, the conversion of **21** to the 2,3-disubstituted phenanthrene **22** was achieved by [2+2+2] cycloaddition of 1,4-dihydroxy-2-butyne to the diyne using a Ni(0) catalyst. To obtain moderate yields, a 10-fold excess of butyne was necessary. Swern oxidation of **22** afforded **23** Homologation of **23** via Seyferth-Gilbert homologation afforded **24**. Note that in this instance, it was preferable to subject the *ortho*-substituted dicarbaldehyde to the milder Seyferth-Gilbert homologation than the relatively harsher Corey-Fuchs reaction. Bestmann-Ohira reagent in this case was prepared following a literature procedure.[166] Reaction partner **18** was prepared by ring-opening of THF with trifluoroacetic anhydride. Finally, **24** was tethered with coupling partner **18** to yield tethered enediyne **19**.

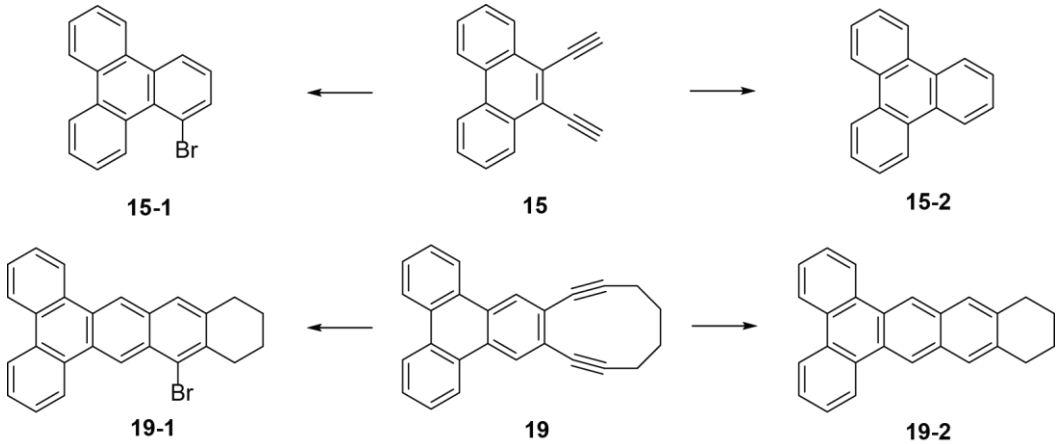

Scheme 5.5 Reaction schemes for the four presented reactions. In the presence of nucleophilcs bromide source like LiBr and acidic proton source like pivalic acid, **15** and **19** should form **15-1** and **19-1** respectively. However, in the presence of a radical hydrogen source like *gamma*-terpinene, **15** and **19** should convert to **15-2** and **19-2** respectively.

Once in hand, they were subjected to conditions outlined by Perrin *et al*.[160] In a typical procedure, the enediyne (4 mM) was added to a solution of lithium bromide (550 mM) in wet DMSO-d6 containing an 1,3,5-trichlorobenzene as internal standard. Because formation of halotriphenylene (Scheme 5.4) produces an equivalent of base, pivalic acid (21.5 mM) was also included. No effort was made to remove water from the solvent. The sample in an NMR tube was degassed by freeze/pump/thaw on a Schlenk line, sealed, and then immersed in a 105 °C oil bath. Disappearance of starting material and formation of product were monitored periodically by removing the sample and analyzing it by NMR.

To evaluate the consistency of these results across multiple reaction types, these enediynes were also subject to radical hydrogen abstraction conditions as well (Scheme 5.4, 5.5). In a typical

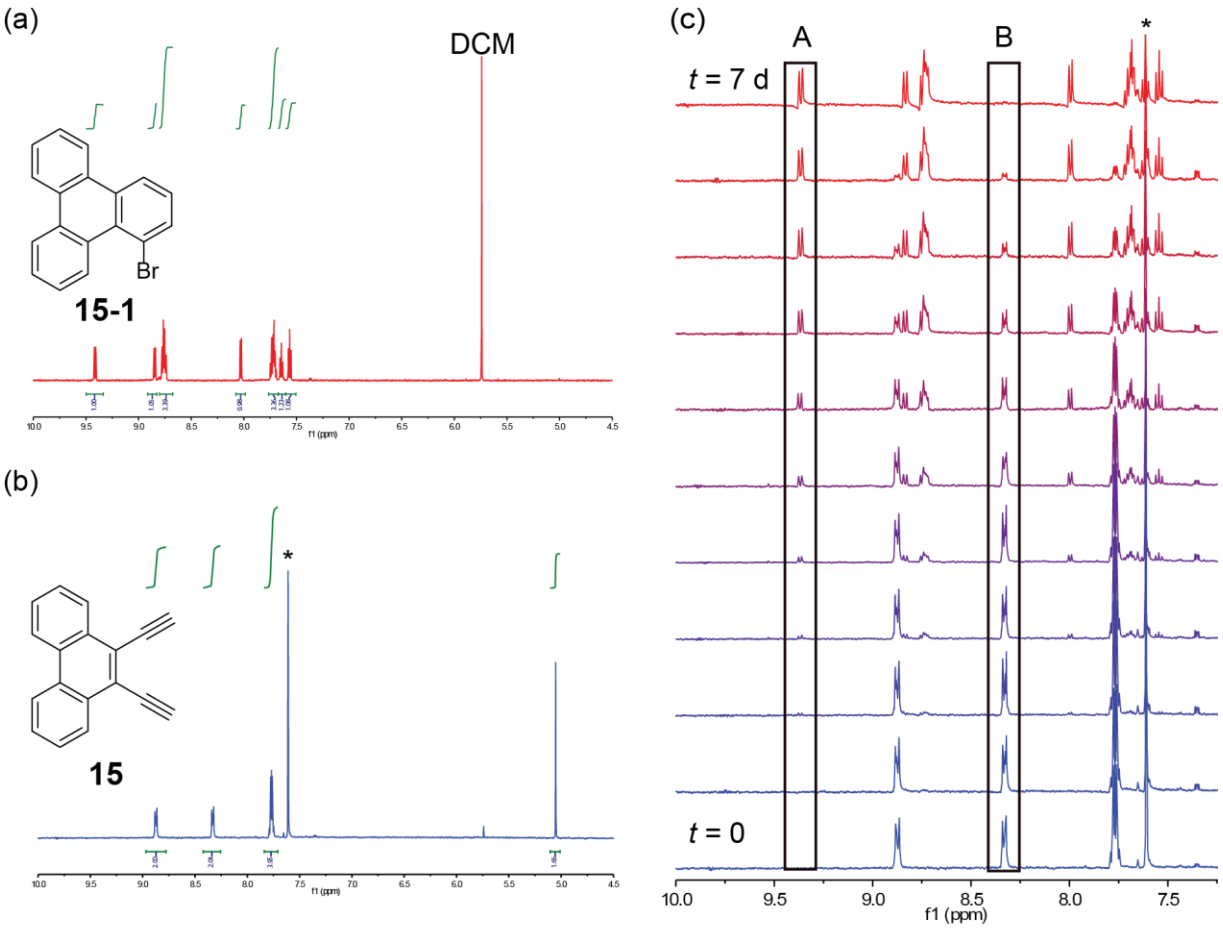

Figure 5.1 Reaction of **15** to form **15-1**. (a) ^{1}H NMR of isolated product **15-1**. Residual DCM is labelled. (b) ^{1}H NMR of **15** at t = 0 of the experiment. 1,3,5-trichlorobenzene is labelled with an asterisk (*). (c) Reaction progress was monitored over the course of 7 days. NMRs were taken at time points t = 0, 0.75, 2.5, 5.3, 8.0, 18, 28, 47, 67, 96, and 160 h. Again, 1,3,5-trichlorobenzene is labelled with an asterisk (*). Reaction progress was evaluated by monitoring the evolution of peaks labelled **A** and **B** (outlined in black).

procedure the enediyne (4 mM) was added to a solution of *gamma*-terpinene (550 mM), as a hydrogen source, in DMSO-d6 containing 1,3,5-trichlorobenzene as internal standard. The terpinene was chosen as the hydrogen source as opposed to the more tradition 1,4-cyclohexadiene as its boiling point is sufficiently above the reaction temperature, while the boiling point of the cyclohexadiene is not. Again, no effort was made to remove water from the solvent. The sample in an NMR tube was degassed by freeze/pump/thaw on a Schlenk line, sealed, and then immersed in a 105 °C oil bath. Disappearance of starting material and formation of product were monitored periodically by removing the sample and analyzing it by NMR.

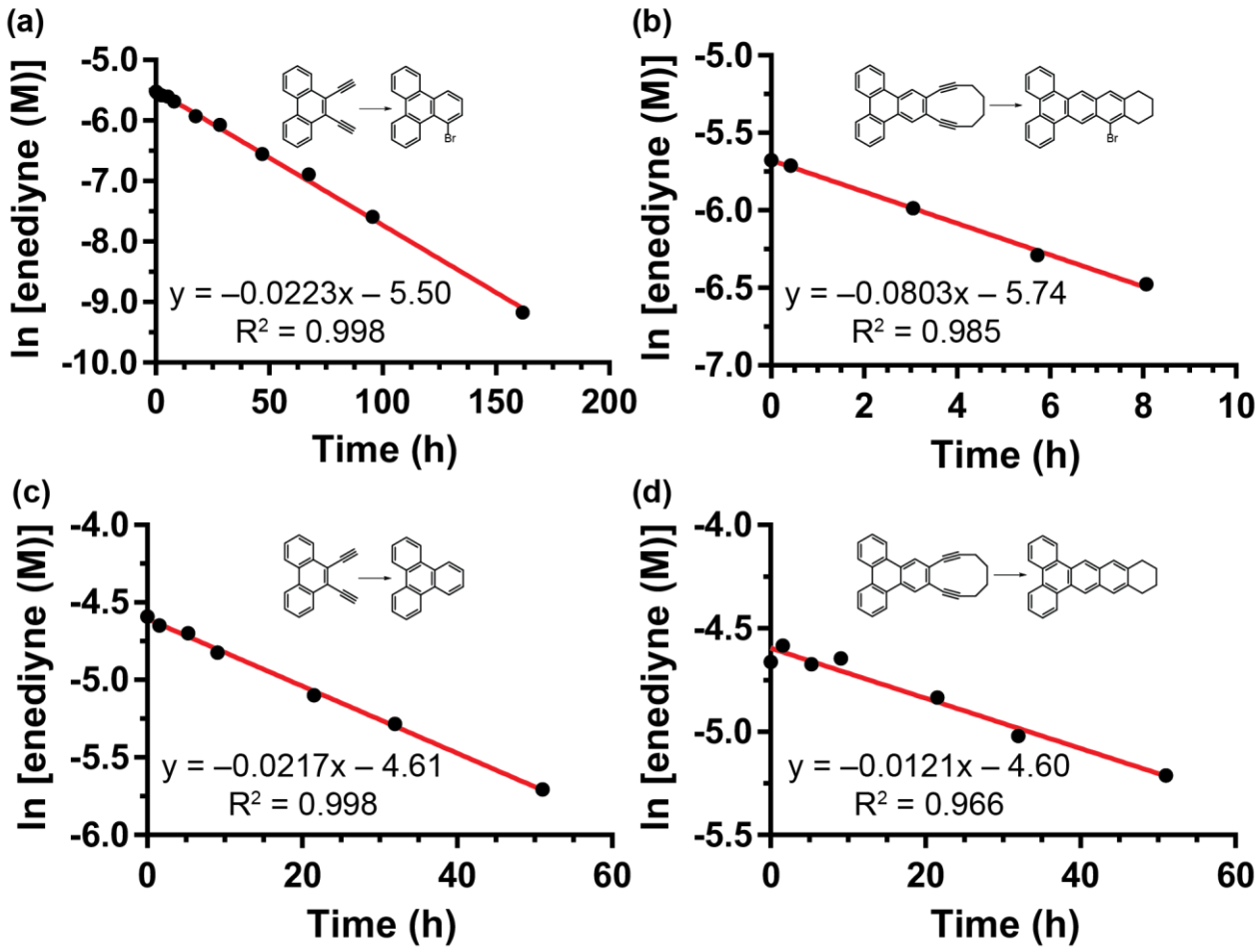

Figure 5.2 Kinetic plots for cyclization reactions. (a) Cyclization of **15→15-1**. (b) Cyclization of **19→19-1**. (c) Cyclization of **15→15-2**. (d) Cyclization of **19→19-2**. Shown below each plot is the linear equation of the linear regression fit to the data along with the R^2 value.

5.3 Cyclization Kinetics

As can be seen by Figure 5.1, the starting material **15** was converted slowly over the course of 7 days into a product. Further investigation of this product by 2D COSY NMR confirms that this material is in fact the bromo-triphenylene product **15-1**.

In order to determine the observed rate constant, 2 peaks were compared to the internal standard 1,3,5-trichlorobenzene. The integrations of peaks A and B (Fig 5.1) verses the internal standard were evaluated as a proxy for concentration of the product and starting materials. The assumed rate constant, k_{obs}, can be evaluated by the following pseudo-first order rate equation:

$$\frac{d[A]}{dt} = k_{obs}[A] \qquad \text{(Eq. 5.1)}$$

where [*A*] represents the concentration of starting enedyine at a given time. We can assume, pseudo-first order conditions as the concentrations of bromide and acid are in great excess to the enedyine. A linear fit to the plot of natural log versus time implies that under these conditions, the reaction is first order in starting material (Figure 5.2). We can also assume that the rate determining step in the cyclization of the starting material to form the cyclic, dehydrobenzene intermediate. At such low concentrations of starting material and such high concentrations of co-reactant materials, we can safely say that polymerization is a non-competitive reaction with the bromide addition.

Diyne	[Diyne] (mmol)	[LiBr] (mmol)	[HA] (mmol)	[terpinene] (mmol)	k_{obs} (10^6 s^1)
15	4.0	550	22	–	6.19
15	4.0	–	–	550	6.01
19	4.0	550	22	–	22.3
19	4.0	–	–	550	3.45

Table 5.1 Rate constants and reaction conditions for the conversion of **15** and **19** into their respective “ring-closed” products.

Table 5.1 shows the outline of the experimental procedures and the calculated rate constants (k_{obs}). Figure 5.2 shows the respective plots. As can be clearly seen, these reactions are all first order in enediyne. As was expected, there is consistency between observed rates of reaction for the untethered enediyne **15** as well as good fit to the data (Fig. 5.2a,c). In addition, as predicted, the rate of cyclization for **19** in increased relative to that of **15** (Fig. 5.2a). We credit this to the presence of the 4-carbon tether linking the terminal alkynes. However, we did not notice the same consistency between the observed rates of reaction for the two cyclizations of **19**. Not only, were the rates inconsistent, but the observed rate of reaction for the reaction of **19→19-2** was significantly lower than the rates of reaction for **15**. This may be an artifact, however, considering the poor regression statistics of the data. A factor leading to this poor data (if in fact poor data is

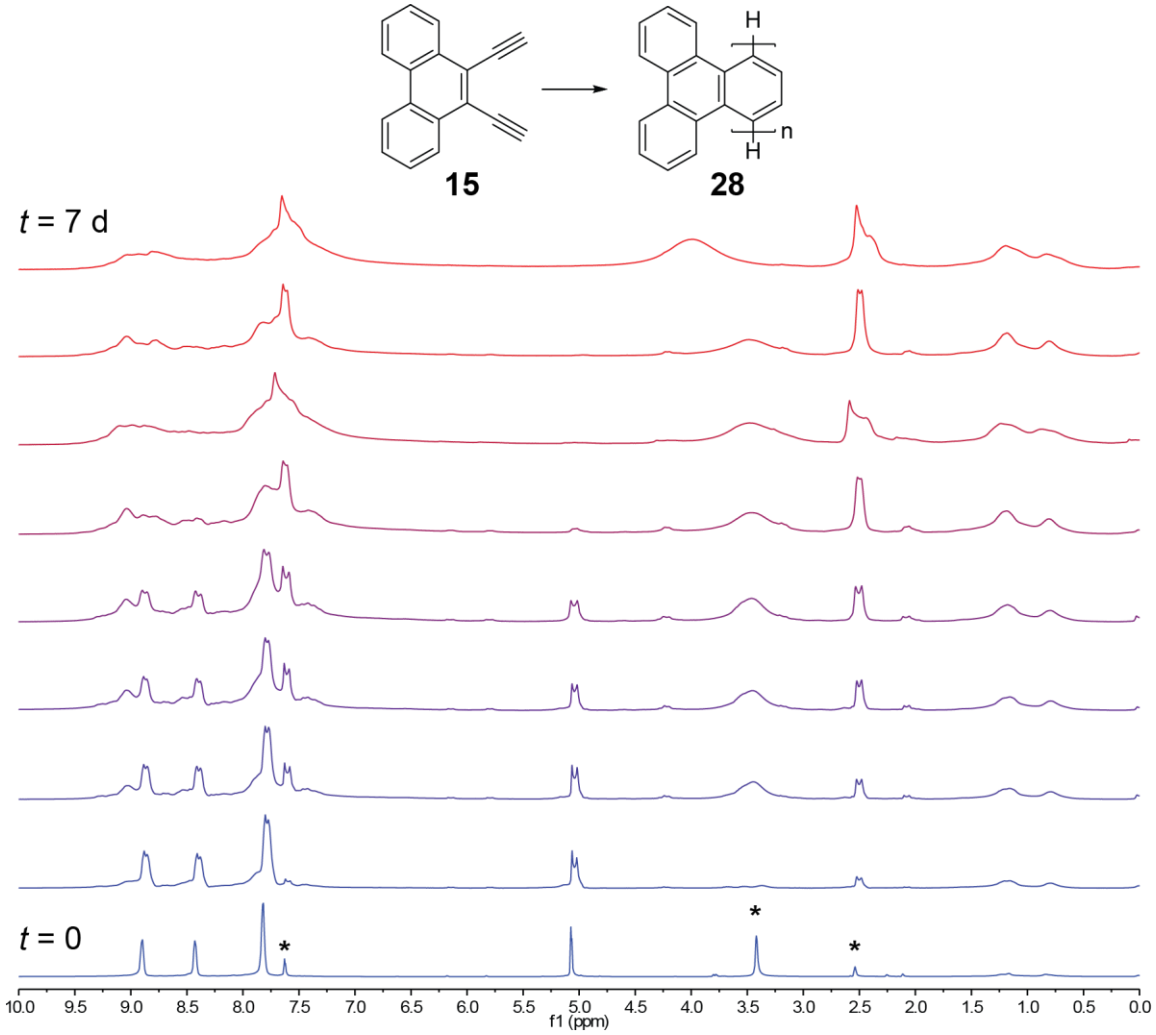

Figure 5.3 Polymerization of **15** to **28** in DMSO-d_6. Residual solvent peaks are labelled with an asterisk (*).

the culprit) may be due to difficulty finding clean signals in the NMR to integrate. The reactions outlined in Figure 5.2a–c all had easily integratable signals (the reference signal was not buried under reactant signals, and there existed starting material signals and product signals that were isolated) whereas there were no easily isolatable signals in the NMR for the reaction outline in Figure 5.2d.

5.4 Polymerization of Enediynes

Aside from determination of the thermodynamic aspect of the cyclization reaction, it is also of interest to create materials using this reaction. Now that we understand that the cyclization of the untethered material occurs at a modest rate at 105 °C we can use this information to inform experimental design parameters for a synthesis that would potentially create polymers (Scheme 5.6).

With **15** in hand, and having recently run similar experiments, a solution based polymerization was attempted. **15** (550 mmol) was dissolved in DMSO and was heated in a 105 °C oil bath for 7 days. Figure 5.3 represents the evolution of the NMR spectrum over those 7 days. The signals on day one are well-resolved. However, after reaction is well-underway, it is evident that there is no-well resolved chemical structure. This lack of resolution can be due to a few effects, perhaps the

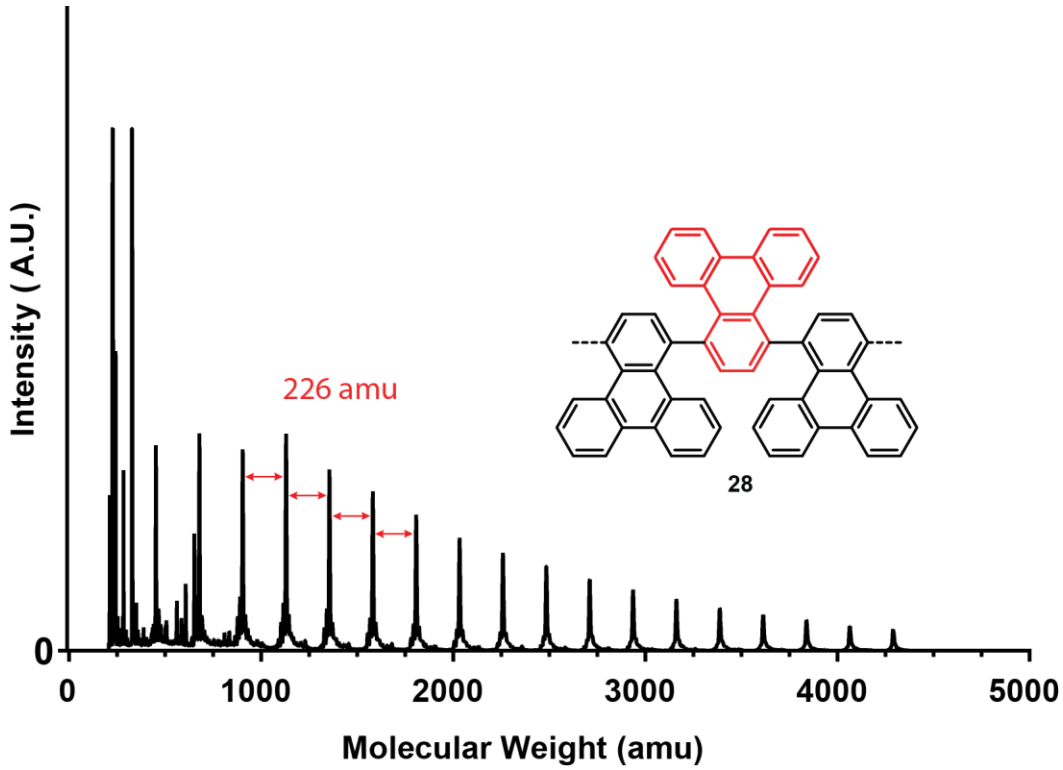

Figure 5.4 MALDI of **28**. The molecular weight of a single monomer is 226 amu which is reflected in the periodicity of 226 amu from peak to peak in the MALDI.

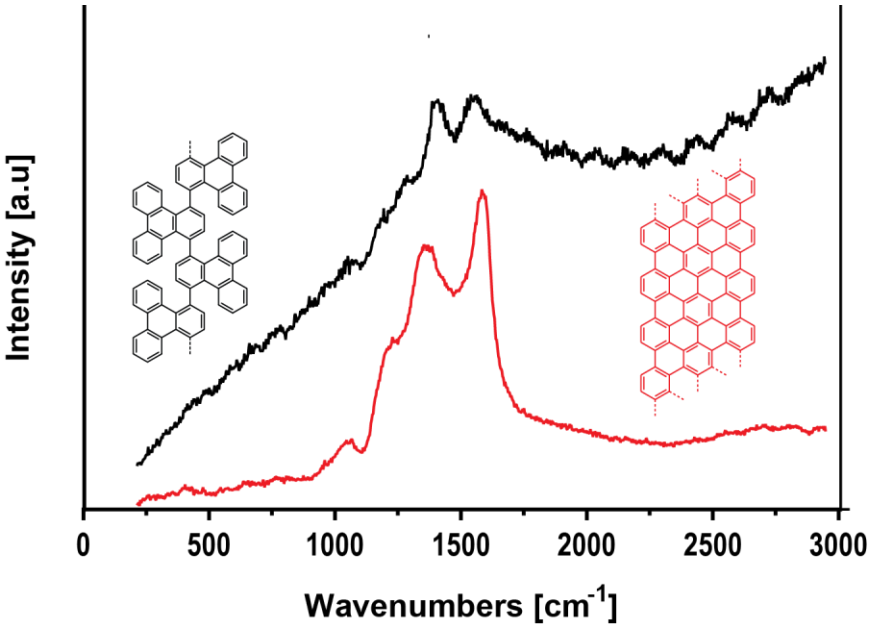

Figure 5.5 Raman spectroscopy of **28** (black) and **29** (red). The two peaks of the GNR **(29)** spectrum are characteristic of a GNRs D and G band.

polymers generated have a great dispersity of length, or perhaps the reaction conditions are still too accessible to deleterious side-reactions.

Considering the high bond dissociation energy (BDE) of Ph-H bonds, it is understandable that the diradicals generated are very reactive and can conceivable react with any hydrogen with a lower BDE. Additionally, as we have seen, the 1,4-dehydrobenzene intermediate is also susceptible to nucleophilic attack. In order to eliminate the possibility for side reaction of the highly reactive diradicals intermediate. Thus it was of great importance that any polymerization attempt contain no impurities and must also contain a high boiling solvent with high BDEs and no nucleophilic tendencies. Thus all polymerization attempts were run in neat triphenylphosphate as solvent. Triphenylphosphate, though a solid at room temperature, it is a liquid at the chosen reaction temperature of 150 °C. In a typical polymerization procedure, 50 mg of **15** were added to a 2 dram glass vial along with 590 mg of triphenylphosphate. The reaction was degassed, sealed, and stirred at 150 °C for 24 h. The black powder isolated was intractable and mostly insoluble, as expected. Thus there were limitations to the characterization available to us.

As we have seen, the Bergman cyclization is not the only reaction mechanism available to enediyne systems. Thus, we must be able to definitively characterize the atomic structure of the final polymer in order to show that polymer **28** consists of a homogenous triphenylene backbone. As Figure 5.4 displays, MALDI of the resultant polymers clearly indicates a regular periodicity of 226 amu, which is the monomer mass, which is a positive sign that the material is undergoing the desired Bergman cyclization polymerization. However, there is still a lack of structural information about the polymer backbone. As we have shown in previous chapters, enediynes have

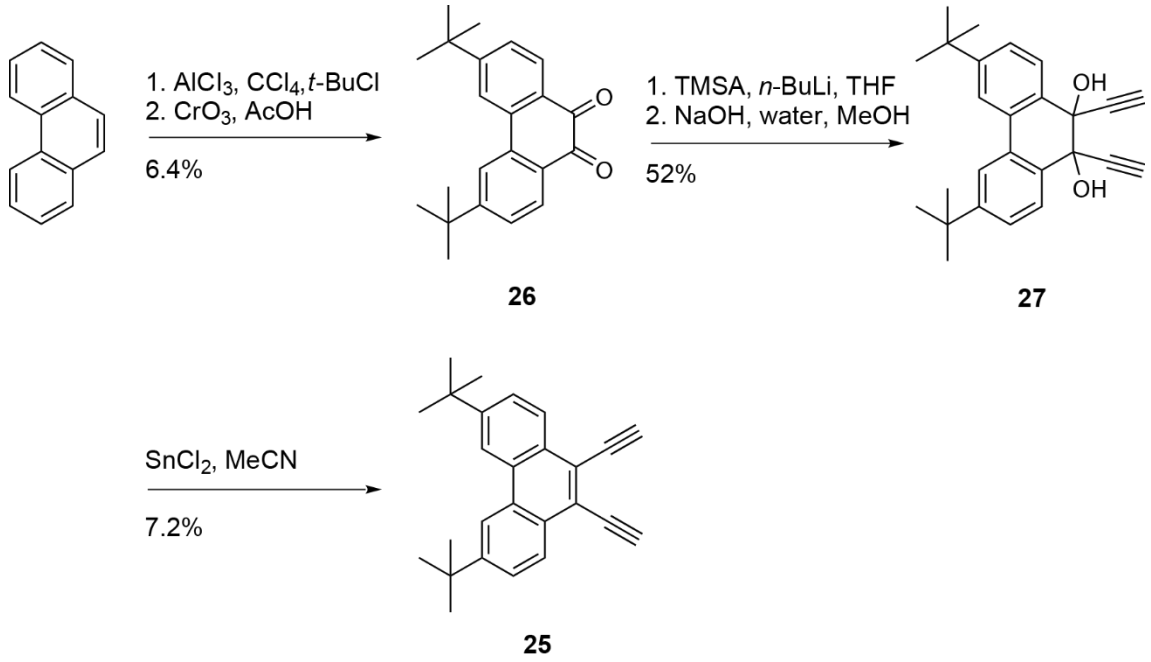

Scheme 5.7 Synthesis of *t*-butylated diyne **25**. This monomer may potentially lead to a soluble polymer.

a variety of reactive mechanisms available like Glaser coupling and C^1–C^5 cyclization to name two. Thus, while the mass is as we expect it to be, we still know very little about the precise structural make-up of the polymer backbone.

To learn more about the polymer structure, we turn to Raman spectroscopy, a common technique used to characterize the structural make-up of materials. Recently, Raman spectroscopy has been used to characterize the structure of GNRs.[167–171] As **28** was designed with the intention to potentially be a GNR precursor, it is simple to convert **28** to a n=9 GNR by typical Scholl oxidation techniques. Therefore, **28** was subjected to Scholl oxidation with ferric chloride to yield product **29**. Figure 5.5 displays the Raman spectra of the polymer before and after oxidation. Promisingly, the spectrum of the post oxidation polymer **29** (Fig. 5.5 red) displays signals characteristic of GNR Raman spectra. The two peaks located at ~1300 and 1600 cm^{-1} are indicative of a GNR's D and G bands.[167,170] Unfortunately, while the peaks are evident, there are still certain characteristics of the spectrum which are unaccounted for, such as the small shoulder at ~1200 cm^{-1} which make it hard to say with certainty that this material is a GNR.

A final attempt to determine if the polymerization technique was in fact producing polymers with the desired structure was to synthesize a material which could potentially be soluble for characterization by bulk ensemble techniques like NMR. It was proposed that **25** could potentially produce ribbons which would then be solubilize by the *tert*-butyl groups on the periphery of the polymer.

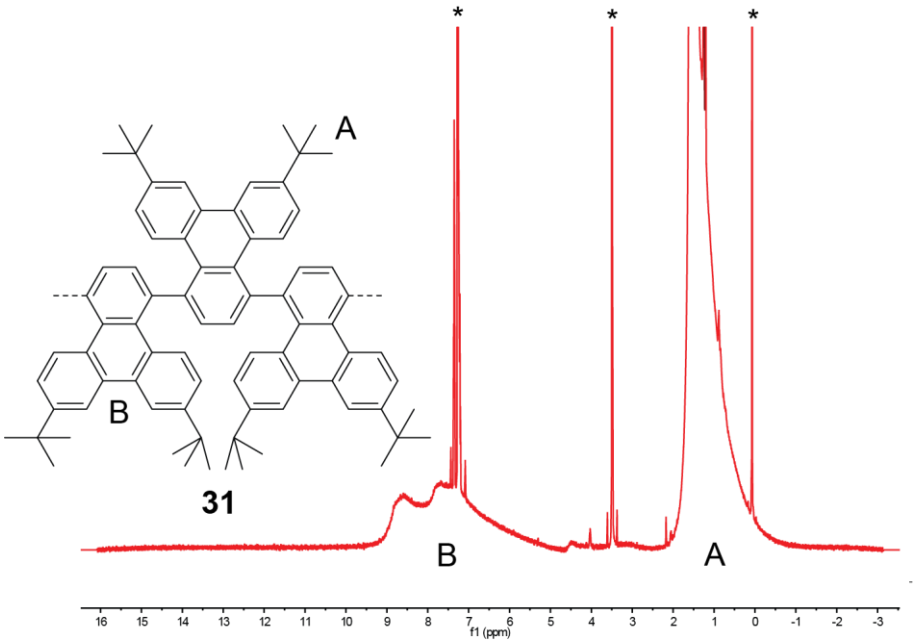

Figure 5.6 NMR of **31**. The two distinguishing characteristics are the large alkyl signal denoted "A" representing the *t*-butyl protons and the bimodal signal "B" which represents the aryl protons. The added solubilizing groups to the polymer backbone do little to resolve the NMR signals. Residual solvent peaks are labelled with an asterisk (*).

To access **25**, phenanthrene was subjected to Friedel-Crafts with *t*-butyl chloride. The statistical mixture of butylated products were directly oxidized with chromium trioxide to dione **26** and then purified. The subsequent reactions are analogous to those used to generate diyne **15**. Dione **26** was alkylated to form diol **27** which was then reduced to form diyne **25** in modest yield.

Diyne **25** was subjected to the same polymerization conditions as the previous precursors. While the solubility of these materials was notably greater than polymers **28** and **30**, characterization by techniques like NMR still fail to resolve the precise structure of the polymer (Figure 5.6). There are 2 sets of signals that we would expect to see from polymer **31**: the signals labelled "A" and "B" in Figure 5.6. The signals labelled "A" represent the total combined integration of all the alkyl signals derived from the *tert*-butyl substituents. That the signal is broad and large relative to the remaining signals makes sense. However, the region of the NMR that we expected greater signal resolution, the aryl region denoted by "B", shows no more resolution than previous NMRs of **28** and **30**.

5.5 Conclusions and Outlook

In conclusion, three small molecule enediyne precursors were synthesized and subjected to a variety of reaction conditions in order to assess the feasibility of use of enediynes as molecular building blocks for 1-D polymeric materials. The kinetics of cyclization for a "tethered" and "untethered" system were compared, and evaluated using two different reaction mechanisms.

Although multiple cyclization routes are available to these enediynes, it was found that C^1–C^6 cyclization occurs exclusively in the presence of excess quenching agent, under both radical and ionic conditions. Polymers were thus synthesized and bulk characterization was attempted. While initial results are promising we still lack discrete structural evidence that the polymer backbone is homogenous.

Moving forward, it will be imperative to determine the structure of a polymer synthesized using Bergman Cyclization Polymerization. Synthesizing polymers with increased solubility seems the most viable route forward and should be investigated. While the typical motif of adding long alkyl chains to the polymer edge seems destined to fail, as it has been shown that alkyl C-H bonds have low enough BDEs to quench the reactive diradicals intermediate, it may be possible to solubilize these materials ionically. Solubility may be achieved, for example if carboxylic acid functionalized precursors are polymerized under basic aqueous conditions.

Chapter 6
Experimental Section

6.1 Materials and General Methods

When unless otherwise stated, all reactions were performed in oven-dried glassware, under an atmosphere of nitrogen. Tetrahydrofuran (THF), triethylamine (Et_3N), toluene, dichloromethane (DCM), and benzene were dried by passing through a column of activated alumina under an atmosphere of nitrogen and were degassed prior to use. All other solvents and reagents were purchased from Alfa Aesar, Spectrum Chemicals, Acros Organics, TCI America, Sigma-Aldrich, and Matrix Scientific and were used as received unless otherwise noted. Thin layer chromatography was performed using SiliCycle silica gel 60 Å F-254 precoated plates (0.25 mm thick) and visualized by UV irradiation or by iodine staining. Flash chromatography was performed on SiliCycle silica gel (particle size 40–63 μm). All ^1H and ^{13}C NMR spectra were recorded on a Bruker AV-600 spectrometer, and are referenced to residual solvent peaks ($CHCl_3$ ^1H NMR; δ = 7.26, ^{13}C NMR; δ = 77.16; DMSO ^1H NMR; δ = 2.50, ^{13}C NMR; δ = 39.52). HR-Mass spectrometry was recorded on a Waters AutoSpec Premier (Waters) spectrometer. Differential scanning calorimetry (DSC) data was collected on a TA Q200 Differential Scanning Calorimeter. Thermogravimetric analysis (TGA) data was collected on a Setaram Sensys TGA-DSC. MALDI mass spectrometry was performed on a Voyager-DE PRO (Applied Biosystems Voyager System 6322) in positive mode using a matrix of dithranol. Raman spectroscopy was recorded using a LabRam ARAMIS automated scanning confocal microscope.

6.1.1 Experimental details of nc-AFM imaging

The Ag(100) surface was prepared by standard sputter-annealing cycles under UHV and cooled to room temperature before depositing the samples from a Knudsen cell held at ~80 °C. The samples were subsequently cooled to cryogenic temperatures for conventional constant-current STM and nc-AFM imaging. For the latter, the apex of the tip was first functionalized with a CO molecule in a qPlus-equipped, commercial Omicron LT-STM/AFM system. CO was deposited on the Ag(100) surface by exposure to 0.06 Langmuir at 5 K. CO was then transferred onto the tip by placing the tip above a molecule and setting the feedback parameters to a sample bias of –1 V and a current of 0.5 nA. Image processing was performed with the WSxM freeware.[172] The product ratios were calculated from 105 molecules characterized by STM on a sample annealed to 145 °C for 1 minute.

Cryogenic imaging was performed at T = 4K in a QPlus-equipped commercial Omicron LT-STM/AFM. nc-AFM images were recorded by measuring the frequency shift of the qPlus resonator (sensor frequency f_0 = 29.73KHz, Q-value of 90000) while scanning over the sample surface in constant height mode. For nc-AFM measurements the apex of the tip was functionalized with a single CO molecule.[92] Oscillation amplitudes of 60 pm were used. All nc-AFM images were recorded at a sample bias of V_s = 50 mV. Differential conductance (dI/dV) was measured in constant-height mode (both for point spectroscopy and for spatial maps) by lock-in detection of the a.c. tunneling current modulated by an 8 mV r.m.s. 300–600 Hz signal added to the tunneling bias.

Alternately, cryogenic nc-AFM measurements (T = 4 K) were performed in a qPlus-equipped[113] commercial Omicron LT-STM/AFM in constant-height mode using CO-functionalized tips[92,93]

(resonance frequency = 29.73 kHz, nominal spring constant = 1800 N/m, Q-value = 90,000, oscillation amplitude = 60 pm, V_S = 0.05 V).

6.1.2 DFT and GW Calculations

Molecular energy levels of the free monomer and free 4-unit oligomer were calculated using the GW approach,[129,130] which includes electron correlation effects not accounted for in density functional theory (DFT) alone. DFT mean-field calculations were performed using the PBE-GGA exchange-correlation functional and norm-conserving pseudopotentials. A plane-wave energy cutoff of 60 Ry was used for the self-consistent determination of the charge density. The calculations were performed using supercells 125 Bohr in length, using optimized structures. The Quantum Espresso package was used for these calculations.

For the GW quasiparticle energies, 4000 empty states were used in the calculation of the dielectric function and the electron self-energy, which was calculated in the generalized plasmon-pole approximation.[129,130] In order to improve the accuracy of the self-energy, a modified static-remainder approach was taken.[173] To account for screening from the metallic substrate, an image charge model[132] was used. An image plane distance of 1.47 Å was used in the image charge model. This image-plane distance is known to be correct for the Au(111) surface.[174] The LUMO levels of the monomer and 4-unit oligomer were calculated as a function of distance between molecule and Au surface. When the surface-molecule distance is set to 3.3 Å (typical physisorption distance of organic molecules on the Au(111) surface[131]), the calculated energy difference between the monomer and oligomer LUMO levels is $\Delta E = E_{\text{LUMO (monomer)}} - E_{\text{LUMO (n=4)}} = 1.00$ eV. When the surface-molecule distance is increased (decreased) by 10%, ΔE changes to 1.10 eV (0.89 eV).

FROM CH 4:

Computational details: All calculations were performed using the density functional-based tight binding (DFTB) method as implemented in the DFTB+ code.[87] Barrier heights along the reaction pathway on the Ag(100) surface were modeled using a periodically repeating 7x7x3 slab fixed at the coordinates derived from the lattice constant of Ag.[175] Transition states were located by constraining the bonds to be broken/formed in a stepwise fashion while relaxing the other adsorbate degrees of freedom and keeping the Ag slab frozen. The energies of the intermediates, as well as the barrier heights of **11-2b** and **11-3c**, were refined by performing structural relaxations of the adsorbates and the upper two Ag layers, and additionally including zero-point energy (ZPE) corrections. The key steps of the reaction (**11→11-2a**, **11-2b→11-3a**, and **11-3c→4a**) do not involve hydrogen transfer, thus we neglect nuclear quantum effects in the calculations. The accuracy of DFTB is discussed in detail in section 7 of the Supplementary Information.

Dissipative energy transfer to the substrate was calculated through constant-energy (no thermostats) molecular dynamics (MD) simulations that allowed us to monitor the time evolution of the kinetic energy of each subsystem (Fig. 4.4). The initial configuration was obtained from the optimization of the upper two Ag layers and the adsorbate (the bottom layer was fixed). A bond constraint was

used to keep the initial adsorbate geometry slightly beyond its transition state and to prevent a chemical reaction during relaxations. The initial ionic velocities were set to zero to facilitate subsequent analysis of the ionic trajectories.

Vibrational entropies and zero point energies were computed by first performing structural relaxations of the adsorbates and the upper two Ag layers (while keeping the bottom one frozen) followed by a partial normal mode analysis of the adsorbate and the top Ag layer vibrations. For "mobile" non-radical species (**11**, **11-2b**, **11-3c**, **11-4c**) we estimated upper bounds for the roto-translational entropies by assuming free 1D rotations about the surface normal and free 2D translations on the surface. Other activation entropies can be neglected since they only involve radical species with constrained roto-translational degrees of freedom.

Kinetic simulations (Fig. 4.3) were performed by numerically solving a system of sequentially-coupled rate equations. The reaction rate constants were determined by the Eyring equation.[154] Selective dissipation was introduced through an effective absolute temperature T_{eff} that replaces T in the Eyring equation. $T_{eff} = T_0 + \Delta T_{molecule}$, where T_0 is the substrate temperature before the respective reaction step and $\Delta T_{molecule}$ is equal to the difference between the released chemical energy and the dissipative energy transfer to the substrate after 1 ps (i.e., the remaining molecular internal energy) divided by the molecular heat capacity, $C_{V,molecule}$. The internal molecular energy is the sum of the molecular kinetic and potential energy (the potential energy is assumed to be equal to the kinetic energy, which is true for harmonic vibrations). $C_{V,molecule}$ was determined by averaging the vibrational heat capacities of the molecules (calculated in the harmonic approximation) for the respective temperature range .

6.2 Synthetic Procedures

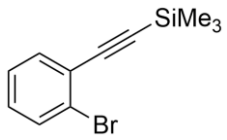

((2-bromophenyl)ethynyl)trimethylsilane (**2**) A 100 mL resealable Schlenk tube was charged under an atmosphere of N_2 with 1-bromo-2-iodobenzene (3.00 g, 10.6 mmol), ethynyltrimethylsilane (1.25 g, 12.7 mmol), tetrakis(triphenylphosphine)palladium(0) (367 mg, 0.32 mmol), and copper(I) iodide (121 mg, 0.64 mmol) in Et_3N (25 mL). The reaction mixture was stirred at 24 °C for 24 h. The reaction mixture was concentrated on a rotary evaporator. The residue was dissolved in ethyl acetate, washed with saturated aqueous $NaHCO_3$ solution, saturated aqueous NaCl solution, dried over $MgSO_4$, and concentrated on a rotary evaporator. Column chromatography (SiO_2; hexane) yielded **2** (2.54 g, 95%) as a yellow oil. ^{1}H NMR (600 MHz, $CDCl_3$): δ = 7.57 (*dd*, *J* = 8.0, 0.9 Hz, 1H), 7.49 (*dd*, *J* = 7.7, 1.6 Hz, 1H), 7.26–7.22 (*m*, 1H), 7.16 (*td*, *J* =7.8, 1.7 Hz, 1H), 0.28 (*s*, 9H) ppm; ^{13}C NMR (151 MHz, $CDCl_3$): δ = 133.6, 132.3, 129.5, 126.8, 125.7, 125.2, 103.0, 99.6, –0.2 ppm; EI-HR-MS: *m/z*: 253.9953 (M^+, $C_{11}H_{13}SiBr^+$, calc. 253.9949).

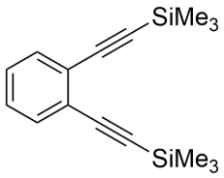

1,2-bis((trimehylsilyl)ethynyl)benzene (**3**) A 100 mL resealable Schlenk tube was charged under an atmosphere of N_2 with 1,2-diiodobenzene (3.50 g, 10.6 mmol), ethynyltrimethylsilane (2.13 g, 21.7 mmol), tetrakis(triphenylphosphine)palladium(0) (367 mg, 0.32 mmol), and copper (I) iodide (121 mg, 0.64 mmol) in Et_3N (25 mL). The reaction mixture was stirred at 24 °C for 20 h. The reaction mixture was concentrated on a rotary evaporator. The residue was dissolved in ethyl acetate, washed with saturated aqueous $NaHCO_3$ solution, saturated aqueous NaCl solution, dried over $MgSO_4$, and concentrated on a rotary evaporator. Column chromatography (SiO_2; hexane) yielded **3** (2.87 g, 99%) as a red oil. ^{1}H NMR (600 MHz, $CDCl_3$): δ = 7.45 (*dd*, *J* = 5.8, 3.4 Hz, 2H), 7.23 (*dd*, *J* = 5.8, 3.3 Hz, 2H), 0.27 (*s*, 18H) ppm; ^{13}C NMR (151 MHz, $CDCl_3$): δ = 132.3, 128.0, 125.7, 103.2, 98.4, 0.0 ppm; EI-HR-MS: *m/z*: 270.1266 (M^+, $C_{16}H_{22}Si_2^+$, calc. 270.1260).

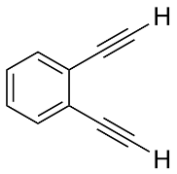

1,2-diethynylbenzene (**4**) A 100 mL roundbottom flask was charged with **3** (2.87 g, 10.6 mmol), and K_2CO_3 (276 mg, 2.0 mmol) in a mixture of THF/MeOH (1:1, 30 mL). The reaction mixture was stirred at 24 °C for 18 h. The reaction mixture was diluted with DCM, washed with 1 N aqueous HCl solution, dried over $MgSO_4$, and concentrated on a rotary evaporator to yield **4** (1.18 g, 88% yield) as a red oil. ^{1}H NMR (600 MHz, $CDCl_3$): δ = 7.52 (*dd*, *J* = 5.7, 3.4 Hz, 2H), 7.32 (*dd*, *J* = 5.8, 3.3 Hz, 2H), 3.34 (*s*, 2H) ppm; ^{13}C NMR (151 MHz, $CDCl_3$): δ = 132.6, 128.5, 125.0, 81.8, 81.1 ppm; EI-HR-MS: *m/z*: 126.0467 (M^+, $C_{10}H_6^+$, calc. 126.0470).

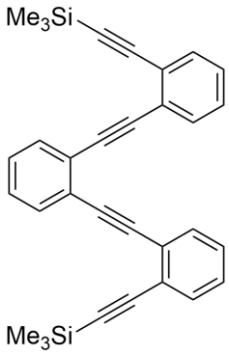

1,2-bis((2-((trimethylsilyl)ethynyl)phenyl)ethynyl)benzene (**5**) A 100 mL resealable Schlenk tube was charged under an atmosphere of N_2 with **4** (817 mg, 6.5 mmol), **2** (3.61 g, 14.2 mmol), tetrakis(triphenylphosphine)palladium(0) (595 mg, 0.52 mmol), copper (I) iodide (96 mg, 0.50 mmol) in Et_3N (40 mL). The reaction mixture was stirred at 70 °C for 22 h. The reaction mixture was concentrated on a rotary evaporator. The residue was dissolved in DCM, washed with saturated aqueous NH_4Cl solution, saturated aqueous NaCl solution, dried over $MgSO_4$, and concentrated on a rotary evaporator. Column chromatography (SiO_2; 100:10:5:0.5 hexane:toluene:DCM:Et_3N) yielded **5** (848 mg, 28%) as a yellow oil. ^{1}H NMR (600 MHz, $CDCl_3$): δ = 7.60 (*dd*, *J* = 5.7, 3.3 Hz, 2H), 7.58–7.55 (*m*, 2H), 7.52–7.50 (*m*, 2H), 7.32 (*dd*, *J* = 5.8, 3.3 Hz, 2H), 7.28–7.24 (*m*, 4H), 0.22 (*s*, 18H); ^{13}C NMR (151 MHz, $CDCl_3$): δ = 132.2, 132.1, 131.9, 128.1, 128.0, 127.9, 126.1, 125.9, 125.5, 103.4, 98.7, 92.3, 92.2, –0.1 ppm; EI-HR-MS: *m/z*: 470.1183 (M^+, $C_{32}H_{30}Si_2^+$, calc. 470.1186).

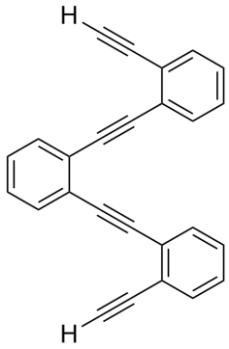

1,2-bis((2-ethynylphenyl)ethynyl)benzene (**1**) A 100 mL roundbottom flask was charged with **5** (985 mg, 2.1 mmol) and K_2CO_3 (58 mg, 0.42 mmol) in a mixture of THF/MeOH (1:1, 10 mL). The reaction mixture was stirred at 24 °C for 18 h. The reaction mixture was diluted with DCM, washed with 1 N aqueous HCl solution, dried over $MgSO_4$, and concentrated on a rotary evaporator. Column chromatography (SiO_2; hexane) yielded **1** (587 mg, 88%) as an orange oil. ^{1}H NMR (600 MHz, $CDCl_3$): δ = 7.62 (*dd*, *J* = 5.8, 3.3 Hz, 2H), 7.60 (*dd*, *J* = 7.5, 1.2 Hz, 2H), 7.54 (*dd*, *J* = 7.5, 1.3 Hz, 2H), 7.36–7.28 (*m*, 6H), 3.24 (*s*, 2H) ppm; ^{13}C NMR (151 MHz, $CDCl_3$): δ = 132.5, 132.4, 132.3, 128.4, 128.1, 128.0, 126.4, 125.5, 124.6, 92.2, 91.8, 82.0, 81.4 ppm; EI-HR-MS: *m/z*: 326.1099 (M^+, $C_{26}H_{14}^+$, calc. 326.1096).

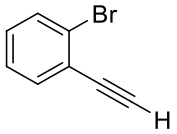

1-bromo-2-ethynylbenzene (**12**) A 100 mL Schlenk tube was charged under an atmosphere of N_2 with **3** (2.54 g, 10.0 mmol) and K_2CO_3 (138 mg, 1.00 mmol) in a mixture of THF/MeOH (1:1, 30 mL). The reaction mixture was stirred at 24 °C for 24 h. The reaction mixture was diluted with DCM, washed with 1 N aqueous HCl, dried over $MgSO_4$, and concentrated on a rotary evaporator to yield **4** (1.61 g, 89%) as a red oil. ^{1}H NMR (600 MHz, $CDCl_3$): δ = 7.59 (*dd*, *J* = 8.1, 0.9 Hz, 1H), 7.53 (*dd*, *J* = 7.7, 1.6 Hz, 1H), 7.31–7.26 (*m*, 1H), 7.21 (*td*, *J* = 7.8, 1.6 Hz, 1H), 3.38 (*s*, 1H) ppm. ^{13}C NMR (151 MHz, $CDCl_3$): δ = 134.1, 132.4, 130.0, 127.0, 125.5, 124.3, 81.9, 81.8 ppm; EI-HR-MS: *m/z*: 181.9550 (M^+, $C_8H_5Br^+$, calc. 181.9554).

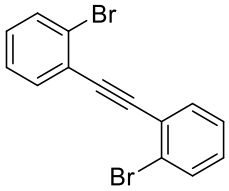

1,2-bis(2-bromophenyl)ethyne (**13**) A dry 100 mL resealable Schlenk tube was charged under an atmosphere of N_2 with **4** (1.61 g, 8.89 mmol), 1-bromo-2-iodobenzene (2.83 g, 10.0 mmol), tetrakis(triphenylphosphine)palladium(0) (549 mg, 0.48 mmol), and copper(I) iodide (190 mg, 1.00 mmol) in Et_3N (30 mL). The reaction mixture was stirred at 24 °C for 24 h. The reaction mixture was then filtered through celite and washed with DCM. The filtrate was collected and washed with concentrated aqueous $NaHCO_3$, concentrated aqueous NaCl, dried over $MgSO_4$, and concentrated on a rotary evaporator. Column chromatography (SiO_2; 20:1 hexane:ethyl acetate) followed by recrystallization from DCM and MeOH yielded **5** (2.24 g, 75%) as a colorless powder. ^{1}H NMR (600 MHz, $CDCl_3$): δ = 7.66–7.59 (*m*, 4H), 7.31 (*td*, *J* = 7.6, 1.1 Hz, 2H), 7.21 (*td*, *J* = 7.9, 1.6 Hz, 2H) ppm; ^{13}C NMR (151 MHz, $CDCl_3$) δ 133.6, 132.5, 129.7, 127.0, 125.5, 125.1, 92.2 ppm; EI-HR-MS: *m/z*: 335.8972 (M^+, $C_{14}H_8Br_2^+$, calc. 335.8972).

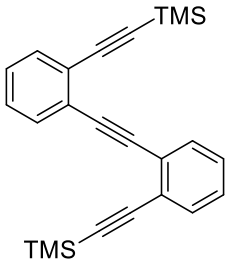

1,2-bis(2-((trimethylsilyl)ethynyl)phenyl)ethyne (**14**) A 100 mL resealable Schlenk tube was charged under an atmosphere of N_2 with **5** (1.55 g, 4.61 mmol), ethynyltrimethylsilane (992 mg, 10.1 mmol), tetrakis(triphenylphosphine)palladium(0) (266 mg, 0.23 mmol), and copper (I) iodide (88 mg, 0.46 mmol), in Et_3N (10 mL). The reaction mixture was stirred at 50 °C for 21 h. The reaction mixture was concentrated on a rotary evaporator, dissolved in ethyl acetate, washed with concentrated aqueous $NaHCO_3$, and concentrated aqueous NaCl, dried over $MgSO_4$, and concentrated on a rotary evaporator. Column chromatography (SiO_2; hexane) yielded **6** (753 mg, 44%) as a yellow oil. ^{1}H NMR (600 MHz, $CDCl_3$): δ = 7.56–7.53 (*m*, 2H), 7.52–7.49 (*m*, 2H), 7.30–7.26 (*m*, 4H), 0.26 (s, 18H) ppm; ^{13}C NMR (151 MHz, $CDCl_3$): δ = 132.2, 131.9, 128.0, 127.9, 126.2, 125.6, 103.4, 98.7, 92.1, 0.0 ppm; EI-HR-MS: *m/z*: 370.1575 (M^+, $C_{24}H_{26}Si_2^+$, calc. 370.1573).

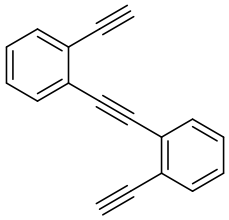

1,2-bis(2-ethynylphenyl)ethyne (**11**) A 100 mL Schlenk tube was charged under an atmosphere of N_2 with **6** (0.753 g, 2.03 mmol) and K_2CO_3 (30 mg, 0.22 mmol) in a mixture of THF/MeOH (1:1, 20 mL). The reaction mixture was stirred at 24 °C for 18 hours. The reaction mixture was diluted in DCM, washed with 1 N aqueous HCl, dried over magnesium sulfate, and concentrated on a rotary evaporator. Column chromatography (SiO_2; 20:1 hexane:DCM) followed by recrystallization from ethyl acetate, and sublimation yielded **1** (155 mg, 34%) as colorless crystals. ^{1}H NMR (600 MHz, $CDCl_3$): δ = 7.59 (*d*, *J* = 7.6 Hz, 2H), 7.54 (*d*, *J* = 7.6 Hz, 2H), 7.34 (*t*, *J* = 7.5 Hz, 2H), 7.32–7.28 (*m*, 2H), 3.35 (*s*, 2H) ppm; ^{13}C NMR (151 MHz, $CDCl_3$): δ = 132.6, 132.3, 128.5, 128.1, 126.2, 124.5, 91.7, 82.1, 81.3 ppm; EI-HR-MS: *m/z*: 226.0784 (M^+, $C_{18}H_{10}^+$, calc. 226.0783).

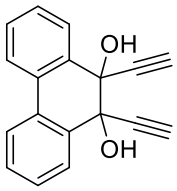

9,10-diethynyl-9,10-dihydrophenanthrene-9,10-diol (**16**) A 1000 mL Schlenk roundbottom flask was charged with ethynyltrimethylsilane (27.9 g, 234 mmol) and THF (300 mL) under an atmosphere of N_2 and cooled to –78 °C for 30 min. To this mixture was added a solution of *n*-butyllithium (100 mL, 2.5 M in hexane) over the course of 1 h and allowed to stir another 1 h at –78 °C. To this mixture was added phenanthrene-9,10-dione (23.5 g, 113 mmol) and the reaction mixture was allowed to stir for 2 h at –78 °C and was then allowed to stir 16 h while warming to 24 °C. The reaction mixture was quenched with aqueous NH_4Cl and the aqueous layer was then extracted with DCM, dried over $MgSO_4$, and concentrated on a rotary evaporator. The resulting brown solid was charged to a 1000 mL roundbottom flask along with methanol (250 mL). A solution of NaOH in water (250 mL, 2 M) was added dropwise at 24 °C over 12 h. The reaction mixture was quenched with NH_4Cl and the precipitate was collected by vacuum filtration. The remaining filtrate was extracted with DCM, dried over $MgSO_4$, and was concentrated on a rotary evaporator. Column chromatography (SiO_2; 20:1 DCM:methanol) yielded **16** (17.7 g, 60%) as a white solid. ^{1}H NMR (600 MHz, $CDCl_3$): δ = 7.90 (d, *J* = 7.6 Hz, 2H), 7.80 (d, *J* = 7.8 Hz, 2H), 7.50–7.45 (m, 2H), 7.45–7.39 (m, 2H), 3.07 (s, 2H), 2.47 (s, 2H); ^{13}C NMR (151 MHz, $CDCl_3$): δ = 131.77, 129.51, 128.72, 124.23, 81.64, 75.39. EI-HR-MS: *m/z*: 260.0840 (M^+, $C_{18}H_{12}O_2^+$, calc. 260.0837).

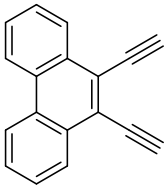

9,10-diethynylphenanthrene (**15**) A 1000 mL Schlenk roundbottom flask equipped with condenser was charged under an atmosphere of N_2 with **16** (14.4 g, 55.3 mmol), anhydrous $SnCl_2$ (31.5 g, 166 mmol), and acetonitrile (500 mL). The reaction mixture was heated to 75 °C and stirred 5 h. The reaction mixture was added to water (400 mL), extracted with DCM (3000 mL), dried over $MgSO_4$, and concentrated on a rotary evaporator. Column chromatography (SiO_2; 20:1 hexane:ethyl acetate) yielded **15** (3.01 g, 24%) as a white solid. ^{1}H NMR (600 MHz, $CDCl_3$): δ = 8.67 (dd, *J* = 8.0, 1.4 Hz, 2H), 8.50 (dd, *J* = 8.0, 1.4 Hz, 2H), 7.75–7.66 (m, 4H), 3.83 (s, 2H); ^{13}C NMR (151 MHz, $CDCl_3$): δ = 130.43, 129.84, 128.06, 127.48, 127.35, 123.59, 122.63, 86.66, 80.79; EI-HR-MS: *m/z*: 226.0786 (M^+, $C_{18}H_{10}^+$, calc. 226.0783).

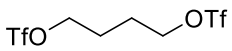

butane-1,4-diyl bis(trifluoromethanesulfonate) (**18**) A 250 mL Schlenk roundbottom flask was charged under an atmosphere of N_2 with trifluoromethanesulfonic anhydride (4.92 g, 17.5 mmol) in DCM (50 mL) and cooled to –78 °C for 10 min. To this mixture was added a solution of THF (1.26 g, 17.5 mmol) in DCM (50 mL) dropwise over 1 h at –78 °C. The mixture was then allowed to warm to 24 °C over the course of 18 h. The reaction mixture was concentrated on a rotary evaporator. The product was then crystallized from DCM to yield **18** (2.50 g, 40% yield) as a as a white solid. ^{1}H NMR (600 MHz, $CDCl_3$): δ = 4.63–4.58 (m, 4H), 2.06–1.98 (m, 4H); ^{13}C NMR (151 MHz, $CDCl_3$): δ = 118.53 (q, $^1J_{FC}$ = 320, 2 C, *C*F3), 75.65, 25.35.

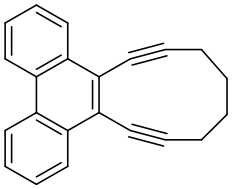

9,10,15,16-tetradehydro-11,12,13,14-tetrahydro-cyclodeca[*l*]phenanthrene (**17**) A 50 mL Schlenk tube was charged under an atmosphere of N_2 with **15** (148 mg, 0.65 mmol) and THF (25 mL) and cooled to 0 °C for 10 min. A solution of *n*-butyl lithium (0.49 mL, 2.5 M) was added to the reaction mixture dropwise and the reaction mixture was allowed to stir 10 min at 0 °C. HMPA (0.34 mL) was added at 0 °C, the reaction was let stir 30 min at 0 °C and then was allowed to warm to 24 °C over for 30 min. A solution of **18** (198 mg, 0.56 mmol) in THF (1 mL) was added to the reaction mixture and allowed to stir 24 h at 24 °C. The reaction mixture was then added to aqueous NH_4Cl, extracted with ethyl acetate, dried over $MgSO_4$, and concentrated on a rotary evaporator. Column chromatography (SiO_2; 100:1 hexane:ethyl acetate) yielded **17** (72.1 mg, 40%) as a white solid. ^{1}H NMR (600 MHz, $CDCl_3$): δ = 8.63 (d, *J* = 7.7 Hz, 2H), 8.33 (d, *J* = 8.1 Hz, 2H), 7.67–7.60 (m, 4H), 2.65–2.61 (m, 4H), 2.12–2.08 (m, 4H); ^{13}C NMR (151 MHz, $CDCl_3$): δ = 130.22, 129.30, 127.61, 127.17, 127.11, 126.99, 122.57, 104.25, 81.97, 28.90, 21.95. EI-HR-MS: *m/z*: 280.1254 (M^+, $C_{22}H_{16}^+$, calc. 280.1252).

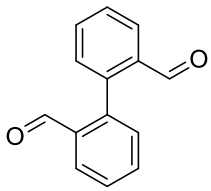

[1,1'-biphenyl]-2,2'-dicarbaldehyde (**20**) A 500 mL roundbottom flask was charged with phenanthrene (10 g, 56.2 mmol) and methanol (300 mL), cooled to –78 °C, and ozone was bubbled through the reaction mixture for 2 h. To the reaction mixture were added potassium iodide (28 g, 167 mmol) and glacial acetic acid (30 mL) at –78 °C and was allowed to stir for 2 h while warming

to 24 °C. The reaction was quenched with aqueous $Na_2S_2O_3$ and the volatile organic solvents were removed under reduce pressure. Water was added and the product was isolated by vacuum filtration to yield **20** (8.06 g, 68%) as a white solid. ^{1}H NMR (600 MHz, $CDCl_3$): δ = 9.84 (s, 2H), 8.07 (dd, *J* = 7.8, 1.4 Hz, 2H), 7.70–7.64 (m, 2H), 7.63–7.58 (m, 2H), 7.36 (dd, *J* = 7.5, 1.2 Hz, 2H); ^{13}C NMR (151 MHz, $CDCl_3$): δ = 191.04, 141.20, 134.54, 133.42, 131.68, 128.81, 128.55. EI-HR-MS: *m/z*: 210.0683 (M^+, $C_{14}H_{10}O_2^+$, calc. 210.0681).

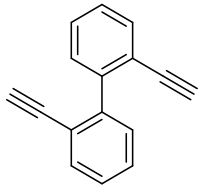

2,2'-diethynyl-1,1'-biphenyl (**21**) A 250 mL roundbottom Schlenk flask was charged under an atmosphere of N_2 with zinc (3.11 g, 47.6 mmol), triphenylphosphine (12.5 g, 47.7 mmol), tetrabromomethane (15.7 g, 47.3 mmol), and DCM (150 mL) and allowed to stir 18 h at 24 °C. The reaction mixture was then cooled to 0 °C and **20** (2.00 g, 9.51 mmol) was added and was allowed to stir 30 min. The reaction mixture was then allowed to warm to 24 °C for 3 h. The reaction mixture was added to hexane (300 mL), the product was collected by vacuum filtration, and concentrated on a rotary evaporator. A 500 mL roundbottom Schlenk flask was charged with the resulting solid and THF (150 mL) and cooled to –78 °C. A solution of *n*-butyl lithium (22.8 mL, 2.5 M in hexane) was added dropwise and the reaction mixture was allowed to stir 18 h while warming to 24 °C. The reaction mixture was quenched with aqueous NH_4Cl, extracted with DCM, dried over $MgSO_4$, and concentrated on a rotary evaporator. Column chromatography (SiO_2; 100:1 hexane:ethyl acetate) yielded **21** (995 mg, 52%) as a yellow solid. ^{1}H NMR (600 MHz, $CDCl_3$): δ = 7.62 (dd, *J* = 7.7, 1.0 Hz, 2H), 7.44–7.31 (m, 6H), 2.96 (dd, *J* = 0.8 Hz, 2H); ^{13}C NMR (151 MHz, $CDCl_3$) δ = 143.23, 133.00, 130.03, 128.22, 127.40, 121.46, 82.56, 80.12. EI-HR-MS: *m/z*: 202.0781 (M^+, $C_{16}H_{10}^+$, calc. 202.0783).

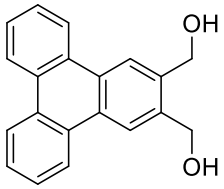

triphenylene-2,3-diyldimethanol (**22**) A 250 mL Schlenk roundbottom flask was charged under atmosphere of N_2 with **21** (2.43 g, 12.0 mmol), 1,4-dihydroxy-2-butyne (10.4 g, 121 mmol), bis(triphenylphosphine)dicarbonylnickel (756 mg, 1.18 mmol), and toluene (50 mL) and heated at reflux for 20 minutes while stirring. The reaction mixture was poured onto water and the resulting solid was collected by vacuum filtration. Column chromatography (SiO_2; 20:1 DCM:methanol)

yielded **22** (1.56 g, 45%) as a white solid. ^{1}H NMR (600 MHz, DMSO-d_6): δ = 8.81 (d, *J* = 8.0 Hz, 2H), 8.79 – 8.74 (m, 4H), 7.76 – 7.67 (m, 4H), 5.36 (t, *J* = 5.6 Hz, 2H), 4.82 (d, *J* = 5.4 Hz, 4H); ^{13}C NMR (151 MHz, DMSO): δ = 139.72, 129.66, 129.48, 128.07, 128.02, 127.71, 124.03, 123.70, 121.82, 61.13. EI-HR-MS: *m/z*: 288.1154 (M^+, $C_{20}H_{16}O_2^+$, calc. 288.1150).

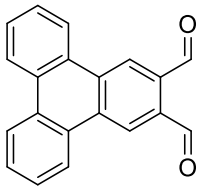

triphenylene-2,3-dicarbaldehyde (**23**) To a 100 mL Schlenk tube was charged under atmosphere of N_2 a solution of oxalyl chloride (4.36 mL, 2 M in hexane) and DCM (100 mL) and was cooled to –78 °C for 10 minutes. To this reaction mixture was added a solution of DMSO (1.55 g, 19.8 mmol) in DCM (5 mL) over 1.5 h at –78 °C and the reaction mixture was allowed to stir another 30 min at this temperature. To this reaction mixture was added a solution of **22** (800 mg, 2.77 mmol) in a mixture of THF (10 mL) and DMSO (1 mL) over 1.5 h at –78 °C and the reaction mixture was allowed to stir another 30 min at this temperature. To the reaction mixture was added Et_3N (5 mL) dropwise are –78 °C. The reaction mixture was allowed to stir at –78 °C for 1 h and then was allowed to warm to 24 °C for 5 h. The reaction mixture was quenched with water, extracted with DCM, dried over $MgSO_4$, and concentrated on a rotary evaporator. Column chromatography (SiO_2; DCM) yielded **23** (449 mg, 57%) as a white solid. ^{1}H NMR (600 MHz, $CDCl_3$): δ = 10.66 (s, 2H), 9.02 (s, 2H), 8.66–8.61 (m, 4H), 7.80–7.70 (m, 4H); ^{13}C NMR (151 MHz, $CDCl_3$) δ 192.17, 133.51, 132.93, 130.89, 129.27, 127.96, 127.76, 124.17, 123.50. EI-HR-MS: *m/z*: 284.0837 (M^+, $C_{20}H_{12}O_2^+$, calc. 284.0837).

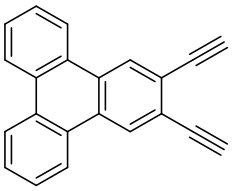

2,3-diethynyltriphenylene (**24**) To a 250 mL Schlenk roundbottom flask under atmosphere of N_2 were charged **23** (1.63 g, 5.74 mmol), K_2CO_3 (4.76 g, 34.4 mmol), methanol (60 mL), and THF (60 mL) and was cooled to 0 °C 30 min. To this reaction mixture was added Bestmann-Ohira reagent (4.41 g, 23.0 mmol) and the reaction mixture was allowed to stir 18 h while warming to 24 °C. The reaction mixture was quenched with aqueous 1N HCl, extracted with DCM, dried over $MgSO_4$, and concentrated on a rotary evaporator. Column chromatography (SiO_2; 10:1 hexane:DCM) yielded **24** (404 mg, 25%) as a white solid. ^{1}H NMR (600 MHz, $CDCl_3$): δ = 8.81 (s, 2H), 8.64 (d, *J* = 7.8 Hz, 2H), 8.59 (d, *J* = 7.8 Hz, 2H), 7.73–7.65 (m, 4H), 3.46 (d, *J* = 2.0 Hz,

2H); ^{13}C NMR (151 MHz, $CDCl_3$): δ = 130.22, 129.61, 128.32, 128.09, 128.07, 127.54, 123.52, 123.33, 122.84, 82.19, 81.20 EI-HR-MS: *m/z*: 276.0944 (M^+, $C_{22}H_{12}^+$, calc. 276.0939).

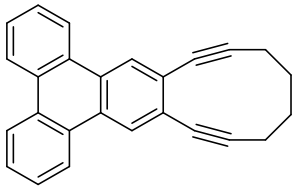

10,11,16,17-tetradehydro-12,13,14,15-tetrahydro-cyclodeca[b]triphenylene (**19**) A 100 mL Schlenk tube was charged with **24** (404 mg, 1.46 mmol) and THF (50 mL) and cooled to 0 °C for 10 min. A solution of *n*-butyl lithium (1.47 mL, 2.5 M) was added to the reaction mixture dropwise and the reaction mixture was allowed to stir 10 min at 0 °C. DMPU (0.62 mL) was added at 0 °C, the reaction was let stir 30 min at 0 °C. A solution of **18** (506 mg, 1.46 mmol) in THF (5 mL) was added to the reaction mixture and allowed to stir 24 h while warming to 24 °C. The reaction mixture was then added to aqueous NH_4Cl, extracted with ethyl acetate, dried over $MgSO_4$, and concentrated on a rotary evaporator. Column chromatography (SiO_2; 20:1 hexane:ethyl acetate) yielded **19** (193 mg, 40%) as a white solid. ^{1}H NMR (600 MHz, $CDCl_3$): δ = 8.66–8.61 (m, 2H), 8.60 (s, 2H), 8.60–8.53 (m, 2H), 7.70–7.62 (m, 4H), 2.58–2.53 (m, 4H), 2.06–2.02 (m, 4H); ^{13}C NMR (151 MHz, $CDCl_3$): δ = 129.98, 129.05, 128.76, 127.77, 127.51, 127.36, 123.37, 123.28, 123.00, 100.58, 82.42, 28.58, 21.62. EI-HR-MS: *m/z*: 330.1407 (M^+, $C_{26}H_{18}^+$, calc. 330.1409).

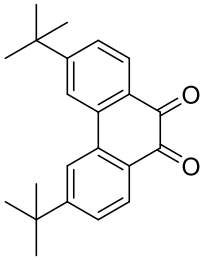

3,6-di-tert-butylphenanthrene-9,10-dione (**26**) To a 500 mL Schlenk rounbottom flask under atmosphere of N_2 was charged phenanthrene (20 g, 112 mmol), anhydrous $AlCl_3$ (800 mg, 6.00 mmol), and CCl_4 (80 mL). To this reaction mixture was added tert-butyl chloride (42 g, 454 mmol) dropwise at 24 °C and the mixture was allowed to stir 30 min. The reaction mixture was then heated to 60°C for 5 h. Water (6 mL) was added to the reaction mixture which was then concentrated on a rotary evaporator. The residue was dissolved in glacial acetic acid (120 mL). A solution of CrO_3 (37.6 g, 376 mmol) in glacial acetic acide (100 mL) was added gradually and the mixture was heated to 110°C, stirred at this temperature for 1 h, °C. The reaction mixture was poured onto cold water, extracted with DCM, dried over $MgSO_4$, and concentrate on a rotary evaporator. Column chromatography (SiO_2; 3:2 DCM:hexane) yielded **26** (2.29 g, 6.4 %) as an orange solid. ^{1}H NMR (600 MHz, DMSO-d_6): δ = 8.18 (d, *J* = 1.8 Hz, 2H), 7.95 (d, *J* = 8.2 Hz,

2H), 7.56 (dd, *J* = 8.2, 1.7 Hz, 2H), 1.39 (s, 18H); ^{13}C NMR (151 MHz, DMSO) δ 179.54, 159.40, 135.67, 129.87, 129.50, 126.91, 121.29, 35.94, 31.05. EI-HR-MS: *m/z*: 320.1776 (M^+, $C_{22}H_{24}O_2^+$, calc. 320.1776).

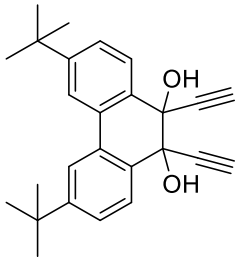

3,6-di-tert-butyl-9,10-diethynyl-9,10-dihydrophenanthrene-9,10-diol (**27**) A 250 mL Schlenk roundbottom flask was charged with ethynyltrimethylsilane (2.10 g, 21.4 mmol) and THF (100 mL) under an atmosphere of N_2 and cooled to –78 °C for 30 min. To this mixture was added a solution of *n*-butyllithium (8.29 mL, 2.5 M in hexane) over the course of 1 h and allowed to stir another 1 h at –78 °C. To this mixture was **26** (2.29 g, 7.15 mmol) and the reaction mixture was allowed to stir for 2 h at –78 °C and was then allowed to stir 16 h while warming to 24 °C. The reaction mixture was quenched with aqueous NH_4Cl and the aqueous layer was then extracted with DCM, dried over $MgSO_4$, and concentrated on a rotary evaporator. The resulting brown residue was charged to a 500 mL roundbottom flask along with methanol (100 mL). A solution of NaOH (100 mL, 2 M) was added dropwise at 24 °C over 12 h. The reaction mixture was quenched with NH_4Cl and the precipitate was collected by vacuum filtration. The remaining filtrate was extracted with DCM, dried over $MgSO_4$, and was concentrated on a rotary evaporator. Column chromatography (SiO_2; 20:1 DCM:methanol) yielded **27** (1.38 g, 52%) as a brown solid. ^{1}H NMR (600 MHz, DMSO-d_6): δ = 7.82 – 7.72 (m, 4H), 7.36 (dd, *J* = 8.1, 1.9 Hz, 2H), 2.96 (s, 2H), 2.07 (s, 2H), 1.35 (s, 18H). EI-HR-MS: *m/z*: 372.2091 (M^+, $C_{26}H_{28}O_2^+$, calc. 372.2089).

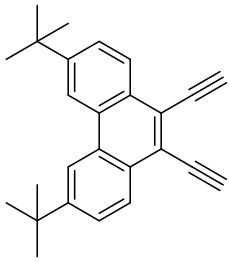

3,6-di-tert-butyl-9,10-diethynylphenanthrene (**25**) A 100 mL Schlenk roundbottom flask equipped with condenser was charged under an atmosphere of N_2 with **27** (1.38 g, 3.71 mmol), anhydrous $SnCl_2$ (2.11 g, 11.1 mmol), and acetonitrile (50 mL). The reaction mixture was heated to 75 °C and stirred 5 h. The reaction mixture was added to water, extracted with DCM, dried over $MgSO_4$, and concentrated on a rotary evaporator. Column chromatography (SiO_2; 20:1 hexane:ethyl acetate) yielded **25** (90 mg, 7.2%) as a brown solid. ^{1}H NMR (600 MHz, DMSO-d_6):

δ = 8.69 (d, *J* = 1.9 Hz, 2H), 8.29 (d, *J* = 8.6 Hz, 2H), 7.86 (dd, *J* = 8.6, 1.8 Hz, 2H), 4.93 (s, 2H), 1.46 (s, 18H); ^{13}C NMR (151 MHz, DMSO): δ = 151.46, 129.37, 128.31, 127.00, 126.60, 122.28, 118.75, 90.50, 80.92, 35.53, 31.49. EI-HR-MS: *m/z*: 338.0239 (M^+, $C_{26}H_{26}^+$, calc. 338.2035).

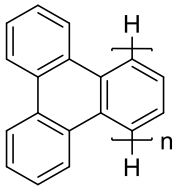

***poly*-triphenylene** (**28**) To a 2 dram vial under atmosphere of N2, were charged **15** (50 mg, 0.21 mmol) and triphenylphosphate (590 mg, 1.81 mmol) and the reaction mixture was heated stirred at 135 °C for 24 h. The reaction was quenched with methanol and the product filtered and rinsed with excess methanol to yield **28** (25 mg, 50%) as a black solid.

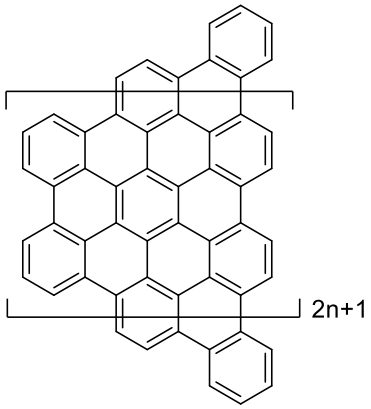

n=9 AGNR (**29**) To a 250 mL Schlenk roundbottom flask under atmosphere of N2 were charged **28** (63.9 mg), ferric chloride (2.061 g, 12.7 mmol), DCM (150 mL) and nitromethane (10 mL). The reaction mixture was stirred for 48 h at 24 °C, then poured into MeOH (100 mL) and filtration yielded **29** (30.0 mg) as a black powder.

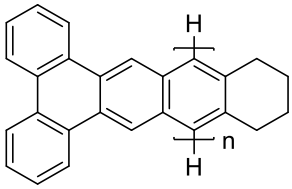

***poly*-11,12,13,14-tetrahydrodibenzo[a,c]tetracene** (**30**) To a 2 dram vial under atmosphere of N2, were charged **19** (50 mg, 0.15 mmol) and triphenylphosphate (590 mg, 1.81 mmol) and the reaction mixture was heated stirred at 135 °C for 24 h. The reaction was quenched with methanol and the product filtered and rinsed with excess methanol to yield **30** (29.5 mg) as a black powder.

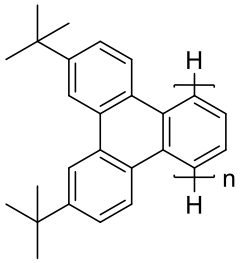

***poly*-2,11-di-tert-butyltriphenylene** (**31**) To a 2 dram vial under atmosphere of N2, were charged **25** (32 mg, 0.094 mmol) and triphenylphosphate (590 mg, 1.81 mmol) and the reaction mixture was stirred at 135 °C for 15 h. The reaction was quenched with isopropanol and the product filtered and rinsed with excess methanol to yield **31** (21.5 mg) as a black powder.

References

(1) Darby, N.; Kim, C. U.; Salaün, J. A.; Shelton, K. W.; Takada, S.; Masamune, S. Concerning the 1,5-didehydro[10]annulene System. *J. Chem. Soc. D* **1971**, *0* (23), 1516–1517.

(2) Bergman, R. G. Reactive 1,4-Dehydroaromatics. *Acc. Chem. Res.* **1973**, *6* (1), 25–31.

(3) Edo, K.; Katamine, S.; Kitame, F.; Ishida, N.; Koide, Y.; Kusano, G.; Nozoe, S. Naphthalenecarboxylic Acid from Neocarzinostatin (NCS). *J. Antibiot. (Tokyo).* **1980**, *33* (3), 347–351.

(4) Lee, M. D.; Dunne, T. S.; Chang, C. C.; Ellestad, G. A.; Siegel, M. M.; Morton, G. O.; McGahren, W. J.; Borders, D. B. Calichemicins, a Novel Family of Antitumor Antibiotics. 2. Chemistry and Structure of Calichemicin .gamma.1I. *J. Am. Chem. Soc.* **1987**, *109* (11), 3466–3468.

(5) Golik, J.; Clardy, J.; Dubay, G.; Groenewold, G.; Kawaguchi, H.; Konishi, M.; Krishnan, B.; Ohkuma, H.; Saitoh, K.; Doyle, T. W. Esperamicins, a Novel Class of Potent Antitumor Antibiotics. 2. Structure of Esperamicin X. *J. Am. Chem. Soc.* **1987**, *109* (11), 3461–3462.

(6) Kraka, E.; Cremer, D. Enediynes, Enyne-Allenes, Their Reactions, and beyond. *Wiley Interdiscip. Rev. Comput. Mol. Sci.* **2014**, *4* (4), 285–324.

(7) Konishi, M.; Ohkuma, H.; Matsumoto, K.; Tsuno, T.; Kamei, H.; Miyaki, T.; Oki, T.; Kawaguchi, H.; VanDuyne, G. D.; Clardy, J. Dynemicin A, a Novel Antibiotic with the Anthraquinone and 1,5-Diyn-3-Ene Subunit. *J. Antibiot. (Tokyo).* **1989**, *42* (9), 1449–1452.

(8) Myers, A. G.; Kuo, E. Y.; Finney, N. S. Thermal Generation of .alpha.,3-Dehydrotoluene from (Z)-1,2,4-Heptatrien-6-Yne. *J. Am. Chem. Soc.* **1989**, *111* (20), 8057–8059.

(9) Myers, A. G.; Dragovich, P. S. Design and Dynamics of a Chemically Triggered Reaction Cascade Leading to Biradical Formation at Subambient Temperature. *J. Am. Chem. Soc.* **1989**, *111* (25), 9130–9132.

(10) Myers, A. G.; Dragovich, P. S.; Kuo, E. Y. Studies on the Thermal Generation and Reactivity of a Class of (.sigma.,.pi.)-1,4-Biradicals. *J. Am. Chem. Soc.* **1992**, *114* (24), 9369–9386.

(11) Nagata, R.; Yamanaka, H.; Murahashi, E.; Saito, I. DNA Cleavage by Acyclic Eneyne-Allene Systems Related to Neocarzinostatin and Esperamicin-Calicheamicin. *Tetrahedron Lett.* **1990**, *31* (20), 2907–2910.

(12) Nagata, R.; Yamanaka, H.; Okazaki, E.; Saito, I. Biradical Formation from Acyclic Conjugated Eneyne-Allene System Related to Neocarzinostatin and Esperamicin-Calichemicin. *Tetrahedron Lett.* **1989**, *30* (37), 4995–4998.

(13) Schmittel, M.; Strittmatter, M.; Kiau, S. Switching from the Myers Reaction to a New Thermal Cyclization Mode in Enyne-Allenes. *Tetrahedron Lett.* **1995**, *36* (28), 4975–4978.

(14) Schmittel, M.; Kiau, S.; Siebert, T.; Strittmatter, M. Steric Effects in Enyne-Allene Thermolyses: Switch from the Myers-Saito Reaction to the C2–C6-Cyclization and DNA Strand Cleavage. *Tetrahedron Lett.* **1996**, *37* (43), 7691–7694.

(15) Schmittel, M.; Keller, M.; Kiau, S.; Strittmatter, M. A Surprising Switch from the Myers–Saito Cyclization to a Novel Biradical Cyclization in Enyne–Allenes: Formal Diels–Alder and Ene Reactions with High Synthetic Potential. *Chem. - A Eur. J.* **1997**, *3* (5), 807–816.

(16) Gabriel Garcia, J.; Ramos, B.; Pratt, L. M.; Rodríguez, A. Intramolecular Cyclization of Enyne [3]cumulenals. *Tetrahedron Lett.* **1995**, *36* (41), 7391–7394.

(17) Prall, M.; Wittkopp, A.; Schreiner, P. R. Can Fulvenes Form from Enediynes? A Systematic High-Level Computational Study on Parent and Benzannelated Enediyne and Enyne−Allene Cyclizations. *J. Phys. Chem. A* **2001**, *105* (40), 9265–9274.

(18) Vavilala, C.; Byrne, N.; Kraml, C. M.; Ho, D. M.; Pascal, R. A. Thermal C^{1} –C^{5} Diradical Cyclization of Enediynes. *J. Am. Chem. Soc.* **2008**, *130* (41), 13549–13551.

(19) Joshi, M. C.; Rawat, D. S. Recent Developments in Enediyne Chemistry. *Chem. Biodivers.* **2012**, *9* (3), 459–498.

(20) Kar, M.; Basak, A. Design, Synthesis, and Biological Activity of Unnatural Enediynes and Related Analogues Equipped with pH-Dependent or Phototriggering Devices. *Chem. Rev.* **2007**, *107*, 2861–2890.

(21) Lindahl, S. E.; Park, H.; Pink, M.; Zaleski, J. M. Utilizing Redox-Mediated Bergman Cyclization toward the Development of Dual-Action Metalloenediyne Therapeutics. *J. Am. Chem. Soc.* **2013**, *135* (10), 3826–3833.

(22) Warner, B. P.; Millar, S. P.; Broene, R. D.; Buchwald, S. L. Controlled Acceleration and Inhibition of Bergman Cyclization by Metal Chlorides. *Buchwald Source Sci. New Ser.* **1995**, *269* (5225), 814–816.

(23) König, B.; Hollnagel, H.; Ahrens, B.; Jones, P. G. Activation of Macrocyclic Biaryl-Enediynes by Metal Ion Coordination. *Angew. Chemie Int. Ed. English* **1995**, *34* (22), 2538–2540.

(24) Kraft, B. J.; Coalter, N. L.; Nath, M.; Clark, A. E.; Siedle, A. R.; Huffman, J. C.; Zaleski, J. M. Photothermally Induced Bergman Cyclization of Metalloenediynes via Near-Infrared Ligand-to-Metal Charge-Transfer Excitation. *Inorg. Chem.* **2003**, *42*, 1663–1672.

(25) Landis, C. A.; Payne, M. M.; Eaton, D. L.; Anthony, J. E. Tellurium-Mediated Cycloaromatization of Acyclic Enediynes under Mild Conditions. *J. Am. Chem. Soc.* **2004**, *126*, 1338–1339.

(26) Sashida, H.; Kurahashi, H.; Tsuchiya, T. 3-Benzotellurepines: The First Examples of Tellurepines. *J. Chem. Soc. Chem. Commun.* **1991**, *0* (12), 802.

(27) O'Connor, J. M.; Lee, L. I.; Gantzel, P.; Rheingold, A. L.; Lam, K.-C. Inhibition and

Acceleration of the Bergman Cycloaromatization Reaction by the Pentamethylcyclopentadienyl Ruthenium Cation. *J. Am. Chem. Soc.* **2000**, *122*, 12057–12058.

(28) O'Connor, J. M.; Friese, S. J.; Tichenor, M. Ruthenium-Mediated Cycloaromatization of Acyclic Enediynes and Dienynes at Ambient Temperature. *J. Am. Chem. Soc.* **2002**, *124*, 3506–3507.

(29) O'Connor, J. M.; Friese, S. J.; Rodgers, B. L. A Transition-Metal-Catalyzed Enediyne Cycloaromatization. *J. Am. Chem. Soc.* **2005**, *127*, 16342–16343.

(30) Alabugin, I. V.; Gilmore, K.; Patil, S.; Manoharan, M.; Kovalenko, S. V.; Clark, R. J.; Ghiviriga, I. Radical Cascade Transformations of Tris(*O* -Aryleneethynylenes) into Substituted Benzo[*a*]indeno[2,1- *c*]Fluorenes. *J. Am. Chem. Soc.* **2008**, *130* (34), 11535–11545.

(31) Giese, B. *Radicals, in Organic Synthesis: Formation of Carbon-Carbon Bonds*; Pergamon: Oxford, U.K., 1986.

(32) Curran, D. P. The Design and Application of Free Radical Chain Reactions in Organic Synthesis, Part 1. *Synthesis (Stuttg).* **1988**, *1988*, 417–439.

(33) Jasperse, C. P.; Curran, D. P.; Fevig, T. L. Radical Reactions in Natural Product Synthesis. *Chem. Rev.* **1991**, *91* (6), 1237–1286.

(34) Hildebrandt, D.; Dyker, G. A Gold-Catalyzed Domino Process to the Steroid Framework. *J. Org. Chem.* **2006**, *71*, 6728–6733.

(35) Iqbal, J.; Bhatia, B.; Nayyar, N. K. Transition Metal-Promoted Free-Radical Reactions in Organic Synthesis: The Formation of Carbon-Carbon Bonds. *Chem. Rev.* **1994**, *94* (2), 519–564.

(36) Snider, B. B. Manganese(III)-Based Oxidative Free-Radical Cyclizations. *Chem. Rev.* **1996**, *96* (1), 339–364.

(37) Gansäuer, A.; Bluhm, H. Reagent-Controlled Transition-Metal-Catalyzed Radical Reactions. *Chem. Rev.* **2000**, *100*, 2771–2788.

(38) Sibi, M. P.; Manyem, S.; Zimmerman, J. Enantioselective Radical Processes†. *Chem. Rev.* **2003**, *103*, 3263–3295.

(39) Matsuda, T.; Kadowaki, S.; Goya, T.; Murakami, M. Synthesis of Silafluorenes by Iridium-Catalyzed [2 + 2 + 2] Cycloaddition of Silicon-Bridged Diynes with Alkynes. *Org. Lett.* **2006**, *9*, 133–136.

(40) Dias, J. R. Steroids Containing Aromatic Hydrocarbon Moieties. *Polycycl. Aromat. Compd.* **1999**, *14* (1–4), 71–76.

(41) Kitagaki, S.; Ohdachi, K.; Kumiko, K.; Mukai, C. Sequential Pericyclic Reaction of Ene-

Diallenes: An Efficient Approach to the Steroid Skeleton. *Org. Lett.* **2005**, *8*, 95–98.

(42) Gourdon, A. Synthesis of "Molecular Landers." *European J. Org. Chem.* **1998**, *1998* (12), 2797–2801.

(43) Zeidan, T. A.; Kovalenko, S. V.; Manoharan, M.; Clark, R. J.; Ghiviriga, I.; Alabugin, I. V. Triplet Acetylenes as Synthetic Equivalents of 1,2-Bicarbenes: Phantom N,π* State Controls Reactivity in Triplet Photocycloaddition. *J. Am. Chem. Soc.* **2005**, *127*, 4270–4285.

(44) Zeidan, T. A.; Clark, R. J.; Ghiviriga, I.; Kovalenko, S. V.; Alabugin, I. V. Triplet Acetylenes as Synthetic Equivalents of 1,2-Bicarbenes, Part II: New Supramolecular Scaffolds from Photochemical Cycloaddition of Diarylacetylenes to 1,4-Cyclohexadienes. *Chem. - A Eur. J.* **2005**, *11* (17), 4953–4960.

(45) Grubbs, R. H.; Kratz, D. Highly Unsaturated Oligomeric Hydrocarbons: α-(Phenylethynyl)-ω-phenylpoly[1,2-phenylene(2,1-Ethynediyl)]. *Chem. Ber.* **1993**, *126* (1), 149–157.

(46) Gleiter, R.; Kratz, D. Conjugated Enediynes—An Old Topic in a Different Light. *Angew. Chemie Int. Ed. English* **1993**, *32* (6), 842–845.

(47) John, J. A.; Tour, J. M. Synthesis of Polyphenylenes and Polynaphthalenes by Thermolysis of Enediynes and Dialkynylbenzenes. *J. Am. Chem. Soc.* **1994**, *116* (11), 5011–5012.

(48) John, J. A.; Tour, J. M. Synthesis of Polyphenylene Derivatives by Thermolysis of Enediynes and Dialkynylaromatic Monomers. *Tetrahedron* **1997**, *53* (45), 15515–15534.

(49) Shah, H. V.; Babb, D. A.; Smith, D. W. Bergman Cyclopolymerization Kinetics of Bis-Ortho-Diynylarenes to Polynaphthalene Networks. A Comparison of Calorimetric Methods. *Polymer (Guildf).* **2000**, *41* (12), 4415–4422.

(50) Chen, X.; Tolbert, L. M.; Hess, D. W.; Henderson, C. A Bergman Cyclization Approach to Polymers for Thin-Film Lithography. *Macromolecules* **2001**, *34*, 4104–4108.

(51) Johnson, J. P.; Bringley, D. A.; Wilson, E. E.; Lewis, K. D.; Beck, L. W.; Matzger, A. J. Comparison of "Polynaphthalenes" Prepared by Two Mechanistically Distinct Routes. *J. Am. Chem. Soc.* **2003**, *125* (48), 14708–14709.

(52) Smith, D. W.; Shah, H. V.; Perera, K. P. U.; Perpall, M. W.; Babb, D. A.; Martin, S. J. Polyarylene Networks via Bergman Cyclopolymerization of Bis-Ortho-Diynyl Arenes. *Adv. Funct. Mater.* **2007**, *17* (8), 1237–1246.

(53) Shirakawa, H.; Louis, E. J.; MacDiarmid, A. G.; Chiang, C. K.; Heeger, A. J. Synthesis of Electrically Conducting Organic Polymers: Halogen Derivatives of Polyacetylene, (CH) X. *J. Chem. Soc. Chem. Commun.* **1977**, No. 16, 578.

(54) Friend, R. H.; Gymer, R. W.; Holmes, A. B.; Burroughes, J. H.; Marks, R. N.; Taliani, C.; Bradley, D. D. C.; Santos, D. A. Dos; Brdas, J. L.; Lgdlund, M.; Salaneck, W. R. Electroluminescence in Conjugated Polymers. *Nature* **1999**, *397* (6715), 121–128.

(55) Coropceanu, V.; Cornil, J.; Filho, D. A. da S.; Olivier, Y.; Silbey, R.; Brédas, J.-L. Charge Transport in Organic Semiconductors. *Chem. Rev.* **2007**, 926–952.

(56) Brabec, C. J.; Sariciftci, N. S.; Hummelen, J. C. Plastic Solar Cells. *Adv. Funct. Mater.* **2001**, *11* (1), 15–26.

(57) *Organic Light Emitting Devices: Synthesis, Properties and Applications*; Müllen, K., Scherf, U., Eds.; Wiley-VCH: Weinheim, 2006.

(58) Zaumseil, J.; Sirringhaus, H. Electron and Ambipolar Transport in Organic Field-Effect Transistors. *Chem. Rev.* **2007**, *107*, 1296–1323.

(59) Barth, J. V.; Costantini, G.; Kern, K. Engineering Atomic and Molecular Nanostructures at Surfaces. *Nature* **2005**, *437* (7059), 671–679.

(60) Bartels, L. Tailoring Molecular Layers at Metal Surfaces. *Nat. Chem.* **2010**, *2*, 87–95.

(61) Elemans, J. A. A. W.; Lei, S.; De Feyter, S. Molecular and Supramolecular Networks on Surfaces: From Two-Dimensional Crystal Engineering to Reactivity. *Angew. Chemie Int. Ed.* **2009**, *48* (40), 7298–7332.

(62) Cai, J.; Ruffieux, P.; Jaafar, R.; Bieri, M.; Braun, T.; Blankenburg, S.; Muoth, M.; Seitsonen, A. P.; Saleh, M.; Feng, X.; Müllen, K.; Fasel, R. Atomically Precise Bottom-Up Fabrication of Graphene Nanoribbons. *Nature* **2010**, *466*, 470–473.

(63) Grill, L.; Dyer, M.; Lafferentz, L.; Persson, M.; Peters, M. V.; Hecht, S. Nano-Architectures by Covalent Assembly of Molecular Building Blocks. *Nat. Nanotechnol.* **2007**, *2* (11), 687–691.

(64) Hla, S.-W.; Bartels, L.; Meyer, G.; Rieder, K.-H. Inducing All Steps of a Chemical Reaction with the Scanning Tunneling Microscope Tip: Towards Single Molecule Engineering. *Phys. Rev. Lett.* **2000**, *85* (13), 2777–2780.

(65) Okawa, Y.; Mandal, S. K.; Hu, C.; Tateyama, Y.; Goedecker, S.; Tsukamoto, S.; Hasegawa, T.; Gimzewski, J. K.; Aono, M. Chemical Wiring and Soldering toward All-Molecule Electronic Circuitry. *J. Am. Chem. Soc.* **2011**, *133* (21), 8227–8233.

(66) Okawa, Y.; Aono, M. Materials Science: Nanoscale Control of Chain Polymerization. *Nature* **2001**, *409* (6821), 683–684.

(67) Zwaneveld, N. A. A.; Pawlak, R.; Abel, M.; Catalin, D.; Gigmes, D.; Bertin, D.; Porte, L. Organized Formation of 2D Extended Covalent Organic Frameworks at Surfaces. *J. Am. Chem. Soc.* **2008**, *130* (21), 6678–6679.

(68) Treier, M.; Richardson, N. V.; Fasel, R. Fabrication of Surface-Supported Low-Dimensional Polyimide Networks. *J. Am. Chem. Soc.* **2008**, *130* (43), 14054–14055.

(69) Zhang, Y.-Q.; Kepčija, N.; Kleinschrodt, M.; Diller, K.; Fischer, S.; Papageorgiou, A. C.; Allegretti, F.; Björk, J.; Klyatskaya, S.; Klappenberger, F.; Ruben, M.; Barth, J. V. Homo-

Coupling of Terminal Alkynes on a Noble Metal Surface. *Nat. Commun.* **2012**, *3*, 1286.

(70) Facchetti, A. π-Conjugated Polymers for Organic Electronics and Photovoltaic Cell Applications. *Chem. Mater.* **2011**, *23* (3), 733–758.

(71) Novoselov, K. S.; Geim, A. K.; Morozov, S. V.; Jiang, D.; Zhang, Y.; Dubonos, S. V.; Grigorieva, I. V.; Firsov, A. A. Electric Field Effect in Atomically Thin Carbon Films. *Science (80-.).* **2004**, *306* (5696).

(72) Geim, A. K.; Novoselov, K. S. The Rise of Graphene. *Nat. Mater.* **2007**, *6* (3), 183–191.

(73) Geim, A. K. Graphene: Status and Prospects. *Science (80-.).* **2009**, *324* (5934).

(74) Barone, V.; Hod, O.; Scuseria, G. E. Electronic Structure and Stability of Semiconducting Graphene Nanoribbons. *Nano Lett.* **2006**, *6*, 2748–2754.

(75) Yang, L.; Park, C.-H.; Son, Y.-W.; Cohen, M. L.; Louie, S. G. Quasiparticle Energies and Band Gaps in Graphene Nanoribbons. *Phys. Rev. Lett.* **2007**, *99* (18), 186801.

(76) Xiao, Y.; Hu, A. Bergman Cyclization in Polymer Chemistry and Material Science. *Macromol. Rapid Commun.* **2011**, *32* (21), 1688–1698.

(77) Skoog, D. A.; Holler, F. J.; Crouch, S. R. *Principles of Instrumental Analysis*, 6th ed.; Brooks/Cole: Belmont, CA, 2006.

(78) Hapala, P.; Kichin, G.; Wagner, C.; Tautz, F. S.; Temirov, R.; Jelínek, P. Mechanism of High-Resolution STM/AFM Imaging with Functionalized Tips. *Phys. Rev. B* **2014**, *90* (8), 85421.

(79) Björk, J.; Zhang, Y. Q.; Klappenberger, F.; Barth, J. V.; Stafström, S. Unraveling the Mechanism of the Covalent Coupling between Terminal Alkynes on a Noble Metal. *J. Phys. Chem. C* **2014**, *118* (6), 3181–3187.

(80) Gao, H.-Y.; Wagner, H.; Zhong, D.; Franke, J.-H.; Studer, A.; Fuchs, H. Glaser Coupling at Metal Surfaces. *Angew. Chemie Int. Ed.* **2013**, *52* (14), 4024–4028.

(81) Gao, H. Y.; Franke, J. H.; Wagner, H.; Zhong, D.; Held, P. A.; Studer, A.; Fuchs, H. Effect of Metal Surfaces in on-Surface Glaser Coupling. *J. Phys. Chem. C* **2013**, *117* (36), 18595–18602.

(82) Liu, J.; Chen, Q.; Xiao, L.; Shang, J.; Zhou, X.; Zhang, Y.; Wang, Y.; Shao, X.; Li, J.; Chen, W.; Xu, G. Q.; Tang, H.; Zhao, D.; Wu, K. Lattice-Directed Formation of Covalent and Organometallic Molecular Wires by Terminal Alkynes on Ag Surfaces. *ACS Nano* **2015**, *9* (6), 6305–6314.

(83) de Oteyza, D. G.; Gorman, P.; Chen, Y.-C.; Wickenburg, S.; Riss, A.; Mowbray, D. J.; Etkin, G.; Pedramrazi, Z.; Tsai, H.-Z.; Rubio, A.; Crommie, M. F.; Fischer, F. R. Direct Imaging of Covalent Bond Structure in Single-Molecule Chemical Reactions. *Science (80-.).* **2013**, *340* (6139), 1434–1437.

(84) Cioslowski, J.; Liu, G.; Moncrieff, D. Nonclassical Aryl Radicals: Intermediates or Transition States for the Hydrogen Shift Reactions? *J. Org. Chem.* **1996**, *61* (12), 4111–4114.

(85) Brooks, M. A.; Scott, L. T. 1,2-Shifts of Hydrogen Atoms in Aryl Radicals. *J. Am. Chem. Soc.* **1999**, *121* (23), 5444–5449.

(86) Tuckerman, M. E.; Marx, D. Heavy-Atom Skeleton Quantization and Proton Tunneling In "intermediate-Barrier" hydrogen Bonds. *Phys. Rev. Lett.* **2001**, *86* (21), 4946–4949.

(87) Aradi, B.; Hourahine, B.; Frauenheim, T. DFTB+, A Sparse Matrix-Based Implementation of the DFTB Method. In *Journal of Physical Chemistry A* **2007**, *111*, 5678–5684.

(88) Di Giovannantonio, M.; El Garah, M.; Lipton-Duffin, J.; Meunier, V.; Cardenas, L.; Fagot Revurat, Y.; Cossaro, A.; Verdini, A.; Perepichka, D. F.; Rosei, F.; Contini, G. Insight into Organometallic Intermediate and Its Evolution to Covalent Bonding in Surface-Confined Ullmann Polymerization. *ACS Nano* **2013**, *7* (9), 8190–8198.

(89) Zhou, H.; Liu, J.; Du, S.; Zhang, L.; Li, G.; Zhang, Y.; Tang, B. Z.; Gao, H. J. Direct Visualization of Surface-Assisted Two-Dimensional Diyne Polycyclotrimerization. *J. Am. Chem. Soc.* **2014**, *136* (15), 5567–5570.

(90) Sun, Q.; Zhang, C.; Li, Z.; Kong, H.; Tan, Q.; Hu, A.; Xu, W. On-Surface Formation of One-Dimensional Polyphenylene through Bergman Cyclization. *J. Am. Chem. Soc.* **2013**, *135* (23), 8448–8451.

(91) Treier, M.; Pignedoli, C. A.; Laino, T.; Rieger, R.; Müllen, K.; Passerone, D.; Fasel, R. Surface-Assisted Cyclodehydrogenation Provides a Synthetic Route towards Easily Processable and Chemically Tailored Nanographenes. *Nat. Chem.* **2011**, *3* (1), 61–67.

(92) Bartels, L.; Meyer, G.; Rieder, K.-H. Controlled Vertical Manipulation of Single CO Molecules with the Scanning Tunneling Microscope: A Route to Chemical Contrast. *Appl. Phys. Lett.* **1997**, *71* (2), 213.

(93) Mohn, F.; Schuler, B.; Gross, L.; Meyer, G. Different Tips for High-Resolution Atomic Force Microscopy and Scanning Tunneling Microscopy of Single Molecules. *Appl. Phys. Lett.* **2013**, *102* (7).

(94) Gross, L.; Mohn, F.; Moll, N.; Liljeroth, P.; Meyer, G. The Chemical Structure of a Molecule Resolved by Atomic Force Microscopy. *Science* **2009**, *325* (5944), 1110–1114.

(95) Gross, L.; Mohn, F.; Moll, N.; Schuler, B.; Criado, A.; Guitián, E.; Peña, D.; Gourdon, A.; Meyer, G. Bond-Order Discrimination by Atomic Force Microscopy. *Science* **2012**, *337* (6100), 1326–1329.

(96) Gross, L.; Mohn, F.; Moll, N.; Meyer, G.; Ebel, R.; Abdel-Mageed, W. M.; Jaspars, M. Organic Structure Determination Using Atomic-Resolution Scanning Probe Microscopy. *Nat. Chem.* **2010**, *2* (10), 821–825.

(97) Ashino, M.; Obergfell, D.; Haluška, M.; Yang, S.; Khlobystov, A. N.; Roth, S.; Wiesendanger, R. Atomically Resolved Mechanical Response of Individual Metallofullerene Molecules Confined inside Carbon Nanotubes. *Nat. Nanotechnol.* **2008**, *3* (6), 337–341.

(98) Ashino, M.; Schwarz, A.; Behnke, T.; Wiesendanger, R. Atomic-Resolution Dynamic Force Microscopy and Spectroscopy of a Single-Walled Carbon Nanotube: Characterization of Interatomic van Der Waals Forces. *Phys. Rev. Lett.* **2004**, *93* (13), 136101.

(99) Gross, L.; Mohn, F.; Moll, N.; Liljeroth, P.; Meyer, G. The Chemical Structure of a Molecule Resolved by Atomic Force Microscopy. *Science (80-.).* **2009**, *325* (5944).

(100) Otero, G.; Biddau, G.; Sánchez-Sánchez, C.; Caillard, R.; López, M. F.; Rogero, C.; Palomares, F. J.; Cabello, N.; Basanta, M. A.; Ortega, J.; Méndez, J.; Echavarren, A. M.; Pérez, R.; Gómez-Lor, B.; Martín-Gago, J. A. Fullerenes from Aromatic Precursors by Surface-Catalysed Cyclodehydrogenation. *Nature* **2008**, *454* (7206), 865–868.

(101) Deshpande, A.; Sham, C.-H.; Alaboson, J. M. P.; Mullin, J. M.; Schatz, G. C.; Hersam, M. C. Self-Assembly and Photopolymerization of Sub-2 Nm One-Dimensional Organic Nanostructures on Graphene. *J. Am. Chem. Soc.* **2012**, *134* (40), 16759–16764.

(102) Bebensee, F.; Bombis, C.; Vadapoo, S.-R.; Cramer, J. R.; Besenbacher, F.; Gothelf, K. V.; Linderoth, T. R. On-Surface Azide–Alkyne Cycloaddition on Cu(111): Does It "Click" in Ultrahigh Vacuum? *J. Am. Chem. Soc.* **2013**, *135* (6), 2136–2139.

(103) Zhong, D.; Franke, J.-H.; Podiyanachari, S. K.; Blömker, T.; Zhang, H.; Kehr, G.; Erker, G.; Fuchs, H.; Chi, L. Linear Alkane Polymerization on a Gold Surface. *Science (80-.).* **2011**, *334* (6053).

(104) Wang, W.; Shi, X.; Wang, S.; Van Hove, M. A.; Lin, N. Single-Molecule Resolution of an Organometallic Intermediate in a Surface-Supported Ullmann Coupling Reaction. *J. Am. Chem. Soc.* **2011**, *133* (34), 13264–13267.

(105) Ertl, G. Elementary Steps in Heterogeneous Catalysis. *Angew. Chemie Int. Ed. English* **1990**, *29* (11), 1219–1227.

(106) Somorjai, G. The Surface Science of Heterogeneous Catalysis. *Surf. Sci.* **1994**, *299–300*, 849–866.

(107) Wiesendanger, R. *Scanning Probe Microscopy and Spectroscopy: Methods and Applications*; Cambridge University Press: Cambridge, 1998.

(108) Hanssen, K. Ø.; Schuler, B.; Williams, A. J.; Demissie, T. B.; Hansen, E.; Andersen, J. H.; Svenson, J.; Blinov, K.; Repisky, M.; Mohn, F.; Meyer, G.; Svendsen, J.-S.; Ruud, K.; Elyashberg, M.; Gross, L.; Jaspars, M.; Isaksson, J. A Combined Atomic Force Microscopy and Computational Approach for the Structural Elucidation of Breitfussin A and B: Highly Modified Halogenated Dipeptides from *Thuiaria Breitfussi*. *Angew. Chemie Int. Ed.* **2012**, *51* (49), 12238–12241.

(109) Pavliček, N.; Fleury, B.; Neu, M.; Niedenführ, J.; Herranz-Lancho, C.; Ruben, M.; Repp, J. Atomic Force Microscopy Reveals Bistable Configurations of Dibenzo[a,h]thianthrene and Their Interconversion Pathway. *Phys. Rev. Lett.* **2012**, *108* (8), 86101.

(110) Jones, R. R.; Bergman, R. G. P-Benzyne. Generation as an Intermediate in a Thermal Isomerization Reaction and Trapping Evidence for the 1,4-Benzenediyl Structure. *J. Am. Chem. Soc.* **1972**, *94* (2), 660–661.

(111) Lockhart, T. P.; Mallon, C. B.; Bergman, R. G. 2,3-Di-Propyl-1,4-Dehydrobenzene. *J. Am. Chem. Soc.* **1980**, *102* (18), 5976–5978.

(112) Lewis, K. D.; Matzger, A. J. Bergman Cyclization of Sterically Hindered Substrates and Observation of Phenyl-Shifted Products. *J. Am. Chem. Soc.* **2005**, *127* (28), 9968–9969.

(113) Giessibl, F. J. Advances in Atomic Force Microscopy. *Rev. Mod. Phys.* **2003**, *75* (3), 949–983.

(114) Giessibl, F. J. Atomic Resolution on Si(111)-(7×7) by Noncontact Atomic Force Microscopy with a Force Sensor Based on a Quartz Tuning Fork. *Appl. Phys. Lett.* **2000**, *76* (11), 1470.

(115) Perdew, J. P.; Zunger, A. Self-Interaction Correction to Density-Functional Approximations for Many-Electron Systems. *Phys. Rev. B* **1981**, *23* (10), 5048–5079.

(116) Mortensen, J. J.; Hansen, L. B.; Jacobsen, K. W. Real-Space Grid Implementation of the Projector Augmented Wave Method. *Phys. Rev. B* **2005**, *71* (3), 35109.

(117) Enkovaara, J.; Rostgaard, C.; Mortensen, J. J.; Chen, J.; Dułak, M.; Ferrighi, L.; Gavnholt, J.; Glinsvad, C.; Haikola, V.; Hansen, H. A.; Kristoffersen, H. H.; Kuisma, M.; Larsen, A. H.; Lehtovaara, L.; Ljungberg, M.; Lopez-Acevedo, O.; Moses, P. G.; Ojanen, J.; Olsen, T.; Petzold, V.; Romero, N. A.; Stausholm-Møller, J.; Strange, M.; Tritsaris, G. A.; Vanin, M.; Walter, M.; Hammer, B.; Häkkinen, H.; Madsen, G. K. H.; Nieminen, R. M.; Nørskov, J. K.; Puska, M.; Rantala, T. T.; Schiøtz, J.; Thygesen, K. S.; Jacobsen, K. W. Electronic Structure Calculations with GPAW: A Real-Space Implementation of the Projector Augmented-Wave Method. *J. Phys. Condens. Matter* **2010**, *22* (25), 253202.

(118) Moll, N.; Gross, L.; Mohn, F.; Curioni, A.; Meyer, G. The Mechanisms Underlying the Enhanced Resolution of Atomic Force Microscopy with Functionalized Tips. *New J. Phys.* **2010**, *12* (12), 125020.

(119) Zhao, A.; Li, Q.; Chen, L.; Xiang, H.; Wang, W.; Pan, S.; Wang, B.; Xiao, X.; Yang, J.; Hou, J. G.; Zhu, Q. Controlling the Kondo Effect of an Adsorbed Magnetic Ion through Its Chemical Bonding. *Science* **2005**, *309* (5740), 1542–1544.

(120) Kohn, W. Nobel Lecture: Electronic Structure of Matter—wave Functions and Density Functionals. *Rev. Mod. Phys.* **1999**, *71* (5), 1253–1266.

(121) Hofmann, M.; Schaefer, H. F. Pathways for the Reaction of the Butadiene Radical Cation,

$[C_4H_6]^{\bullet+}$, with Ethylene. *J. Phys. Chem. A* **1999**, *103* (44), 8895–8905.

(122) Bader, R. F. W. *Atoms in Molecules: A Quantum Theory*, Vol. 3.; Oxford University: Oxford, UK, 1990.

(123) Cabellos, J. L.; Mowbray, D. J.; Goiri, E.; El-Sayed, A.; Floreano, L.; de Oteyza, D. G.; Rogero, C.; Ortega, J. E.; Rubio, A. Understanding Charge Transfer in Donor–Acceptor/Metal Systems: A Combined Theoretical and Experimental Study. *J. Phys. Chem. C* **2012**, *116* (34), 17991–18001.

(124) Lee, C.-Y.; Wu, M.-J. Synthesis of Benzofulvenes by Palladium-Catalyzed Cyclization of 1,2-Dialkynylbenzenes. *European J. Org. Chem.* **2007**, *2007* (21), 3463–3467.

(125) Alabugin, I. V.; Manoharan, M. Radical-Anionic Cyclizations of Enediynes: Remarkable Effects of Benzannelation and Remote Substituents on Cyclo *Re* Aromatization Reactions. *J. Am. Chem. Soc.* **2003**, *125* (15), 4495–4509.

(126) Alabugin, I. V.; Kovalenko, S. V. C1−C5 Photochemical Cyclization of Enediynes. *J. Am. Chem. Soc.* **2002**, *124* (31), 9052–9053.

(127) Wennerstroem, O. Qualitative Evaluation of the Band Gap in Polymers with Extended .pi. Systems. *Macromolecules* **1985**, *18* (10), 1977–1980.

(128) van der Lit, J.; Boneschanscher, M. P.; Vanmaekelbergh, D.; Ijäs, M.; Uppstu, A.; Ervasti, M.; Harju, A.; Liljeroth, P.; Swart, I. Suppression of Electron–vibron Coupling in Graphene Nanoribbons Contacted via a Single Atom. *Nat. Commun.* **2013**, *4*.

(129) Hybertsen, M. S.; Louie, S. G. First-Principles Theory of Quasiparticles: Calculation of Band Gaps in Semiconductors and Insulators. *Phys. Rev. Lett.* **1985**, *55* (13), 1418–1421.

(130) Deslippe, J.; Samsonidze, G.; Strubbe, D. A.; Jain, M.; Cohen, M. L.; Louie, S. G. BerkeleyGW: A Massively Parallel Computer Package for the Calculation of the Quasiparticle and Optical Properties of Materials and Nanostructures. *Comput. Phys. Commun.* **2012**, *183* (6), 1269–1289.

(131) Henze, S. K. M.; Bauer, O.; Lee, T.-L.; Sokolowski, M.; Tautz, F. S. Vertical Bonding Distances of PTCDA on Au(111) and Ag(111): Relation to the Bonding Type. *Surf. Sci.* **2007**, *601* (6), 1566–1573.

(132) Neaton, J. B.; Hybertsen, M. S.; Louie, S. G. Renormalization of Molecular Electronic Levels at Metal-Molecule Interfaces. *Phys. Rev. Lett.* **2006**, *97* (21), 216405.

(133) Zhang, J.; Chen, P.; Yuan, B.; Ji, W.; Cheng, Z.; Qiu, X. Real-Space Identification of Intermolecular Bonding with Atomic Force Microscopy. *Science* **2013**, *342* (6158), 611–614.

(134) Sweetman, a M.; Jarvis, S. P.; Sang, H.; Lekkas, I.; Rahe, P.; Wang, Y.; Wang, J.; Champness, N. R.; Kantorovich, L.; Moriarty, P. J. Mapping the Force Field of a Hydrogen-Bonded Assembly. *Nat. Commun.* **2014**, *5* (May 2014), 3931.

(135) Hämäläinen, S. K.; Van Der Heijden, N.; Van Der Lit, J.; Den Hartog, S.; Liljeroth, P.; Swart, I. Intermolecular Contrast in Atomic Force Microscopy Images without Intermolecular Bonds. *Phys. Rev. Lett.* **2014**, *113* (18).

(136) Kawai, S.; Sadeghi, A.; Xu, F.; Peng, L.; Orita, A.; Otera, J.; Goedecker, S.; Meyer, E. Extended Halogen Bonding between Fully Fluorinated Aromatic Molecules. *ACS Nano* **2015**, *9* (3), 2574–2583.

(137) Zhang, Y.-Q.; Kepčija, N.; Kleinschrodt, M.; Diller, K.; Fischer, S.; Papageorgiou, A. C.; Allegretti, F.; Björk, J.; Klyatskaya, S.; Klappenberger, F.; Ruben, M.; Barth, J. V. Homo-Coupling of Terminal Alkynes on a Noble Metal Surface. *Nat. Commun.* **2012**, *3*, 1286.

(138) Zhang, X.; Liao, L.; Wang, S.; Hu, F.; Wang, C.; Zeng, Q. Polymerization or Cyclic Dimerization: Solvent Dependent Homo-Coupling of Terminal Alkynes at HOPG Surface. *Sci. Rep.* **2014**, *4*, 3899.

(139) Eichhorn, J.; Heckl, W. M.; Lackinger, M. On-Surface Polymerization of 1,4-Diethynylbenzene on Cu(111). *Chem. Commun.* **2013**, *49* (28), 2900.

(140) Riss, A.; Wickenburg, S.; Gorman, P.; Tan, L. Z.; Tsai, H. Z.; De Oteyza, D. G.; Chen, Y. C.; Bradley, A. J.; Ugeda, M. M.; Etkin, G.; Louie, S. G.; Fischer, F. R.; Crommie, M. F. Local Electronic and Chemical Structure of Oligo-Acetylene Derivatives Formed through Radical Cyclizations at a Surface. *Nano Lett.* **2014**, *14* (5), 2251–2255.

(141) Weymouth, A. J.; Hofmann, T.; Giessibl, F. J. Quantifying Molecular Stiffness and Interaction with Lateral Force Microscopy. *Science (80-.).* **2014**, *352* (6336), 600–603.

(142) Boneschanscher, M. P.; Hämäläinen, S. K.; Liljeroth, P.; Swart, I. Sample Corrugation Affects the Apparent Bond Lengths in Atomic Force Microscopy. *ACS Nano* **2014**, *8* (Xx), 3006–3014.

(143) Hapala, P.; Temirov, R.; Tautz, F. S.; Jelínek, P. Origin of High-Resolution IETS-STM Images of Organic Molecules with Functionalized Tips. *Phys. Rev. Lett.* **2014**, *113* (22).

(144) Guo, C.-S.; Van Hove, M. A.; Ren, X.; Zhao, Y. High-Resolution Model for Noncontact Atomic Force Microscopy with a Flexible Molecule on the Tip Apex. *J. Phys. Chem. C* **2015**, *119* (3), 1483–1488.

(145) Moll, N.; Schuler, B.; Kawai, S.; Xu, F.; Peng, L.; Orita, A.; Otera, J.; Curioni, A.; Neu, M.; Repp, J.; Meyer, G.; Gross, L. Image Distortions of a Partially Fluorinated Hydrocarbon Molecule in Atomic Force Microscopy with Carbon Monoxide Terminated Tips. *Nano Lett.* **2014**, *14* (11), 6127–6131.

(146) Fabig, S.; Haberhauer, G.; Gleiter, R. Dimerization of Two Alkyne Units: Model Studies, Intermediate Trapping Experiments, and Kinetic Studies. *J. Am. Chem. Soc.* **2015**, *137* (5), 1833–1843.

(147) Atkins, P.; de Paula, J. *Atkins' Physical Chemistry*, 7th ed.; OUP Oxford, 2002.

(148) Reuter, K.; Scheffler, M. First-Principles Kinetic Monte Carlo Simulations for Heterogeneous Catalysis: Application to the CO Oxidation at RuO2(110). *Phys. Rev. B Condens. Matter Mater. Phys.* **2006**, *73* (4), 045433/1-045433/17.

(149) Stoltze, P.; Nørskov, J. K. Theoretical Modelling of Catalytic Reactions. In *Handbook of Heterogeneous Catalysis*; Wiley-VCH Verlag GmbH & Co. KGaA, 2008.

(150) Neurock, M. The Microkinetics of Heterogeneous Catalysis. By J. A. Dumesic, D. F. Rudd, L. M. Aparicio, J. E. Rekoske, and A. A. Treviño, ACS Professional Reference Book, American Chemical Society, Washington, DC, 1993, 315 Pp. *AIChE Journal*. Dept. of Chemical Engineering, University of Delaware, Newark, DE 19716 1994, pp 1085–1087.

(151) Meyer, J.; Reuter, K. Modeling Heat Dissipation at the Nanoscale: An Embedding Approach for Chemical Reaction Dynamics on Metal Surfaces. *Angew. Chemie - Int. Ed.* **2014**, *53* (18), 4721–4724.

(152) Ditze, S.; Stark, M.; Buchner, F.; Aichert, A.; Jux, N.; Luckas, N.; Görling, A.; Hieringer, W.; Hornegger, J.; Steinrück, H. P.; Marbach, H. On the Energetics of Conformational Switching of Molecules at and close to Room Temperature. *J. Am. Chem. Soc.* **2014**, *136* (4), 1609–1616.

(153) Marbach, H.; Steinrück, H.-P. Studying the Dynamic Behaviour of Porphyrins as Prototype Functional Molecules by Scanning Tunnelling Microscopy close to Room Temperature. *Chem. Commun.* **2014**, *50* (65), 9034–9048.

(154) Eyring, H. The Activated Complex in Chemical Reactions. *J. Chem. Phys.* **1935**, *3* (2), 107–115.

(155) Laidler, K. J.; King, M. C. The Development of Transition-State Theory. *J. Phys. Chem.* **1983**, *87* (15), 2657–2664.

(156) McQuarrie, D. A. *Statistical Mechanics*; University Science Books, 2000.

(157) Garcia-Araez, N.; Climent, V.; Feliu, J. Separation of Temperature Effects on Double-Layer and Charge-Transfer Processes for Platinum|Solution Interphases. Entropy of Formation of the Double Layer and Absolute Molar Entropy of Adsorbed Hydrogen and OH on Pt(111). *J. Phys. Chem. C* **2009**, *113* (46), 19913–19925.

(158) Ayala, P. Y.; Schlegel, H. B. Identification and Treatment of Internal Rotation in Normal Mode Vibrational Analysis. *J. Chem. Phys.* **1998**, *108* (6), 2314.

(159) van der Lit, J.; Boneschanscher, M. P.; Vanmaekelbergh, D.; Ijäs, M.; Uppstu, A.; Ervasti, M.; Harju, A.; Liljeroth, P.; Swart, I. Suppression of Electron–vibron Coupling in Graphene Nanoribbons Contacted via a Single Atom. *Nat. Commun.* **2013**, *4* (May), 2023.

(160) Charles L. Perrin, *; Betsy L. Rodgers, and; O'Connor*, J. M. Nucleophilic Addition to a P-Benzyne Derived from an Enediyne: A New Mechanism for Halide Incorporation into Biomolecules. **2007**.

References

(161) Perrin, C. L.; Reyes-Rodríguez, G. J. Selectivity and Isotope Effects in Hydronation of a Naked Aryl Anion. *J. Am. Chem. Soc.* **2014**, *136* (43), 15263–15269.

(162) Jiang, W.; Shang, B.; Li, L.; Zhang, S.; Zhen, Y. Construction of a Genetically Engineered Chimeric Apoprotein Consisting of Sequences Derived from Lidamycin and Neocarzinostatin. *Anticancer. Drugs* **2016**, *27* (1), 24–28.

(163) Shao, R.-G. Pharmacology and Therapeutic Applications of Enediyne Antitumor Antibiotics. *Curr. Mol. Pharmacol.* **2008**, *1* (1), 50–60.

(164) Wenk, H. H.; Winkler, M.; Sander, W. One Century of Aryne Chemistry. *Angew. Chemie Int. Ed.* **2003**, *42* (5), 502–528.

(165) Perrin, C. L.; Reyes-Rodríguez, G. J. Reactivity of Nucleophiles toward a *P* -Benzyne Derived from an Enediyne. *J. Phys. Org. Chem.* **2013**, *26* (2), 206–210.

(166) Pietruszka, J.; Witt, A. Synthesis of the Bestmann-Ohira Reagent. *Synthesis (Stuttg).* **2006**, *2006* (24), 4266–4268.

(167) Saito, R.; Furukawa, M.; Dresselhaus, G.; Dresselhaus, M. S. Raman Spectra of Graphene Ribbons. *J. Phys. Condens. Matter* **2010**, *22* (33), 334203.

(168) Pimenta, M. A.; Dresselhaus, G.; Dresselhaus, M. S.; Cançado, L. G. Studying Disorder in Graphite-Based Systems by Raman Spectroscopy. *Phys. Chem. Chem. Phys.* **2007**, *9* (11), 1276–1290.

(169) Saito, R.; Grüneis, A.; Samsonidze, G. G.; Brar, V. W.; Dresselhaus, G.; Dresselhaus, M. S.; Jorio, A.; Cançado, L. G.; Fantini, C.; Pimenta, M. A.; Filho, A. G. S. Double Resonance Raman Spectroscopy of Single-Wall Carbon Nanotubes. *New J. Phys.* **2003**, *5* (1), 157–157.

(170) Cançado, L. G.; Pimenta, M. A.; Neves, B. R. A.; Medeiros-Ribeiro, G.; Enoki, T.; Kobayashi, Y.; Takai, K.; Fukui, K.; Dresselhaus, M. S.; Saito, R.; Jorio, A. Anisotropy of the Raman Spectra of Nanographite Ribbons. *Phys. Rev. Lett.* **2004**, *93* (4), 47403.

(171) Schwab, M. G.; Narita, A.; Hernandez, Y.; Balandina, T.; Mali, K. S.; De Feyter, S.; Feng, X.; Müllen, K. Structurally Defined Graphene Nanoribbons with High Lateral Extension. *J. Am. Chem. Soc.* **2012**, *134* (44), 18169–18172.

(172) Horcas, I.; Fernández, R.; Gómez-Rodríguez, J. M.; Colchero, J.; Gómez-Herrero, J.; Baro, A. M. WSXM: A Software for Scanning Probe Microscopy and a Tool for Nanotechnology. *Rev. Sci. Instrum.* **2007**, *78* (1), 13705.

(173) Deslippe, J.; Samsonidze, G.; Jain, M.; Cohen, M. L.; Louie, S. G. Coulomb-Hole Summations and Energies for G W Calculations with Limited Number of Empty Orbitals: A Modified Static Remainder Approach. *Phys. Rev. B* **2013**, *87* (16), 165124.

(174) Tamblyn, I.; Darancet, P.; Quek, S. Y.; Bonev, S. A.; Neaton, J. B. Electronic Energy Level Alignment at Metal-Molecule Interfaces with a G W Approach. *Phys. Rev. B* **2011**, *84* (20), 201402.

References

(175) CRC Handbook of Chemistry and Physics. **2006**.